

UNIVERSITY OF CALIFORNIA

Santa Barbara

Integrated Optical Isolators and Circulators for Heterogeneous Silicon Photonics

A dissertation submitted in partial satisfaction of the
requirements for the degree Doctor of Philosophy
in Electrical and Computer Engineering

by

Duanni Huang

Committee in charge:

Professor John E. Bowers, Chair

Professor Larry A. Coldren

Professor Nadir Dagli

Professor Jon A. Schuller

March 2019

The dissertation of Duanni Huang is approved.

Larry A. Coldren

Nadir Dagli

Jon A. Schuller

John E. Bowers, Committee Chair

March 2019

**Integrated Optical Isolators and Circulators for
Heterogeneous Silicon Photonics**

Copyright © 2019

by

Duanni Huang

ACKNOWLEDGMENTS

The work would not be possible without the assistance and good will of many others. Research at this level is simply not possible without the teamwork of many individuals.

First of all, I'd like to give my sincere thanks to Professor John E. Bowers, whose guidance played an instrumental role in this work. He provided the right balance of attention to detail without losing track of the overall picture. The environment in his group is one that really promotes a balance of academic curiosity with realistic expectations. Over my five and a half years in his group at UCSB, John was also kind enough to provide me with all the resources I needed to succeed. I feel like I will only truly appreciate how lucky I was to be in his group after I graduate.

I also thank Professor Larry Coldren for teaching me everything I know about lasers, as well as Professor Jon Schuller and Professor Nadir Dagli for teaching me quantum mechanics and electromagnetism respectively. After I finished my coursework, I started to appreciate the bits and pieces of classwork that reared their heads in my research. Sometimes I wish I paid more attention in class, which could have saved me some time down the road, but hey, you only truly learn something when you learn it for the second (or third) time. Thank you for serving on my committee.

Of course, the students around me in graduate school create the atmosphere that is so conducive towards research and learning. I would like to give my gratitude to Dr. Paolo Pintus, whom contributed directly to almost every work in this dissertation. I was lucky enough to work with Paolo from the very beginning, which allowed me to hit the ground running. I would also like to thank Dr. Minh Tran, with whom I have worked

extensively over the last few years. His optimism certainly balances out my pessimism at times, and we make a great team. I was also lucky enough to have older students and postdocs such as Mike, Daryl, Sudha, Chong, and Tin that I could go to with questions. Their constant availability and willingness to help despite their own busy schedules is something I truly appreciate. I'd also like to thank all the other Bowers students and visitors both past (Jock, Jared, Nick, Andreas, Xinru, Daisuke, Shangjian, Daehwan, Jinxi, Eric, Emmett, Aditya, Alan, Yichen) and present (Alex, Aditya, Songtao, Yating, Chen, Weiqiang, Lin, Justin, Akhilesh, Andy, Chao, Robert, Jenny, Warren, Kaiyin, Noelle, Joel).

The fabrication facilities and expertise at UCSB are truly unique, and I would like to thank the Nanofab and all its staff. Special thanks go to Jon Peters, MJ, and Alfredo. You are truly Ph.D. accelerators, and probably shaved a year off my timeline. Speaking of staff members, Tina and Ceanna worked behind the scenes to take care of all the time consuming paperwork. Thank you!

Not everything in graduate school is work-related, and the Bowers basketball group certainly attests to that. I will definitely miss our (bi)weekly games. I hope this continues after I graduate, and I can pop in for a quick game whenever I'm around UCSB. For all its pros, Santa Barbara is lacking when it comes to Chinese food, and I appreciate everyone who went with me on food-seeking trips to Los Angeles. I will also miss our Taco Tuesdays and Chick-fil-a Everyday. I also thank my housemates at the Berkeley house, especially Lin, who is still there. It has been my home for the past four years.

None of this work would be possible without the help of collaborators outside UCSB. I would especially like to thank Professor Yuya Shoji and Professor Tetsuya Mizumoto for providing me with material to fabricate the devices with, as well as Professor

Caroline Ross and Professor Bethanie Stadler for our joint work. Engineering research is only possible with sufficient funding, and for that I would like to thank Dr. Paul Morton and Morton Photonics, as well as the NSF GFRP.

Finally, I would like to thank my family. My parents have supported me from the very beginning, providing a constant stream of support. The roots of my academic curiosity and abilities start well before UCSB, and my parents have made sure that I set out on the right path. I also wish the best of luck to my brother Dennis, whom is just beginning his graduate adventure as well. The path is long and sometimes a struggle, but is definitely worth it in the end, as cliché as that may sound.

CURRICULUM VITAE OF DUANNI HUANG
March 2019

EDUCATION

B.S. in Electrical Engineering and Computer Science, Massachusetts Institute of Technology, June 2013.

M.S. in Electrical and Computer Engineering, University of California, Santa Barbara, June 2015.

Ph.D. in Electrical and Computer Engineering, University of California, Santa Barbara, March 2019.

AWARDS AND HONORS

OFC Corning Outstanding Student Paper Competition – Honorable Mention (2019)

CLEO Maiman Student Paper Competition – Honorable Mention (2016)

NSF Graduate Student Research Fellowship (2015)

UCSB Holbrook Foundation Fellow (2014)

MIT EECS Conference Undergraduate Speaker Award (2013)

Intel International Science and Engineering Fair - 1st place (2009)

Siemens National Competition in Science and Technology - 3rd place (2008)

JOURNAL PUBLICATIONS

1. **Huang, D.**, Tran, M.A., Guo, J., Peters, J., Komljenovic, T., Malik, A., Morton, P.A., and Bowers, J.E. "High-power sub-kHz linewidth lasers fully integrated on silicon." *Optica*, *submitted* (2019).
2. Zhang, Y., Du, Q., Wang, C., Fakhrol, T., Liu, S., Deng, L., **Huang, D.**, Pintus, P., Bowers, J.E., Ross, C.A., and Hu, J., and Bi, L. "Monolithic integration of broadband optical isolators for polarization-diverse silicon photonics." *Optica*, *accepted* (2019).
3. Pintus, P., **Huang, D.**, Morton, P.A., Shoji, Y., Mizumoto, T., and Bowers, J.E. "Broadband TE Optical Isolators and Circulators in Silicon Photonics through Ce:YIG Bonding." *J. Light. Technol.* (2019) [*Invited Paper*].
4. **Huang, D.**, Pintus, P., and Bowers, J.E. "Towards heterogeneous integration of optical isolators and circulators with lasers on silicon." *Opt. Mater. Express* 8(9), 2471-2483 (2018) [*Invited Paper*].
5. Komljenovic, T., **Huang, D.**, Pintus, P., Tran, M.A., Davenport, M.L, and Bowers, J.E. "Photonic integrated circuits using heterogeneous integration on silicon." *Proc. IEEE* 106(12) 2246-2257 (2018) [*Invited Paper*].

6. Tran, M. A., **Huang, D.**, Komljenovic, T., Peters, J., Malik, A., & Bowers, J. E. "Ultra-Low-Loss Silicon Waveguides for Heterogeneously Integrated Silicon/III-V Photonics." *Appl. Sci.*, 8(7), 1139 (2018) [**Feature Paper**].
7. **Huang, D.**, Pintus, P., Morton, P., Shoji, Y., Mizumoto, T., and Bowers, J. E. "Integrated broadband Ce:YIG/Si Mach-Zehnder optical isolators with over 100nm tuning range." *Opt. Lett.* 42(23), 4901-4904 (2018).
8. Wan, Y., Norman, J., Li, Q., Kennedy, MJ, Liang, D., Zhang, C., **Huang, D.**, Zhang, Z., Liu, A., Torres, A., Jung, D., Gossard, A., Hu, El, Lau, K., and Bowers, J. E. "1.3 um submilliamp threshold quantum dot micro-lasers on Si." *Optica* 4(8) 940-944 (2017).
9. Pintus, P., **Huang, D.**, Zhang, C., Shoji, Y., Mizumoto, T., and Bowers, J. E. "Microring-based optical isolator and circulator with integrated electromagnet for silicon photonics." *J. Light. Technol.* 35(8), 1429-1437 (2017) [**Invited Paper**].
10. **Huang, D.**, Pintus, P., Zhang, C., Morton, P., Shoji, Y., Mizumoto, T., and Bowers, J. E. "Dynamically reconfigurable integrated optical circulators." *Optica*, 4(1), 23-30 (2017).
11. **Huang, D.**, Pintus, P., Zhang, C., Shoji, Y., Mizumoto, T., and Bowers, J. E. "Electrically driven and thermally tunable integrated optical isolators for silicon photonics." *IEEE J. Sel. Top. Quantum Electron.* 22(6), 271-278 (2016).
12. **Huang, D.**, Srinivasan, S., and Bowers, J. E. "Compact Tb doped fiber optic current sensor with high sensitivity." *Opt. Express* 23(23), 29993-29999 (2015) [**Highlighted by SPIE Newsroom**].
13. **Huang, D.**, Santhanam, P., and Ram, R. J. "Low-power Communication with a Photonic Heat Pump." *Opt. Express*, 22(107), A1650-A1658 (2014) [**Highlighted by OSA Spotlight on Optics and Nature Photonics**].
14. Cobaleda, C.S., Xiao, X., Burckel, D. B., Polsky, R., **Huang, D.**, Diez, E., and Pan, W. "Superconducting properties in tantalum decorated three-dimensional graphene and carbon structures." *Appl. Phys. Lett.*, 105(5), 053505 (2014).
15. Santhanam, P., **Huang, D.**, Ram, R. J., Remennyi, M. A., & Matveev, B. A. "Room temperature thermo-electric pumping in mid-infrared light-emitting diodes." *Appl. Phys. Lett.*, 103(18), 183513 (2013).

CONFERENCE PUBLICATIONS

1. **Huang, D.**, Tran, M.A., Guo, J., Peters, J., Komljenovic, T., Malik, A., Morton, P.A., and Bowers, J.E. "Sub-kHz linewidth Extended-DBR lasers heterogeneously integrated on silicon." *Optical Fiber Communication Conference* (2019).
2. Bowers, J.E., **Huang, D.**, Jung, D., Norman, J., Tran, M.A., Wan, Y., Xie, W., and Zhang, Z. "Realities and challenges of III-V/Si integration technologies." *Optical Fiber Communication Conference* (2019) [**Invited Talk**].

3. **Huang, D.**, Pintus, P., Peters, J., Morton, P., Shoji, Y., Mizumoto, T., and Bowers, J. E. "Widely tunable Ce:YIG on Si microring isolators for TE mode operation." *Group IV Photonics* (2018).
4. Pintus, P., **Huang, D.**, Morton, P.A., Shoji, Y., Mizumoto, T., and Bowers, J.E. "Integrated optical isolator and circulator in silicon photonics." *European Conference on Optical Communication* (2018) [**Invited Talk**].
5. Tran, M., **Huang, D.**, Komljenovic, T., Liu, S., Liang, L., Kennedy, M, and Bowers, J. E. "Multi-ring Mirror-based Narrow Linewidth Widely-Tunable Lasers in Heterogeneous Silicon Photonics." *European Conference on Optical Communication* (2018) [**Invited Talk**].
6. Tran, M., **Huang, D.**, Komljenovic, T., Peters, J., and Bowers, J. E. "A 2.5kHz linewidth widely tunable laser with booster SOA integrated on silicon." *IEEE International Semiconductor Laser Conference* (2018).
7. **Huang, D.**, Pintus, P., Shoji, Y., Mizumoto, T., and Bowers, J. E. "Heterogeneously integration optical isolators and circulators on silicon." *Progress in Electromagnetism Research* (2018) [**Invited Talk**].
8. Tran, M., Komljenovic, T., **Huang, D.**, Liang, L., Kennedy, MJ, and Bowers, J. E. "A Widely-Tunable High-SMSR Narrow-Linewidth Laser Heterogeneously Integrated on Silicon." *CLEO: Science and Innovations* (2018).
9. Wu, X., Zhou, W., **Huang, D.**, Zhang, Z., Wang, Y., Bowers, J. E., and Tsang, H. K. "Low crosstalk bent multimode waveguide for on-chip mode-division-multiplexing interconnects" *CLEO: Science and Innovations* (2018).
10. Pintus, P., **Huang, D.**, Shoji, Y., Mizumoto, T., and Bowers, J. E. "Integrated widely tunable broadband optical isolator in silicon photonics." *European Conference on Optical Communication* (2017).
11. Pintus, P., **Huang, D.**, Shoji, Y., Mizumoto, T., and Bowers, J.E. "Heterogeneously integrated optical isolators and circulators." *Integrated Photonics Research* (2017) [**Invited Talk**].
12. Wan, Y., Norman, J., Li, Q., Kennedy, M., Liang, D., Zhang, C., **Huang, D.**, Zhang, Z., Liu, A.Y., Torres, A., Jung, D., Gossard, A., Hu, E.L., Lau, K.M., and Bowers, J.E. "1.3um submilliamp threshold quantum dot micro-lasers on Si" *CLEO: Science and Innovations* (2017).
13. Davenport, M., Chang, L., **Huang, D.**, Volet, N., and Bowers, J.E. "Heterogeneous photonic integration by direct wafer bonding" *ECS Transactions* (2016).
14. **Huang, D.**, Pintus, P., Zhang, C., Shoji, Y., Mizumoto, T., and Bowers, J. E. "Multiple-port integrated optical circulators." *IEEE Photonics Conference* (2016).
15. **Huang, D.**, Pintus, P., Zhang, C., Shoji, Y., Mizumoto, T., and Bowers, J. E. "Reconfigurable integrated optical circulator." *CLEO: Science and Innovations* (2016) [**Invited Talk**].

16. Pintus, P., **Huang, D.**, Zhang, C., Shoji, Y., Mizumoto, T., and Bowers, J. E. “Novel nonreciprocal devices with integrated electromagnet for silicon photonics.” *European Conference on Optical Communication* (2016).
17. **Huang, D.**, Pintus, P., Zhang, C., Shoji, Y., Mizumoto, T., and Bowers, J. E. “Silicon microring isolator with large optical isolation and low loss.” *Optical Fiber Communication Conference* (2016).
18. **Huang, D.**, Pintus, P., Srinivasan, S., and Bowers, J. E. “Integrated compact optical current sensors with high sensitivity.” *SPIE Photonics West* (2016) [**Invited Talk**].
19. **Huang, D.**, Xiao, X., Polsky, R., Bruce Burckel, D., Luk, T., Brener, I. & Pan, W. “Three-dimensional graphene photonic crystal.” APS March Meeting. *Bulletin of the American Physical Society* (2014).

PATENTS

Bowers, J.E., Pintus, P. and **Huang, D.**, “Reconfigurable Integrated-Optics-Based Non-Reciprocal Devices.” *U.S. Patent Application* 16/074,905 (2019).

ABSTRACT

Integrated Optical Isolators and Circulators for Heterogeneous Silicon Photonics

by

Duanni Huang

Integrated optical isolators are nonreciprocal optical components that allow light to pass in one direction only. They are useful in conjunction with lasers, as they block undesired reflections from entering the laser cavity, where it might destabilize the device. Optical circulators are extensions of isolators, as they reroute the backwards propagating light into another direction. Thus, they can be used to separate counterpropagating signals. Both devices have many uses in photonic integrated circuits, but are challenging to implement, due to the reciprocal nature of most semiconductor and dielectric materials.

Magnetic materials such as garnets can break the symmetry and are well suited for optical isolators and circulators. However, they are difficult to integrate with silicon, III-V, and other commonly used optical materials. Heterogeneous integration through wafer bonding can overcome this obstacle and is used successfully in this work to achieve integrated optical isolators and circulators on silicon with record performance. This is done through waveguide optimization, careful process development, and a novel idea to integrate the source of magnetic fields, an electromagnet, directly onto the chip. This not

only shrinks the footprint of the devices, but also provides flexibility in design as well as wavelength tunability, which is critical if the device is to be used in a circuit.

Two flavors of the isolator and circulator are presented. One is a resonant device using a microring that can achieve up to 32dB of isolation. Slight modifications to the design can result in a microring optical circulator as well, a first to the best of our knowledge. The other device architecture is a nonresonant device using a Mach-Zehnder interferometer. While these devices have larger footprint, they can achieve optical isolation over 20dB over a wide wavelength range of 18nm. This is extremely useful in applications such as data transmission, where backwards propagating light may be spread over several nanometers.

Of course, the isolator should be paired with a laser to realize its true potential. Several design and fabrication challenges stand in the way of this, which are addressed in this work. Polarization rotators are implemented to match the operating polarization between the laser and the isolator, and fabrication is carefully tailored such that both devices can be integrated on the same chip. Preliminary results show that the laser and isolator integration can happen in the near future. Such a demonstration would open up new opportunities in photonic integrated circuits, and would be of great interest in optical communications, sensing, RF photonics, as well as new, unexplored fields.

TABLE OF CONTENTS

Chapter 1 Introduction.....	1
1.1 Integrated Optics	1
1.2 Heterogeneous silicon photonics	3
1.3 Optical Nonreciprocity	6
Summary	10
Thesis Organization	10
References	12
Chapter 2 Magneto-optic Effects	15
2.1 Faraday Rotation.....	16
2.2. Magneto-optic materials	21
2.3 Magneto-optic effect in waveguides.....	27
2.4 Nonreciprocal phase shift.....	32
2.5 – Methods for applying a magnetic field.....	39
Summary	43
References	44
Chapter 3 Microring based nonreciprocal devices.....	50
3.1 Microring resonator.....	50
3.2 Microring optical isolator	57
Design	57
Fabrication	65

Characterization	74
3.3 Microring optical circulator	82
Design	82
Characterization	86
Coupled ring circulators	93
Summary	95
References	98
Chapter 4 Mach-Zehnder interferometer (MZI) based isolators and circulators	101
4.1 Mach-Zehnder Interferometers	101
4.2 MZI based isolator	104
Design and Fabrication	104
Device Characterization	113
4.3 MZI based Circulator	119
Summary	121
References	122
Chapter 5 Optical isolation for TE polarization	124
5.1 Nonreciprocal phase shift for TE polarization	124
5.2 TE to TM polarization rotators	131
5.3 Microring optical isolator for TE mode	142
5.4 MZI optical isolator and circulator for TE mode	145
Summary	149
References	150
Chapter 6 Laser and Isolator integration	154

6.1 Background and Motivation	154
6.2 Co-design of heterogeneous silicon laser and isolator	155
6.3 Fabrication and Preliminary Results	160
Summary	171
References	171
Chapter 7 Beyond optical isolators and circulators.....	173
7.1 Optical isolators and circulators in PIC.....	173
7.2 Magnetic sensors	176
7.3 Magneto-optic switches	178
Summary	181
References	182
Chapter 8 Conclusions and Future Outlook	184
8.1 Conclusions	184
8.2 Future Outlook.....	186
References	189

LIST OF FIGURES

Figure 1.1: SEM images of potential reflections in a PIC from facets, MMIs, and tapers.	4
Figure 1.2: Example of a reflection that can destabilize a laser cavity without an isolator, as well as the use of a circulator to separate counterpropagating signals.....	6
Figure 1.3: Schematic of all the components that have been realized on the heterogeneous silicon platform.....	6
Figure 1.4: Scattering matrix of any photonic component relating the input fields to the output fields.....	7
Figure 2.1: Schematic of Cartesian coordinate system used for analysis of a Faraday rotator in which light and magnetic field are parallel.....	16
Figure 2.2: Schematic of a polarization dependent optical isolator	19
Figure 2.3: Schematic of a polarization dependent optical circulator	20
Figure 2.4: Faraday rotation measurement of Ce:YIG/SGGG	26
Figure 2.5: Schematic of integrated Faraday rotator based isolator.....	28
Figure 2.6: Schematic of using a MO waveguide in the Voigt configuration to achieve nonreciprocal loss and phase shift.....	31
Figure 2.7: Electric field profiles for a strip and rib MO waveguide.....	36
Figure 2.8: Electric field profiles for two waveguides where the MO material is used as the cladding rather than the core.....	37
Figure 2.9: Schematic of integrated electromagnet on the backside of the Ce:YIG40	

Figure 2.10: Simulations on the magnetic field strength and temperature as a function of spacer thickness and number of coils.....	41
Figure 3.1: Schematic and SEM image of an all-pass ring resonator.....	51
Figure 3.2: Schematic and SEM image of an add-drop ring resonator	54
Figure 3.3: Schematic of the microring isolator	58
Figure 3.4: Schematic of the integrated electromagnet on top of the microring isolator	59
Figure 3.5: Depiction of the resonant wavelength split caused by NRPS.....	60
Figure 3.6: Simulated results for NRPS and resulting RWS as a function of silicon and Ce:YIG thicknesses.....	61
Figure 3.7: Simulations of the sensitivity of RWS with respect to thickness variation in the layers of the MO waveguide.	62
Figure 3.8: Simulations of the bend loss for a variety of MO waveguide geometries with different widths and thicknesses.....	63
Figure 3.9: Simulations of the coupling into the MO ring for different gaps ranging from 140nm to 400nm for a ring radius of 35 microns.....	64
Figure 3.10: Fabrication flow for integrated optical isolators and circulators	66
Figure 3.11: SEM images of the silicon waveguides used in the microring isolator prior to Ce:YIG bonding.	66
Figure 3.12: Images of Ce:YIG/SGGG 2" wafer and individual dies (bonded on Si).....	68
Figure 3.13: Micrographs of various Ce:YIG/Si bond fails stemming from particulates of varying sizes	69

Figure 3.14: Progression of Ce:YIG on silicon after bonding, anneal, and substrate removal respectively.....	70
Figure 3.15: SEM images of the waveguides entering the bonded Ce:YIG regions, from which some chipping can be observed.....	70
Figure 3.16: SEM images of the bonded cross-section, as well as the transition into the bonded areas after substrate removal is complete.	73
Figure 3.17: Micrograph and SEM image of an array of completed microring isolators.	73
Figure 3.18: Experimental results of the microring isolator showing the difference between forward and backwards transmission.	75
Figure 3.19: Measurements of the thermal induced resonance shift on top of the RWS as a function of the applied current into the microring isolator.....	77
Figure 3.20: Simulations of the magnetic field and temperature in the microring isolator as a function of applied current.....	78
Figure 3.21: Comparison of experimental and predicted thermal and RWS	79
Figure 3.22: Schematic, micrograph, and principle of operation for the cascaded microring isolator.....	81
Figure 3.23: Experimental results of the cascaded microring isolator showing nonreciprocal transmission between the forward and backward directions over a larger optical bandwidth.....	81
Figure 3.24: Schematic of microring optical circulator	84
Figure 3.25: Extinction ratio between various ports for different design criteria regarding the coupling strength into the ring.	86

Figure 3.26: Picture of test setup used to characterize optical circulators	87
Figure 3.27: Simulated and experimental spectra of the transmission through the microring circulator operating near 1558nm.	87
Figure 3.28: Schematic of a six-port microring circulator.....	90
Figure 3.29: Simulated (left) and experimental (right) transmission spectra of the six-port circulator operating near 1557.5nm.	92
Figure 3.30: Schematic and simulated performance of a coupled ring circulator showing the improvement in isolation bandwidth and ratio compared with a single ring.	94
Figure 3.31: Simulated (left) and experimental (right) transmission spectra of the coupled ring circulator.	95
Figure 4.1: Schematic of a MZI using a pair of 1x2 splitters	102
Figure 4.2: Schematic of a MZI using a pair of 2x2 splitters.	103
Figure 4.3: Schematic of the MZI isolator with electromagnets.....	105
Figure 4.4: Simulated wavelength dependence on effective index and Faraday rotation. Further details on the simulations are found in [7].	108
Figure 4.5: FDTD and EME simulations of the MMI with bonded Ce:YIG on top for TE and TM polarizations. A length of 42 microns is selected for the TE polarization, giving a 50:50 split, but no appropriate lengths are available for TM modes.	110
Figure 4.6: EME simulations of a directional coupler with Ce:YIG bonded on top for TM polarization for different wavelengths and coupling gaps. The cross (left) and bar (right) transfer functions are shown.....	111
Figure 4.7: FDTD simulations for a tapered gap Y-junction with bonded Ce:YIG on top for TM polarization.	112

Figure 4.8: Experimental comparison of a Y-junction, a tapered Y-junction, and a directional coupler in terms of extinction ratio in a MZI with bonded Ce:YIG.	112
Figure 4.9: Schematic and micrograph of MZI isolator.	113
Figure 4.10: Experimental transmission spectra through the MZI isolator for different applied currents in the electromagnet.	114
Figure 4.11: Extracted optical path difference between forward and backwards propagation in the MZI based on the data in Figure 4.10.	115
Figure 4.12: Comparison of MZI isolator with various electromagnet geometries based on data in this chapter, as well as subsequent fabrication runs, detailed in Chapter 5.	116
Figure 4.13: Experimental spectra of the broadband MZI isolator. Only a single fringe is visible within the tuning range of the laser.	117
Figure 4.14: Wavelength tuning of the broadband MZI isolator by unbalancing one of the arms slightly (+/- 20mA).	118
Figure 4.15: Extracted isolation bandwidth for the broadband MZI isolator.	119
Figure 4.16: Experimental spectra of the cross and bar ports of a MZI circulator.	120
Figure 4.17: Dependence on the extinction ratio versus power coupling.	120
Figure 5.1: Schematic for waveguide designs to achieve NRPS for TE modes	125
Figure 5.2: Process flow for preparing MO isolators for TE polarization.	126
Figure 5.3: Simulation of the RWS for different silicon and Ce:YIG widths.	127
Figure 5.4: SEM images of the waveguides with the trench adjacent to the waveguide, and the cross-section after garnet deposition.	128
Figure 5.5: SEM images of the occasional misalignment in the trench.	128

Figure 5.6: Schematic and images of the test setup for generating strong out-of-plane magnetic fields.	129
Figure 5.7: Comparison of the forward and backward spectra in the ring and MZI devices, showing no signs of nonreciprocity. Multiple sweeps showed the forward and backwards spectra to overlay exactly on top of each other.	130
Figure 5.8: Schematic and simulations of the mode hybridization between TM ₀ and TE ₁ modes at various waveguide heights from 400nm to 1100nm and widths from 220nm to 270nm.	133
Figure 5.9: Polarization ratio of the TE and TM-like modes near the crossover point at 840nm.	135
Figure 5.10: Schematic and field profiles along various points in the taper from TE ₁ to TM ₀ polarization.	136
Figure 5.11: Simulation of power transfer between TM ₀ and TE ₁ modes as a function of central taper length.	137
Figure 5.12: Simulation of the TE ₀ and TE ₁ modes for various waveguide widths for a silicon waveguide height of 220nm.	138
Figure 5.13: Schematic of the TE ₀ to TE ₁ tapered coupler.	139
Figure 5.14: FDTD simulation of the TE ₀ to TE ₁ tapered coupler.	139
Figure 5.15: Final design of the polarization converter.	140
Figure 5.16: Measurements of a waveguide with and without the polarization rotator.	141
Figure 5.17: Schematic and image of the TE mode microring isolator.	142

Figure 5.18: Experimental measurements of the forward and backward transmission through the TE mode microring isolator.....	143
Figure 5.19: Thermal tuning of the TE mode microring isolator exceeding a FSR.	144
Figure 5.20: Measurements of isolation bandwidth and wavelength range.	145
Figure 5.21: Schematic of the TE mode circulator (not showing polarization rotators)	146
Figure 5.22: Schematic of the adiabatic 50:50 splitter as well as both simulated and experimental coupling values.	147
Figure 5.23: Experimental results for the transmission through a narrowband TE mode optical circulator.	148
Figure 5.24: Experimental results for the transmission through a broadband TE mode optical circulator	149
Figure 6.1: Schematic of the cross-section of a heterogeneous silicon/III-V amplifier waveguide.....	156
Figure 6.2: Effective index of various silicon thicknesses at different waveguide widths compared with the III-V epitaxial stack. Further details found in [6].....	157
Figure 6.3: Schematic of the layout of integrated lasers with isolators and circulators.	159
Figure 6.4: Complete processing flow for the laser with isolator.....	160
Figure 6.5: Process flow of the first few silicon processing steps	161
Figure 6.6: SEM images of the LOCOS transition.....	162
Figure 6.7: AFM comparison of the surface quality of the thinned and unthinned silicon areas.....	163

Figure 6.8: Process flow of the III-V bonding and subsequent processing.	164
Figure 6.9: SEM images of the P-InP taper after etching with MHA.	165
Figure 6.10: SEM images of residue after the MHA etch using a resist mask and bubbles that may form under the mesa after BHF cleaning.....	166
Figure 6.11: Completed laser mesa structures with transitions to the silicon waveguides.	167
Figure 6.12: Process flow of the backend metallization of the lasers.....	168
Figure 6.13: SEM images of the lasers after metallization to the n and p contacts is complete.....	168
Figure 6.14: Process flow of the isolator integration after laser processing is complete.	169
Figure 7.1: Schematic of a single-frequency DFB with a booster amplifier.....	175
Figure 7.2: Schematic of the Tb-fiber based interferometric current sensor.	177
Figure 7.3: Experimental results of the switching time of the MO microring switch. The device used is identical to the microring isolator described in Chapter 3.	181

Chapter 1

Introduction

1.1 Integrated Optics

The invention of the transistor revolutionized the entire electronics industry and became the fundamental building block of integrated circuits (IC). Transistors are ubiquitous today and the underlying semiconductor industry has developed into a multi-hundred-billion-dollar industry. Following in the footsteps of the IC is the development of photonic integrated circuits (PIC), which use photons instead of electrons. Integrated optics take the same concepts (light generation and manipulation) that are used in bulk optics and shrink them down to the microscale, where the devices can be integrated together on a chip. This miniaturization of optics provides many benefits in terms of size, weight, power, and cost (SWaP + C), just like the ongoing miniaturization of electronics, otherwise known as Moore's Law.

Over the past few decades, silicon photonics has emerged as a leading platform for advanced photonic integration. The driving force behind this include economic reasons (cheaper substrates and material costs), manufacturing related reasons (larger wafer

sizes, higher processing yields), and scientific reasons (low-loss waveguides, highly compact devices). Using silicon as the primary material also comes with the benefit of using the technology and expertise developed by the semiconductor industry. Tremendous progress has been made by both academic institutions as well as industry to tackle various issues ranging from the availability of high-quality silicon-on-insulator (SOI) wafers, to the development of germanium epitaxial growth. However, the largest obstacle facing silicon-based photonics today is the same obstacle from over thirty years ago: the lack of an efficient laser diode in the group IV material system.

The laser is arguably the most important element in any PIC, as it is responsible for the generation of light. In fact, this is the primary reason why the integrated optics industry has largely been focused on III-V semiconductor systems (GaAs, InP, GaN, etc), which have direct bandgaps and are suitable for lasers. Significant efforts have been made to achieve lasing in purely group IV materials, with notable demonstrations being the silicon Raman laser [1], the germanium tin (GeSn) laser [2], and the germanium laser on silicon [3]. However, continuous wave operation at room temperature or higher is required for most practical applications, which these lasers struggle to meet due to poor efficiency.

An ideal platform would have access to both material systems (Si and III-V). Epitaxial integration of III-V materials directly on silicon is highly desired, but difficult due to lattice and thermal mismatch between the materials. The difficulty lies in improving the material quality of the III-V and reducing dislocations and defects in the material, which serve as nonradiative recombination centers. This degrades the device performance and lowers the overall lifetime of the laser. Quantum dot (QD) based materials have

improved tolerance to defects, and lifetime of QD lasers on silicon have reached millions of hours (extrapolated) by reduction of dislocations through optimization of the growth parameters and strategy [4]. However, they have not been integrated with silicon waveguides due to the need for a thick buffer layer between the silicon and the quantum dots and are therefore incompatible with silicon photonic integrated circuits as of now [5]. An alternate method to bring silicon and III-V materials together is using wafer bonding. This method has already been adopted by various industry members such as Intel and Aurrion (acquired by Juniper) and is discussed in the following section.

1.2 Heterogeneous silicon photonics

As discussed in the previous section, one material system cannot be optimal for everything, and multiple materials must be used to realize highly functional PICs. In a purely monolithic approach to fabrication, different growths of materials are performed at various times during the process. This procedure, termed regrowth, is highly dependent on surface quality, and often restricted by the need to match the lattice constant of various materials. This not only decreases the possibilities of material combinations, but also adds significant fabrication complexity and reduces yield.

Heterogeneous integration refers to the combination of multiple materials (often dissimilar in structure and properties) onto a common substrate wafer. For this work, the substrate wafer is an SOI wafer, and the materials are transferred onto the wafer using wafer bonding procedures. Critically, the material transfer takes place in an unprocessed state, and the bonded materials are processed together, often at a wafer level scale. This is contrast to hybrid integration, in which the laser and the silicon PIC

are processed separately and assembled afterwards. There is some confusion regarding these terms, as the first heterogeneous silicon laser was given the name “hybrid silicon laser” [6], but the difference in methodology is clear. Compared with hybrid integration, heterogeneous integration is more suitable for volume production, and often wins in terms of size, power, weight, and cost (SWaP+C). In many applications there is also tremendous advantage in having all devices integrated on a single chip, as it is resistant to mechanical shock, vibrations, and other environmental factors.

The advancement in heterogeneous silicon photonics is also illustrated by the rapid scaling of heterogeneous silicon PICs, which has gone from several devices to hundreds of devices in just under a decade [7]. However, as the number of elements increases, the potential for undesired reflections in the PIC also increase. Reflections can come from any source of mode mismatch such as abrupt waveguide bends, tapered transitions, and facets shown in Figure 1.1. Some sources of reflection are shown in If the reflection is significant, it can cause undesired Fabry-Perot-like cavities to form within the PIC. This issue is exacerbated when on-chip lasers are present, as these are very sensitive to reflections. The conventional solution in optics is to place an optical isolator directly after the laser, which blocks all reflections from reaching the laser.

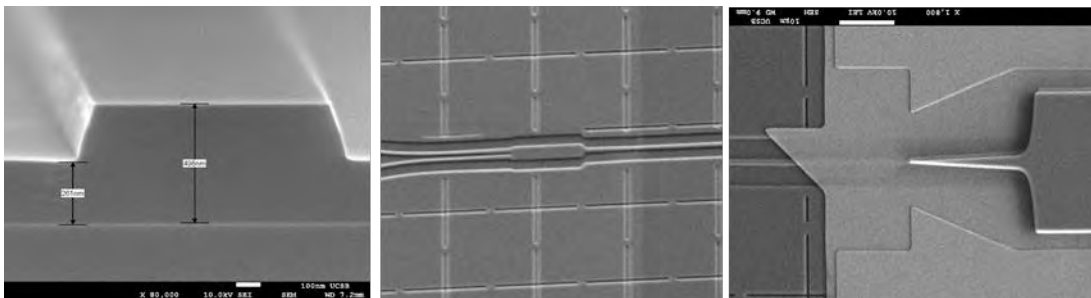


Figure 1.1: SEM images of potential reflections in a PIC from facets, MMIs, and tapers.

An extension of an isolator is an optical circulator, which can take the backwards propagating light and direct it somewhere else. Thus, it is able to separate counterpropagating signals. Optical isolators and circulators can also be found in many applications beyond just eliminating unwanted reflections. They are advantageous to have in any system involving optical amplifiers, and absolutely necessary in the case that bidirectionality is desired [8]. Optical circulators are commonly found in wavelength division multiplexed (WDM) systems in conjunction with gratings. They are also crucial components in interferometric sensors (Sagnac type) or distributed sensing (OFDR). PICs involving optical isolators and circulators are discussed in more detail in Chapter 7. A depiction of the use of these devices is shown in Figure 1.2. Despite these advantages, there is not a single PIC today that actually uses an integrated isolator to the best of the researcher's knowledge. This primarily stems from fabrication related challenges in integrating optical isolators with lasers, modulators, and other critical photonic devices. Heterogeneous integration has been proposed as a way to overcome these challenges [9]. The vision for this is shown in Figure 1.3, in which all the relevant PIC components are integrated together on a common SOI wafer. This is done through bonding multiple dies of different material onto the wafer, which has previously been demonstrated with III-V materials [10,11].

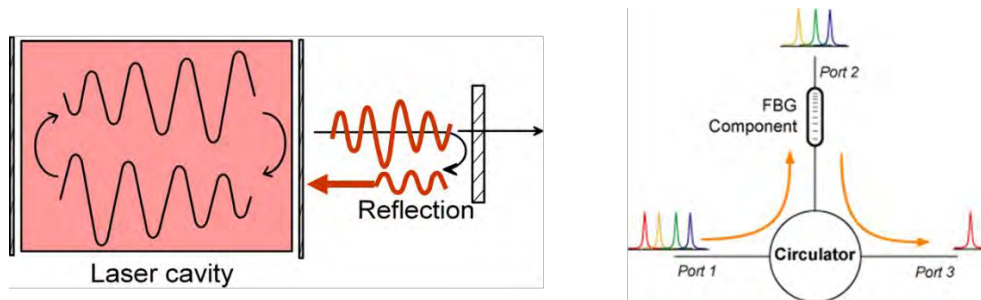


Figure 1.2: Example of a reflection that can destabilize a laser cavity without an isolator, as well as the use of a circulator to separate counterpropagating signals.

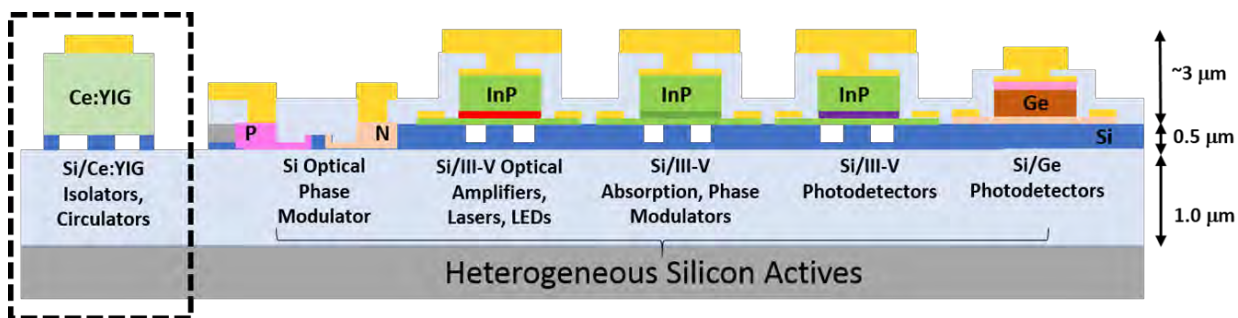


Figure 1.3: Schematic of all the components that have been realized on the heterogeneous silicon platform.

1.3 Optical Nonreciprocity

Optical isolators, in many ways analogous to the electronic diode, are unique in their ability to break the reciprocal nature of light and only block light in one direction. They are essential in preventing unwanted reflected light from reaching the optical cavity, while simultaneously maintaining the desired output power. Optical circulators extend the principle of an optical isolator by rerouting the backwards propagating light to an additional port. Thus, it is able to separate counterpropagating signals.

Mathematically, optical isolators and circulators are devices that break Lorentz reciprocity. Lorentz reciprocity does not hold up in cases in which the medium of

interest has an asymmetric or nonlinear permittivity tensor or has time dependence. This can be depicted as a device with asymmetric scattering matrix as shown in Figure 1.4, in which a and b represent the field components entering and exiting the device respectively. They are characterized by allowing the propagation of light in one specific direction, such that their scattering matrix is non-symmetric [12].

$$\begin{pmatrix} b_1 \\ b_2 \\ b_3 \\ b_4 \\ \vdots \end{pmatrix} = \begin{bmatrix} S_{11} & S_{12} & S_{13} & S_{14} & \dots \\ S_{21} & S_{22} & S_{23} & S_{24} & \dots \\ S_{31} & S_{32} & S_{33} & S_{34} & \dots \\ S_{41} & S_{42} & S_{43} & S_{44} & \dots \\ \vdots & \vdots & \vdots & \vdots & \ddots \end{bmatrix} \begin{pmatrix} a_1 \\ a_2 \\ a_3 \\ a_4 \\ \vdots \end{pmatrix}$$

Figure 1.4: Scattering matrix of any photonic component relating the input fields to the output fields.

It is important to note that there exists a class of devices which have been classified as optical diodes. These also demonstrate different forward and backward transmission, but differ from optical isolators, as they do not show optical nonreciprocity. The classic example of this is an abrupt transition from a single-mode waveguide (fiber) and a multimode waveguide (fiber). Going from single to multimode, the power transmission should be near unity, with some distribution of power among all the modes supported in the multimode region. Going the other way around, if the fundamental mode in the multimode section is excited, not all of it will transmit into the single-mode section, so the transmission will be less than one. However, this is not an isolator. If the same superposition of modes corresponding to the result of the forward transmission are excited in the multimode region for the backward transmission, the backward transmission should be near unity. This is the principle of optical reciprocity. Whatever

happens in the forward direction can be “undone” by doing the opposite in the reverse direction. Optical isolators should block all backwards propagating light, regardless of what combination of modes are used. This topic has been extensively debated in literature [12–14].

Another key difference between optical diodes and isolators is that isolators need to work when both forward and backward propagating light are present simultaneously in the device. Most lasers will emit in continuous wave, so that there is always a forward propagating wave. This rules out a class of devices such as an add-drop ring resonator with asymmetric coupling values to differentiate the quality factor in the forward and backward direction in such a way that nonlinear effects are only observed in one direction [15]. This breaks down when light is propagating in both directions, as the nonlinear effects will always be observed, and the device becomes purely reciprocal.

Thus, Lorentz reciprocity must be broken. This can be effectively broken in three different ways: i) by spatiotemporal modulation (STM) of the refractive index; ii) exploiting nonlinear effects (NLE) and iii) using magneto-optical (MO) materials.

In STM case, the nonreciprocity of the device is induced by modulating the refractive index of the waveguide, usually with a microwave [16] or acoustic signal [17]. For a given propagation direction, the modulating signal is used to couple the incident light with different modes or frequencies supported by the waveguide that can then be filtered or radiated out of the device [18]. This modulating signal has no effect on counter-propagating light, as the phase relation between the light and modulating signal is different. Integrated optical isolators have been demonstrated exploiting the electro-optic effects in a travelling wave III-V modulator [19] as well as a tandem phase

modulator [20]. Similar isolators were achieved in silicon [16,21]. No additional materials are needed, making STM based isolators very attractive for integration with lasers. However, the operation of the isolators often requires complex, high-speed drive circuits that can consume large amounts of power. Furthermore, they also suffer from small optical bandwidth, and the results to date have not achieved large isolation.

In the second approach, a NLE is tailored to achieve nonreciprocal behavior. As previously mentioned, not all nonlinear effects can be used for this purpose, as some effects such as Kerr-like nonlinearities are subject to dynamic reciprocity [22]. When a forward and backward propagating signal are simultaneously propagating through the device, the nonreciprocity of the system can break down, and the device cannot be used to perform isolation. Nonlinear effects suitable for isolation are Raman amplification [23], stimulated Brillouin scattering [24], and parametric amplification [25] among others. Like STM based isolators, the NLE isolators do not require materials outside of those commonly found in CMOS or III-V based foundries. However, a drawback of using nonlinear effects is the inherent dependence between optical isolation of the device and the optical power of the incident light. This is undesirable as the feedback to the laser should be minimized regardless of the output power. Furthermore, they also suffer from small isolation bandwidths since they generally rely on phase matching, meaning isolation is only performed at a specific wavelength.

This leads to the focus of this work, which is optical isolators and isolators based on magneto-optic materials. Magneto-optic materials inherently have an asymmetric dielectric tensor when under the influence of a magnetic field, which breaks Lorentz

reciprocity. They are broadband, linear, and widely used in commercial applications today. However, the use of isolators and circulators in PIC continues to elude researchers, as the magnetic materials are difficult to integrate with silicon, III-V, and other commonly used optical materials. This is the basic problem that the work in this thesis aims to solve.

Summary

The rapid growth of integrated optics over the past decades has resulted in increasingly complex photonic integrated circuits that rival their benchtop counterparts in terms of performance. At the same time, PICs have much lower SWaP+C, which opens up a realm of new possibilities. Silicon photonics in particular has benefitted from decades of CMOS expertise, and is an excellent material system to realize complex PIC, with the exception of the laser source. Heterogeneous integration using wafer bonding techniques has already been established as a potential solution and can be extended to include materials outside the traditional III-V materials. This can be utilized to integrate optical isolators and circulators for silicon photonics through the bonding of magneto-optic materials.

Thesis Organization

This thesis is divided into eight chapters. The first chapter has provided an introduction to integrated optics, with a focus on silicon photonics. Heterogeneous integration using wafer bonding is described as a method to partially overcome material incompatibility challenges. This is especially pertinent to this work, as many magnetic

materials are incompatible with silicon based on lattice constant and thermal expansion coefficient mismatch. An introduction to optical isolators and the various methods of achieving optical nonreciprocity is given.

Chapter 2 will cover the background behind using magneto-optic materials to break optical reciprocity. First, the principles behind magnetism and how they relate to optics (i.e. Faraday rotation) are explained. Not all materials are suitable for this application, so an overview of commonly used magneto-optic materials at telecom wavelengths (1.3 or 1.55 micron) is given. The magneto-optic effect gives rise to nonreciprocal loss and nonreciprocal phase shift mechanisms, the latter of which is used as the basis for all devices covered in this work. Finally, the chapter concludes with a comparison of techniques to drive an external magnetic field in the vicinity of the PIC. An integrated electromagnet solution is chosen and used throughout the devices in this work.

Chapter 3 covers the design, simulation, fabrication, and characterization of microring based isolators. Microrings are widely used in silicon photonics due to their small footprint, power consumption, and other unique properties described in this chapter. Both microring isolators and circulators are fabricated and measured, showing excellent performance. The use of an integrated electromagnet greatly shrinks the size of the microring optical isolator, rendering it more suitable for integration.

Chapter 4 covers the design, simulation, fabrication, and characterization of nonresonant, Mach-Zehnder type isolators and circulators. These address a crucial drawback of the microring isolator, which is their small operating bandwidth. The integrated electromagnet additionally serves as a thermal tuning mechanism, which can be used to compensate for any fabrication inaccuracies.

Chapter 5 covers the efforts to change the operating polarization of the devices in Chapters 3 and 4 from TM to TE, which is the preferred polarization of most semiconductor lasers. This can be done either by altering the cross-section of the waveguides, or by including a polarization rotator in front of the isolator. Ultimately, the polarization rotator solution was chosen, as it maintains the optimal magneto-optic material quality.

Furthermore, it ensures that the fabrication of the optical isolator is compatible with that used for integrated lasers, which is the subject of Chapter 6. Thermal budget is the primary concern, and the challenges and potential solutions are described. Ongoing efforts to integrate the isolator with a laser on silicon are detailed in this chapter.

Chapter 7 covers some examples of isolators and circulators in photonic integrated circuits. Magneto-optic effects can also be used beyond just these devices, and two examples are given in a magneto-optic switch as well as a magnetic or current sensor. Finally, Chapter 8 provides a conclusion, as well as a personal perspective regarding the challenges overcome in this work, as well as challenges that remain. A future outlook for integrated optical isolators and circulators is given, reflecting the personal opinions of the researcher.

References

1. H. Rong, R. Jones, A. Liu, O. Cohen, D. Hak, A. Fang, and M. Paniccia, "A continuous-wave Raman silicon laser," *Nature* **433**, 725–728 (2005).
2. S. Wirths, R. Geiger, N. V. Den Driesch, G. Mussler, T. Stoica, S. Mantl, Z. Ikonik, M. Luysberg, S. Chiussi, J. M. Hartmann, H. Sigg, J. Faist, D. Buca, D. Grützmacher, N. Von Den Driesch, G. Mussler, T. Stoica, S. Mantl, Z. Ikonik, M. Luysberg, S. Chiussi, J. M. Hartmann, H. Sigg, J. Faist, D. Buca, and D. Grützmacher, "Lasing in direct-bandgap GeSn alloy grown on Si," *Nat. Photonics* **9**, 88–92 (2015).

3. R. E. Camacho-Aguilera, Y. Cai, N. Patel, J. T. Bessette, M. Romagnoli, L. C. Kimerling, and J. Michel, "An electrically pumped germanium laser," *Opt. Express* **20**, 11316 (2012).
4. D. Jung, Z. Zhang, J. Norman, R. Herrick, M. J. Kennedy, P. Patel, K. Turnlund, C. Jan, Y. Wan, A. C. Gossard, and J. E. Bowers, "Highly Reliable Low-Threshold InAs Quantum Dot Lasers on On-Axis (001) Si with 87% Injection Efficiency," *ACS Photonics* **5**, 1094–1100 (2018).
5. J. C. Norman, D. Jung, Y. Wan, and J. E. Bowers, "Perspective: The future of quantum dot photonic integrated circuits," *APL Photonics* **3**, (2018).
6. A. W. Fang, H. Park, O. Cohen, R. Jones, M. J. Paniccia, and J. E. Bowers, "Electrically pumped hybrid AlGaInAs-silicon evanescent laser," *Opt. Express* **14**, 9203 (2006).
7. C. T. Santis, M. Davenport, T. Komljenovic, S. Srinivasan, J. E. Bowers, E. J. Stanton, A. Y. Liu, A. Spott, C. Zhang, J. Hulme, M. Davenport, J. Hulme, A. Y. Liu, C. T. Santis, A. Spott, S. Srinivasan, E. J. Stanton, C. Zhang, and J. E. Bowers, "Heterogeneous Silicon Photonic Integrated Circuits," *J. Light. Technol.* **34**, 20–35 (2015).
8. P. Pintus, N. Andriolli, F. Di Pasquale, and J. E. Bowers, "Bidirectional crosstalk and back-reflection free WDM active optical interconnects," *IEEE Photonics Technol. Lett.* **25**, 1973–1976 (2013).
9. D. Huang, P. Pintus, and J. E. Bowers, "Towards heterogeneous integration of optical isolators and circulators with lasers on silicon [Invited]," *Opt. Mater. Express* **8**, 2471–2483 (2018).
10. H.-H. Chang, Y. Kuo, R. Jones, A. Barkai, and J. E. Bowers, "Integrated hybrid silicon triplexer.," *Opt. Express* **18**, 23891–23899 (2010).
11. S. Keyvaninia, M. Muneeb, S. Stanković, P. J. Van Veldhoven, D. Van Thourhout, and G. Roelkens, "Ultra-thin DVS-BCB adhesive bonding of III-V wafers, dies and multiple dies to a patterned silicon-on-insulator substrate," *Opt. Mater. Express* **3**, 35 (2013).
12. D. Jalas, A. Petrov, M. Eich, W. Freude, S. Fan, Z. Yu, R. Baets, M. Popović, A. Melloni, J. D. Joannopoulos, M. Vanwolleghem, C. R. Doerr, and H. Renner, "What is-and what is not-an optical isolator," *Nat. Photonics* **7**, 579–582 (2013).
13. S. Fan, R. Baets, A. Petrov, Z. Yu, J. D. Joannopoulos, W. Freude, A. Melloni, M. Vanwolleghem, D. Jalas, M. Eich, M. Krause, H. Renner, E. Brinkmeyer, and C. R. Doerr, "Comment on "Nonreciprocal light propagation in a silicon photonic circuit,"" *Science* (80-.). 5–6 (2012).
14. L. Feng, M. Ayache, J. Huang, Y.-L. Xu, M.-H. Lu, Y.-F. Chen, Y. Fainman, and A. Scherer, "Nonreciprocal Light Propagation in a Silicon Photonic Circuit," *Science*

- (80-). **333**, 729–733 (2011).
15. L. Fan, J. Wang, L. T. Varghese, H. Shen, B. Niu, Y. Xuan, A. M. Weiner, and M. Qi, "An all-silicon passive optical diode," *Science* (80-). **335**, 447–450 (2012).
 16. H. Lira, Z. Yu, S. Fan, and M. Lipson, "Electrically driven nonreciprocity induced by interband photonic transition on a silicon chip," *Phys. Rev. Lett.* **109**, 1–5 (2012).
 17. D. B. Sohn, S. Kim, and G. Bahl, "Time-reversal symmetry breaking with acoustic pumping of nanophotonic circuits," *Nat. Photonics* **12**, 91–97 (2018).
 18. Z. Yu and S. Fan, "Complete optical isolation created by indirect interband photonic transitions," *Nat. Photonics* **3**, 91–94 (2009).
 19. S. Bhandare, S. K. Ibrahim, D. Sandel, H. Zhang, F. Wüst, and R. Noé, "Novel nonmagnetic 30-dB traveling-wave single-sideband optical isolator integrated in III/V material," *IEEE J. Sel. Top. Quantum Electron.* **11**, 417–421 (2005).
 20. C. R. Doerr, N. Dupuis, and L. Zhang, "Optical isolator using two tandem phase modulators," *Opt. Lett.* **36**, 4293 (2011).
 21. C. R. Doerr, L. Chen, and D. Vermeulen, "Silicon photonics broadband modulation-based isolator," *Opt. Express* **22**, 4493 (2014).
 22. Y. Shi, Z. Yu, and S. Fan, "Limitations of nonlinear optical isolators due to dynamic reciprocity," *Nat. Photonics* **9**, 388–392 (2015).
 23. M. Krause, H. Rentier, and E. Brinkmeyer, "Optical isolation in silicon waveguides based on nonreciprocal Raman amplification," *Electron. Lett.* **44**, (2008).
 24. C. H. Dong, Z. Shen, C. L. Zou, Y. L. Zhang, W. Fu, and G. C. Guo, "Brillouin-scattering-induced transparency and non-reciprocal light storage," *Nat. Commun.* **6**, 1–6 (2015).
 25. S. Hua, J. Wen, X. Jiang, Q. Hua, L. Jiang, and M. Xiao, "Demonstration of a chip-based optical isolator with parametric amplification," *Nat. Commun.* **7**, 1–6 (2016).

Chapter 2

Magneto-optic Effects

The study of magneto-optics involves a number of phenomenon that occur when an electromagnetic wave such as light travels through a material that is under the influence of an external, quasi-static magnetic field. Such medium is also known as gyrotropic material. The origin of these effects dates to 1845, when Michael Faraday showed the first experimental evidence that light and electromagnetism were related. In his work, Faraday was able to measure the rotation of the polarization of light under the influence of a magnetic field as it travelled through a piece of glass with traces of lead [1]. Thus, he was successful in “magnetizing a ray of light”, as he remarked in his journal. This effect is now known as Faraday rotation and is widely used in bulk and free-space optical isolators and circulators today. In this section, a brief overview of magneto-optic effects and their applications in waveguides is given. While some basic theory and origins of the effects are given, a much more detailed explanation can be found in physics textbooks. Regarding magneto-optics for integrated optics, a number of excellent reviews have been published on this subject [2–9].

2.1 Faraday Rotation

Faraday rotation describes the birefringence that arises between the two orientations of circularly polarized light when under the influence of a magnetic field. Critically, the sign of this circular birefringence, as defined as the refractive index difference between right hand polarized (RHP) and left hand polarized (LHP) light is dependent on the direction of propagation (\vec{k}) with respect to the direction of the applied magnetic field (\vec{H}). In the Faraday configuration, \vec{k} and \vec{H} must be either parallel or antiparallel. This dependence on propagation direction is also the origin of nonreciprocity. Any linear polarization of light can be decomposed as a superposition of the RHP and LHP states of light, which is defined in Equations 2.1-2.3. The Cartesian coordinate system referenced in these equations is given in Figure 2.1

$$\mathbf{E}_{RHP} = E_0[\cos(kz - \omega t)\hat{x} - \sin(kz - \omega t)\hat{y}] \quad (2.1)$$

$$\mathbf{E}_{LHP} = E_0[\cos(kz - \omega t)\hat{x} + \sin(kz - \omega t)\hat{y}] \quad (2.2)$$

$$\mathbf{E}_{Lin} = \frac{\mathbf{E}_{LHP} \pm \mathbf{E}_{RHP}}{2} \quad (2.3)$$

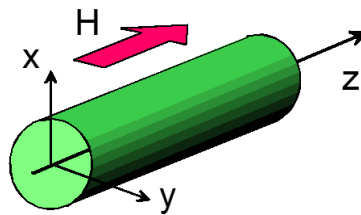


Figure 2.1: Schematic of Cartesian coordinate system used for analysis of a Faraday rotator in which light and magnetic field are parallel.

Here, the wave is assumed to be propagating in the z-direction, which is parallel to the applied magnetic field. Circular birefringence will cause a handedness dependence on the refractive index, which is defined as $\Delta n = n_{LHP} - n_{RHP}$. Substituting $k = \bar{n} \left(\frac{2\pi}{\lambda} \right)$ where \bar{n} is the refractive index in absence of magnetic field into the above equations gives the following equations.

$$\mathbf{E} = \frac{E_0}{2} \left[\left(\cos \left(kz - \omega t + \frac{\pi \Delta n z}{\lambda} \right) + \cos \left(kz - \omega t - \frac{\pi \Delta n z}{\lambda} \right) \right) \hat{\mathbf{x}} \right. \\ \left. + \left(\sin \left(kz - \omega t + \frac{\pi \Delta n z}{\lambda} \right) + \sin \left(kz - \omega t - \frac{\pi \Delta n z}{\lambda} \right) \right) \hat{\mathbf{y}} \right] \quad (2.4)$$

$$\mathbf{E} = E_0 \left[\cos \left(\frac{\pi \Delta n z}{\lambda} \right) \hat{\mathbf{x}} + \sin \left(\frac{\pi \Delta n z}{\lambda} \right) \hat{\mathbf{y}} \right] \cos(kz - \omega t) \quad (2.5)$$

The polarization of light is rotated by an angle ϕ with respect to the incident polarization.

$$\phi = \frac{\pi \Delta n z}{\lambda} \quad (2.6)$$

The value of Δn can be derived either quantum mechanically, or classically. From a quantum mechanical point of view, the magnetic field causes a splitting in the Landau levels of the electrons, which is known as Zeeman splitting. The levels are split depending on the spin of the particle, which is tied to the handedness of the polarization. This splitting of the energy levels results in different transition energies in the system, which affects the imaginary component of dielectric function $\varepsilon(\omega)$. Finally, the real part of $\varepsilon(\omega)$ is also changed due to Kramer-Kronig relations, which results in the circular

birefringence and Faraday rotation discussed in this section. Further details can be found in [10].

Classically, it is well known that electrons in an external magnetic field obey the Lorentz law of motion. More specifically, electrons will spin around the axis of the magnetic field with an angular frequency known as the Larmor frequency of $\omega_L = eB/2m$. Here, e and m are the charge and mass of an electron respectively. When circularly polarized light with frequency ω_0 is propagating through such a medium, the relative angular frequency between the electrons and light will be either higher or lower than that of the unmagnetized medium, depending on the handedness of the light. Thus, $\Delta n = 2 \frac{dn}{d\omega} \omega_L$, as long as $\omega_L \ll \omega_0$. This can be expanded as the following in Equation 2.7

$$\Delta n = \left(\frac{eB}{m}\right) \frac{dn}{d\omega} = \left(\frac{eB}{m}\right) \left(\frac{-\lambda^2}{2\pi c}\right) \frac{dn}{d\lambda} \quad (2.7)$$

Finally, we combine Equation 2.6 with Equation 2.7 To obtain the following expression for Faraday rotation of light over an interaction length (d) [11].

$$\phi = -\frac{e}{2mc} \left(\lambda \frac{dn}{d\lambda}\right) Bd = VBd \quad (2.8)$$

The dependence between B and ϕ is linear over a fixed interaction length. This linear constant is known as the Verdet constant (V) [12]. The Verdet constant has units of [rad/T•m] and is strongly dependent on the optical wavelength. Strictly speaking, Equation 2.8 only holds true for diamagnetism, which is present in all materials. Equation 2.8 is often modified with an empirical correction factor between zero and one

to fit the measured Verdet constant for different materials and different types of magnetism (diamagnetic, paramagnetic, ferromagnetic, or ferrimagnetic). The differences in these magnetic materials is expanded on in Section 2.2. Far away from the absorption lines, the refractive index of transparent media can be modelled using Cauchy's Law, which gives an inverse squared dependence between refractive index and wavelength. Thus, the Verdet constant also has a $1/\lambda^2$ dependence based on Equation 2.8, providing an inherent tradeoff between strength of magneto-optic interaction and the optical loss at longer wavelengths. Finally, the Verdet constant is known to be temperature sensitive. Generally, Faraday rotation will decrease at higher temperatures.

As previously mentioned, the most common use of Faraday rotation in optics is to make optical isolators. The operating principle of the simplest Faraday optical isolator is depicted below in Figure 2.2.

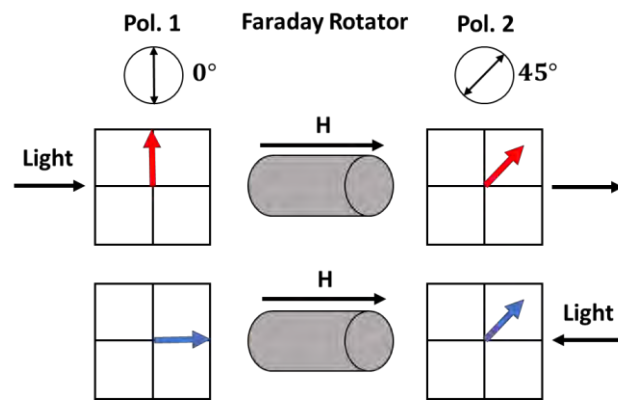


Figure 2.2: Schematic of a polarization dependent optical isolator

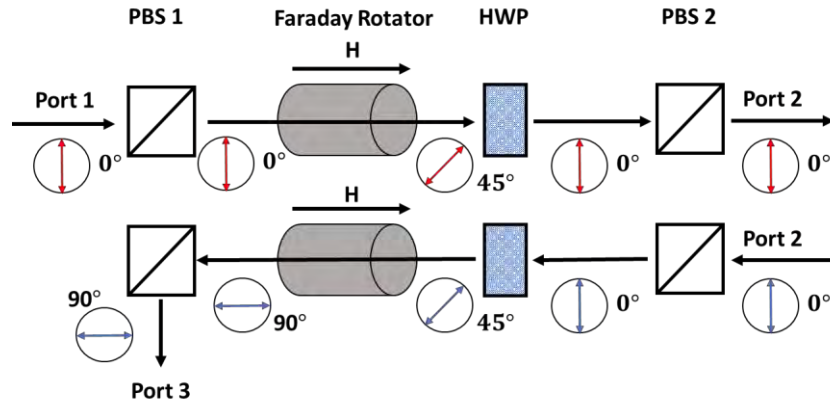


Figure 2.3: Schematic of a polarization dependent optical circulator

This polarization dependent Faraday isolator consists of two linear polarizers orientated at 0 and 45 degrees, and a 45-degree Faraday rotator in between. The key element is the Faraday rotator, which comprises of a magneto-optic material and a static magnetic field. Backwards propagating light is polarized 90 degrees after the Faraday rotator, so it can be filtered out by the polarizer. An optical circulator can be realized by including an additional half-wave plate as well as use of polarization beam splitters, as shown in Figure 2.3. The combination of the nonreciprocal 45-degree Faraday rotator and reciprocal 45-degree half-wave plate rotator causes the polarization of the backwards propagating light to be rotated by 90 degrees, where it is split off using the polarization beam splitter.

It is worth noting that the schematics shown here are polarization dependent since they require the input light to be aligned with the polarizer. In most fiber-optic applications, polarization independent isolators and circulators are used, since polarization is easily scrambled in single mode fiber. These have a slightly different design, making use of birefringent crystals to physically displace the beam instead of

polarizers [13]. However, the use of Faraday rotation to provide nonreciprocal polarization rotation is central to all designs.

2.2. Magneto-optic materials

While this is by no means an extensive overview of magnetic materials, this section introduces several classes of materials that have been studied for magneto-optic applications. To begin with, magnetism is divided into several classifications, which are listed below.

- Diamagnetism occurs in all materials, regardless of composition. It is the weakest effect, and is a repulsive force (negative susceptibility), rather than an attractive force. The origins can be tied back to the orbitals of electrons being affected by the external magnetic field in such a way that it internally produces a magnetic field with an opposite sign. Classically, this is tied to Lenz's law and Faraday's law.
- Paramagnetism is an attractive force and found in materials with unpaired electrons (unfilled orbitals). Some (or all) of the magnetic dipoles align up with the external field, resulting in a net magnetization in the same direction of the external field. However, the remnant magnetization is very weak, and the dipoles return to random configurations if the external field is removed. Common paramagnetic materials include aluminum and magnesium.
- Ferromagnetism refers to the concept of permanent magnets, in which the material retains magnetization even in the absence of external magnetic fields. These materials such as iron, cobalt, or gadolinium also have unpaired electrons and magnetic dipole moments. Locally aligned "pieces" of the material are known

as magnetic domains, which are randomly orientated so that the overall magnetization is zero (much like paramagnetism, but on a much larger scale). The difference is that ferromagnets have strong remnance and coercivity, meaning that once the magnetic domains are aligned, they tend to stay aligned and magnetized. This is due to a quantum mechanical effect known as exchange interaction. An intuitive way to think of this is that the dipoles are kept in alignment by neighboring dipoles, since it is energetically favorable. Therefore, they tend to stay aligned even after the external field is removed, until they are demagnetized (by temperature, or other magnetic fields). Materials that are easily magnetized and demagnetized with little to no hysteresis effects are known as soft magnetic materials. On the other hand, materials with large hysteresis loops are known as hard magnetic materials.

- Antiferromagnetism is similar to ferromagnetism, but the adjacent dipoles align up in antiparallel direction, rather than parallel. Generally, this effect is only seen at low temperatures.
- Ferrimagnetism is somewhere in between ferromagnetism and antiferromagnetism. It consists of two populations of atoms that have dipoles oriented in opposite directions, but with unequal magnetic moments. Therefore, a net magnetization remains. The most common ferrimagnets are garnets and ferrites. Most of the magnetic materials used in this work fall under this category of magnetism.

When considering materials for integrated magneto-optic applications, four important aspects of the material should be considered, which are listed below.

1. Maximum Faraday rotation of the material [deg/cm]
2. Optical loss [dB/cm]
3. Saturation magnetization [Oe]
4. Ease of integration with semiconductors (silicon, III-V, etc)

The first two parameters are often quoted together (Faraday rotation/optical loss) to provide a figure of merit [deg/dB]. Together, it provides a measure of how useful the material is for magneto-optic applications. One should note that in the interest of integration, device size is very important, so the figure of merit should not be blindly accepted. Given the same figure of merit, a material with larger Faraday rotation and optical loss is preferable to a material with lower Faraday rotation since the resulting device will be smaller. The third parameter is not as often stated but is very relevant when considering integration. Given the need to integrate an optical isolator on chip with lasers, other PIC elements, and electronic drivers in a small package, it may not be feasible to apply fields on the order of one Tesla to saturate the magnetization. Doing so would require strong external magnets, which add significant bulk in addition to significant headache when considering how to package the PIC. Finally, the ability to integrate the isolator with semiconductors (with lasers in particular) is important when considering the function of the isolator in a PIC.

Semiconductors themselves have nonzero Faraday rotation due to free carriers and Zeeman splitting of the bands. However, these effects are very weak by themselves, and need to be enhanced. As discussed previously, the Verdet constant for diamagnetic materials follows a $1/\lambda^2$ dependence, so Faraday rotation is stronger as the bandgap energy is approached. However, this significantly increases loss due to absorption, so

the figure of merit remains roughly the same. Researchers have also looked to introduce magnetic dopants such as iron into semiconductors such as InP or InGaAsP [5]. For doping concentrations, up to 10^{17} cm^{-3} , the Faraday rotation was measured to be as high as 125 deg/cm at a field strength of 1 Tesla [14]. This corresponds to a Verdet constant of 218 rad/(T*m). Still, this is one to two orders of magnitude smaller than what can be achieved with garnets.

Just like semiconductors can be doped, it is also possible to introduce ferromagnetic or ferrimagnetic properties by doping dielectrics such as glass. This is interesting because it has very low loss, with ease of integration. Terbium doped fiber has shown Verdet constants of 32 rad/(T*m) at 1060nm [15], and 15.5 rad(T*m) at 1300nm [16]. It is expected to be even lower at 1550nm. These low values mean large devices sizes are needed, which does not lend itself well to integration.

Due to these low Faraday rotations, most commercial Faraday isolators discussed in the previous section use ferrimagnetic garnets such as terbium gallium garnet ($\text{Tb}_3\text{Ga}_5\text{O}_{12}$), yttrium iron garnet ($\text{Y}_3\text{Fe}_5\text{O}_{12}$), or bismuth substituted iron garnets ($\text{Bi}_3\text{Fe}_5\text{O}_{12}$). Yttrium iron garnets (YIG) substituted with cerium ($\text{Ce}_1\text{Y}_2\text{Fe}_5\text{O}_{12}$) or bismuth ($\text{Bi}_1\text{Y}_2\text{Fe}_5\text{O}_{12}$) have shown the largest figure of merit among iron garnets. A comparison of some MO thin-film materials at telecom wavelengths is summarized below. The wavelength of interest is 1550nm.

Material	Optical Loss [dB/cm]	Faraday Rotation [deg/cm]
$\text{Y}_3\text{Fe}_5\text{O}_{12}$	-	200
Crystalline Ce:YIG on SGGG [17]	14	-4500
Polycrystalline Ce:YIG on Si [18] [19]	58	-1260, -3000
Polycrystalline Bi:YIG on Si [20]	-	-1700
$\text{Tb}_3\text{Ga}_5\text{O}_{12}$ on Si [21]	-	500

Bi:TIG on Si [21]	-	-500
Ce:TIG on Si [22]	-	-3200
CoFe ₂ O ₄ [23]	>1000	24000
Fe:InP or Fe:InGaAsP [14]	1.66	125

Table 2.1: Comparison of Faraday rotation and optical loss for several thin-film magneto-optic materials measured at 1550nm. The materials are either on native substrate or silicon or quartz substrates.

The main challenge regarding these garnets has been integration with semiconductors. The MO material used in this work is cerium substituted yttrium iron garnet (Ce:YIG). It has a lattice constant of 12.57 Å, which is over twice the value of Si (5.431 Å), GaAs (5.6533 Å), and InP (5.8696 Å) [24]. To make matters worse, the coefficient of thermal expansion (CTE) of garnet is $10.4 \times 10^{-6} \text{ K}^{-1}$, which is over three times larger than silicon. This makes it very difficult to grow garnet films on semiconductor substrates with high quality, although it is an area of active research.

The highest quality garnet films are grown on a lattice matched (Ca, Mg, Zr)-substituted gadolinium gallium garnet (SGGG, $n_{\text{SGGG}}=1.97$) substrate, which is commercially available. The preparation of thin film on garnet substrates is performed through liquid-phase epitaxy (LPE), sputtering, or pulsed laser deposition. The Ce:YIG used in this work is prepared by sputter epitaxy by Professor Yuya Shoji and Professor Tetsuya Mizumoto from the Tokyo Institute of Technology. The growth conditions and procedures were developed over 20 years ago, are specified in the following works [25,26]. The Faraday rotation of the film is measured as a function of out-of-plane magnetic field and plotted below in Figure 2.4.

The out-of-plane magnetization for Ce:YIG for which this measurement is taken is considered to be the hard-axis, as it requires almost 2kOe of H-field to saturate. When

the magnetization is saturated, the Faraday rotation measures at -4500 deg/cm, after compensating for the slightly paramagnetic SGGG substrate. The Faraday rotation in the easy-axis (in-plane) is not measured but assumed to saturate at a similar value, albeit at a much lower magnetic field (~ 500 e). Further information on Ce:YIG films can be found in references [20,24,27,28]. A summary of relevant material properties of Ce:YIG is shown in the table below.

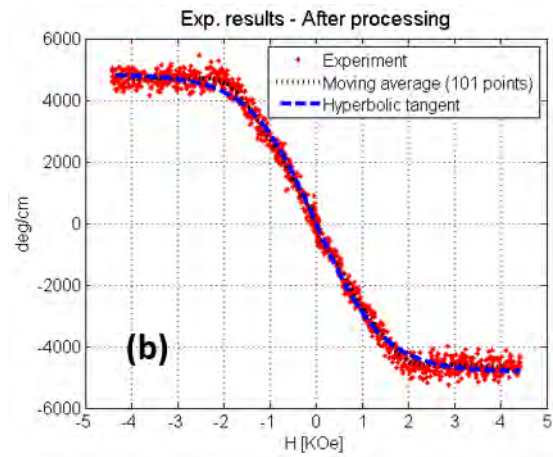


Figure 2.4: Faraday rotation measurement of Ce:YIG/SGGG

Material Parameter @ 1550nm	Value
Refractive Index	2.20
Faraday Rotation	-4500 deg/cm
Saturation (easy axis)	~ 50 Oe
Saturation (hard-axis)	~ 2000 Oe
Optical Loss	10-60dB/cm 40dB/cm in this work
Lattice Constant	12.57 angstroms
CTE	$1.04E-5$ / K
Figure of Merit	112.5 deg/dB

Table 2.2: Selected material parameters of Ce:YIG relevant to this work.

The largest discrepancy in literature is the optical loss, which can vary from roughly 10dB/cm to 60dB/cm depending on the preparation of the film and whether any anneals were performed post-deposition. Other types of magneto-optic materials that have garnered interest include iron oxides (FeO, Fe₂O₃, etc) [29] or cobalt ferrite [23] which show Faraday rotation over 25,000 deg/cm at 1550nm. Unfortunately, this is accompanied with optical losses at the dB/micron scale, which renders the materials unusable for PIC.

2.3 Magneto-optic effect in waveguides

In this section, integrated optical isolators based on magneto-optic effects are discussed. Depending on the orientation of the magnetic field with respect to the waveguide, several magneto-optic effects can be realized. Proper waveguide design can then take advantage of these nonreciprocal effects to achieve optical isolation. Over several decades, many different approaches have been taken. There are three methods that stand out, being nonreciprocal mode conversion, nonreciprocal loss, and nonreciprocal phase shift. The first two methods will be discussed here, while nonreciprocal phase shift is discussed in more detail in Section 2.4 and adopted throughout this work.

Initial work on integrated optical isolators copied the approach used in bulk, Faraday isolators used in free-space and fiber optic systems. This is also the approach that was discussed in Section 2.1. The waveguide equivalent of the approach is a nonreciprocal mode conversion, which is depicted in Figure 2.5. It combines a nonreciprocal mode converter with a reciprocal mode converter to allow forward propagation of TE modes,

while converting backwards propagating TE modes to TM modes, where they can be filtered out. The magnetic field is parallel to the propagation direction.

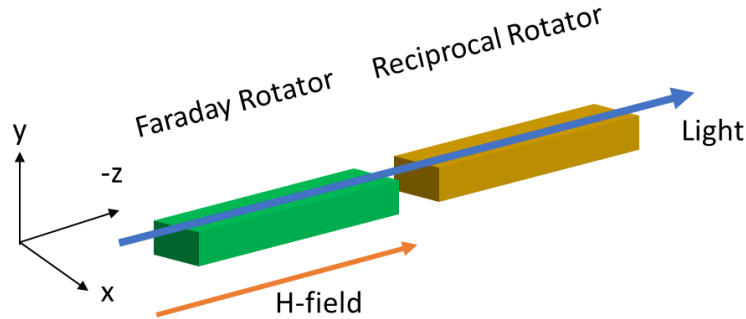


Figure 2.5: Schematic of integrated Faraday rotator based isolator

There are two immediate issues with such a design. One of the primary issues facing integrated Faraday effect isolators in waveguides is the linear birefringence of light. The waveguide cross-section is generally rectangular, such that the effective index and phase constant of the two polarizations of light is different. In fact, this modal degeneracy is usually favorable, as it prevents unwanted mode conversion. The combination of circular birefringence due to Faraday rotation with the linear birefringence from the waveguide leads to an elliptical polarization of light, reducing the mode conversion efficiency. Furthermore, the lack of phase matching causes the principal axis of polarization to oscillate, leading to a beating effect instead of monotonic behavior. The beat length is inversely proportional to the birefringence between the two modes [30], which will be typically on the order of hundreds of microns. The resulting effect from this is the self-cancellation of polarization rotation. The polarization will start converting from TE to TM in one segment, and then backwards in the next segment, as

the phase is mismatched. This causes a great deal of trouble when trying to realize 45 degrees of nonreciprocal polarization rotation.

Significant efforts have been taken to reduce, compensate, or even eliminate the linear birefringence. Given the realities of fabrication, it is practically impossible to realize a perfectly square waveguide, as birefringence should be reduced to the order of 10^{-5} [6]. Also, the deposition of a thin film on a substrate results in stress induced birefringence. Instead, methods to compensate one source of birefringence with another are used such that the net linear birefringence is zero [31]. This usually involves some kind of post-fabrication device etch trimming [32] or capping with another material. Impressive isolations over 32dB were achieved over 150nm [33], although it used an off-axis launch polarization into the waveguide, which is difficult to replicate in a fully integrated platform. Quasi phase-matching can also be used to overcome linear birefringence, as it introduces a spatial modulation parameter to counteract the beat length. As long as the beat length is known, the birefringence can be overcome by flipping the magnetic field periodically [34], or only incorporating the magnetic material periodically [35,36]. However, this is also a highly wavelength selective process, since the beat length is inherently wavelength dependent.

In addition to these “tricks” and workarounds to the birefringence issue, the waveguide Faraday isolator still requires a reciprocal polarization converter. While full TE to TM polarization conversion has been widely studied in silicon photonics [37], and one such converter is presented in Chapter 5, half-polarization, or 45-degree conversion is difficult. As shown in Figure 2.5, the full waveguide Faraday isolator requires a polarizer orientated at a 45-degree angle, or a 45-degree reciprocal polarization rotator.

While commonly found in free-space optics, waveplates are not commonly used in integrated optics due to design and fabrication complexity. Various designs have been demonstrated, utilizing asymmetric waveguide cross-sections such as slanted sidewalls [38,39], slot waveguides [40], or L-shaped waveguides [41], among other designs. Other workarounds have been to incorporate use the magneto-optic Cotton-Mouton effect [42] or radiating the converted mode out by engineering the modal cutoff conditions in the waveguide [17]. While each design has its merits and drawbacks, these are not commonly found photonic components such as power splitters or polarization splitters. As a result, there has not been a fully integrated waveguide Faraday isolator (including the polarization components) on semiconductor substrates to best of our knowledge.

The second method of obtaining efficient nonreciprocity on a semiconductor platform is the nonreciprocal loss effect. There have been several demonstrations of isolators based on this phenomenon, and the basic operating principle and schematic is shown below in Figure 2.6. Essentially, the structure is a III-V semiconductor optical amplifier (SOA) with a magneto-optic coating. Here, the magnetic field is perpendicular to the propagation direction. This is also known as the Voigt configuration.

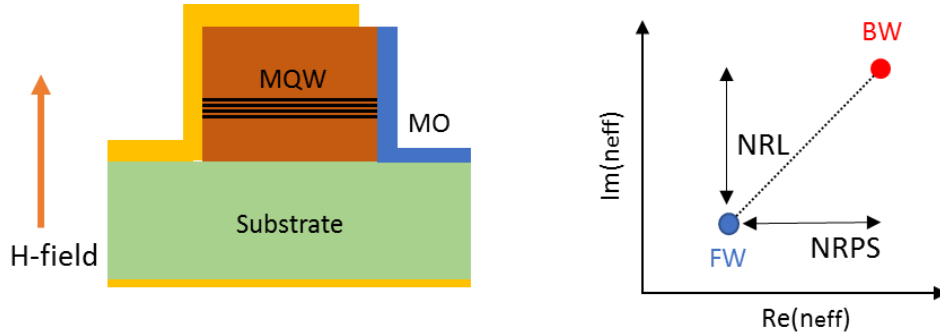


Figure 2.6: Schematic of using a MO waveguide in the Voigt configuration to achieve nonreciprocal loss and phase shift.

In the Voigt configuration, the waveguide experiences a different effective index Δn_{MO} (real and imaginary) for forward and backward direction of light. For NRL based isolators, the waveguide design is such that the imaginary component of Δn_{MO} is large, which leads to different optical loss in the forwards and backwards direction. In the case that the real part of Δn_{MO} is much more significant than the imaginary part (transparent magneto-optic materials), the effect is classified as nonreciprocal phase shift. The origins and derivations of this effect is covered in much more detail in Section 2.4.

Unlike the Faraday isolator, the NRL isolator operates entirely within one polarization, and does not require any phase matching conditions or polarization rotators. This approach makes use of highly absorbing ferromagnetic materials such as iron or cobalt in conjunction with III-V gain material, which can compensate for the optical loss. There have been multiple demonstrations of these devices for TE [43] and TM polarization [44]. Perhaps most importantly of all, the advantage of NRL based isolators is their inherent compatibility with III-V lasers. To date, the only full integration of laser with isolator has been the demonstration of a DFB with NRL based isolator [45]. However, the isolation was only 4dB, which is not sufficient for practical applications.

The forward propagation losses are large (14.1 dB/mm), which is on par with the isolation (14.7 dB/mm) in the device. It is difficult to achieve transparency with the Fe coated SOA. By design, the propagation losses and isolation ratio cannot be decoupled, since larger confinement in the lossy ferromagnetic material is needed to achieve high isolation. Finally, amplified spontaneous emission in the backwards direction from the SOA can never be completely isolated, which will reach the laser diode. As a result, NRL and “active” optical isolators in general may not be applicable to PIC, despite their material and process compatibility with semiconductor lasers.

2.4 Nonreciprocal phase shift

Due to the shortcomings of the Faraday based waveguide isolator and the NRL isolator, researchers turned to NRPS based isolator [46], which should be lower loss than NRL devices and less complex than Faraday isolators. In fact, all the devices discussed in this work operate based on nonreciprocal phase shift (NRPS). As previously mentioned, NRPS arises when the directions of light and magnetic field are perpendicular, known as the Voigt configuration. The following section uses the same coordinate system as Figure 2.1, in which z is out the page, x is vertical, and y is horizontal.

Consider an optical waveguide partially or fully comprised of a magnetic-optic material in an external magnetic field. The permittivity tensor of each material is described by the following equation.

$$\boldsymbol{\varepsilon} = \begin{pmatrix} \varepsilon_{xx} & 0 & 0 \\ 0 & \varepsilon_{yy} & 0 \\ 0 & 0 & \varepsilon_{zz} \end{pmatrix} + K \begin{pmatrix} 0 & M_z & -M_y \\ -M_z & 0 & M_x \\ M_y & -M_x & 0 \end{pmatrix} \quad (2.9)$$

K is a coefficient which has a real part corresponding to Faraday ellipticity, and an imaginary part that is proportional to the Faraday rotation θ_F [2]. For garnets such as Ce:YIG, the Faraday ellipticity is generally ignored. For isolators based on NRL in the previous section, the real part of K is crucial, and cannot be ignored [47]. M is the magnetization of the material, which is proportional to the external magnetic field in that direction. Together, the product can be written as follows [48]. Here, $\theta_F^{x,y,z}$ refers to the saturated Faraday rotation of the material.

$$K \cdot M_{x,y,z} = j \left(\frac{2\theta_F^{x,y,z} \cdot n_0}{k_0} \right) \quad (2.10)$$

Depending on the material used, the magnetization of the material is easier in certain axes, as was previously discussed. Therefore, the Faraday rotation saturates at different field strengths for depending on the orientation of the magnetic fields. When the magnetization is not saturated, a linear dependence between the field strength and Faraday rotation is assumed, as evident by linear nature of the Verdet constant. For the devices in this work, the propagation direction is in the z-axis, while the magnetic field is orientated in the x or y-axis, meaning M_z is equal to zero. Thus, Equation 2.X can be simplified as follows.

$$\boldsymbol{\varepsilon} = \begin{pmatrix} \varepsilon_{xx} & 0 & -KM_y \\ 0 & \varepsilon_{yy} & KM_x \\ KM_y & -KM_x & \varepsilon_{zz} \end{pmatrix} = n_0^2 \begin{pmatrix} 1 & 0 & 0 \\ 0 & 1 & 0 \\ 0 & 0 & 1 \end{pmatrix} + \Delta\boldsymbol{\varepsilon} \quad (2.11)$$

The NRPS is often calculated using perturbation theory, since the off-diagonal terms are much smaller than the diagonal terms, and $\Delta\boldsymbol{\varepsilon}$ can be treated as a perturbation. This approach leads to the following equation for the NRPS ($\Delta\beta$) [49]. It should be noted that $\Delta\beta = \beta^{FW} - \beta^{BW}$, which is double the change from the unperturbed state β .

$$\Delta\beta = \frac{2\omega\varepsilon_0 \iint E^* \Delta\varepsilon E}{\iint (E \times H^* + E^* \times H)_z} dx dy \quad (2.10)$$

This equation can be directly used to calculate the NRPS in any scenario but can be simplified further under some assumptions to provide intuition on how the modal shape should be designed. First, the cases in which the magnetic field is purely x-orientated $\Delta\beta(M_x)$ or y-orientated $\Delta\beta(M_y)$ are considered. Second of all, the semivectorial approximation is used, such that $E_y = 0$ and $E_z = \frac{j}{\beta} \frac{\partial E_x}{\partial x}$ for TE modes, and $E_x = 0$ and $E_z = \frac{j}{\beta} \frac{\partial E_y}{\partial y}$ for TM modes. Already, the polarization dependence of the NRPS is clear. The off-diagonal terms KM_x and KM_y couple the longitudinal field component (E_z) with one of the transverse components (E_y or E_x respectively). If E_x is negligible for TM polarized modes, and E_y is negligible for TE polarized modes, then $\Delta\beta(M_x)$ is only nonzero for TM polarization and $\Delta\beta(M_y)$ is nonzero for TE polarization. Hence, a magnetic field in-plane but perpendicular (x) to light propagation (z) will be referred to as the TM configuration. Likewise, a magnetic field out-of-plane but perpendicular (y) to light propagation (z) will

be referred to as the TE configuration. Under these approximations, the following equations are valid for TM mode NRPS and TE mode NRPS respectively [48].

$$\Delta\beta^{TM}(M_x) = \frac{-4j\omega\varepsilon_0}{\beta^{TM}} \frac{\iint E_y \frac{\partial E_y}{\partial y} (KM_x)}{\iint (E \times H^* + E^* \times H)_z} dx dy \quad (2.12)$$

$$\Delta\beta^{TE}(M_y) = \frac{4j\omega\varepsilon_0}{\beta^{TE}} \frac{\iint E_x \frac{\partial E_x}{\partial x} (KM_y)}{\iint (E \times H^* + E^* \times H)_z} dx dy \quad (2.13)$$

Note that if K is purely imaginary (corresponding to Faraday rotation), the resulting change in β is strictly real, hence the term NRPS. To simultaneously achieve NRPS for both polarizations requires magnetization in both x and y , which has been investigated by several researchers [50–52], although optical isolation has not been realized.

Furthermore, the waveguide geometry is crucial to the calculation of NRPS, as the cross-sectional integral dictates. In fact, only asymmetric profiles result in significant NRPS. To analyze this further, two waveguide geometries are considered, as shown in Figure 2.7. For now, only the fundamental TE and TM mode of each waveguide is considered.

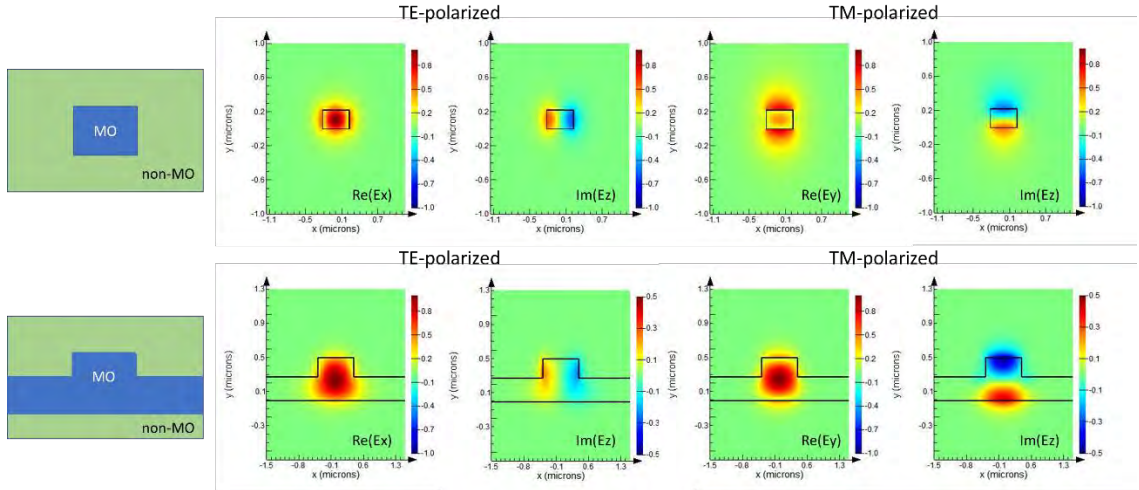


Figure 2.7: Electric field profiles for a strip and rib MO waveguide.

In the first case, a waveguide consists of a strip waveguide made of MO material (assume $n = 3.45$) surrounded by nonmagnetic material (assume $n = 1.45$) such that is symmetric in both x and y directions. The actual indices here are somewhat irrelevant, as the focus is on the symmetry in the waveguide. A strip waveguide has no NRPS for TE or TM modes. The primary field component is exactly even in either direction, meaning its derivative is exactly odd. Therefore, the numerator for either case is exactly an odd function, which will integrate to zero.

In the second case, a rib waveguide is made in the MO material surrounded by nonmagnetic cladding. Such a waveguide is symmetric in x and asymmetric in the y -direction. Therefore, there exists a NRPS for the TM polarization, since E_y is asymmetric in the y -direction. There is no NRPS for the TE polarization, since E_x is exactly even and E_z is exactly odd in the x -direction.

To enhance the NRPS effect, the asymmetry in the waveguide must be increased. This can be done in one of two ways. If the magnetization in the waveguide can also be an odd

function, such as by flipping the magnetization in half the waveguide, the resulting NRPS can be significant, even if the waveguide index profile itself is symmetric. Alternatively, using different materials as cladding on each side increases the asymmetry. In fact, it was proposed that using a semiconductor core with MO cladding on one side of the waveguide provided a significant boost to the NRPS. To illustrate this, the following two waveguide configurations are analyzed in Figure 2.8. Here, only the relevant polarizations to each waveguide configuration is used. The core in the simulation has index 3.45, the MO material has index 2.2, and the non-MO cladding has index 1.45.

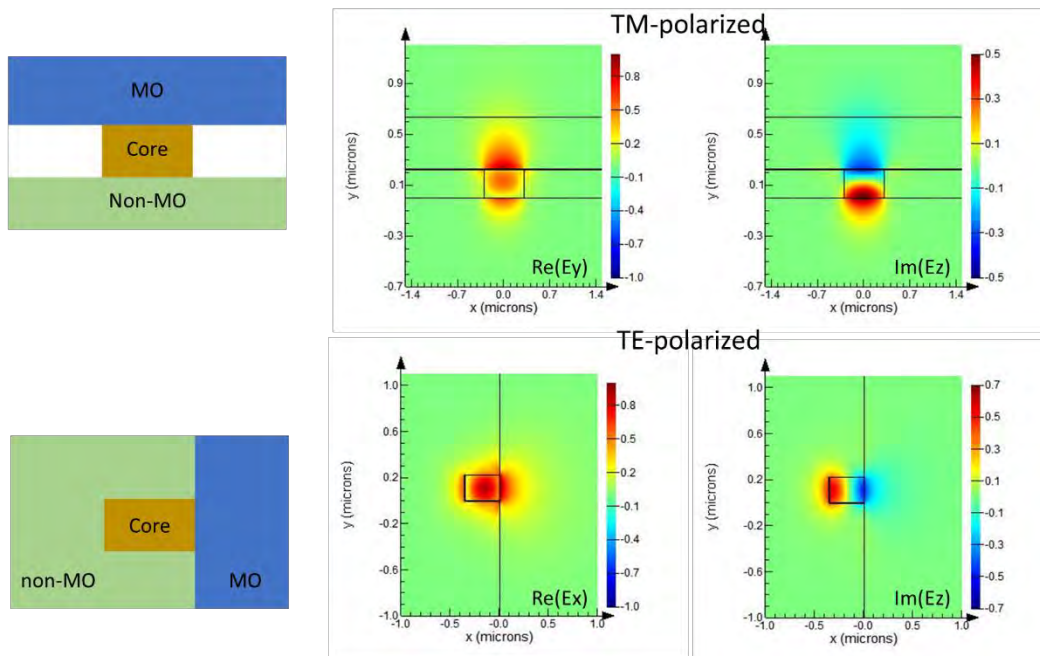


Figure 2.8: Electric field profiles for two waveguides where the MO material is used as the cladding rather than the core.

In the first case, the MO material serves as a cladding and is directly above (or below) a nonmagnetic waveguide, and the TM polarization is considered since the asymmetry is vertical. This is the configuration used for all the devices in Chapters 3 and 4. Only the

field components that penetrate the MO region contribute to the integrals in Equations 2.12 and 2.13. Therefore, the $E_y E_z$ product does not cancel itself out, as the bounds of the integral have essentially been changed to cover half of the odd function E_z . In the second case, the MO material side by side with the semiconductor core. Waveguides using this configuration show significant NRPS for TE polarization, are explored in Chapter 5. In either case, the non-MO cladding should have an index well below the index of the MO cladding to ensure significant modal overlap with the MO material. Therefore, high index contrast platforms such as SOI have the advantage of low contrast III-V or SiN platforms when considering NRPS.

Finally, the placement of the boundary between the core and the MO material is critical. For optimal NRPS, the boundary is placed near the maxima of the mode field. The reasoning behind this is that the boundary causes a discontinuity in $\frac{\partial E_y}{\partial y}$ or $\frac{\partial E_x}{\partial x}$, as it is effectively a delta function, which causes the product to be large. Another potential improvement could be to use MO materials with different magnetizations on each side of the semiconductor core. However, given the materials and platforms available, this was not given serious consideration.

The actual calculation of the NRPS is straightforward provided a modal analysis tool such as Lumerical MODE or FIMMWAVE is available to solve for the necessary field components in Equation 2.10. Alternatively, a finite element mode (FEM) solver taking into account the nonreciprocal effects can be used [53]. For integration of Ce:YIG with silicon waveguides, the difference between the FEM solver and the perturbative approach is only 3%, while the difference between the FEM solver and the semivectorial approximation of the perturbative approach is 10%. In this work, the FEM solver is used

to optimize the waveguide cross-section to provide the largest NRPS. This process is detailed in Chapter 3, and the resulting waveguide is used throughout all the devices in this work.

Once optimized, the NRPS effect can be used in multiple interferometric structures to achieve isolation. Both microring (Chapter 3) and Mach-Zehnder (Chapter 4) structures are explored. Other device architectures using NRPS have been demonstrated such as nonreciprocal directional couplers [54], nonreciprocal multimode imaging devices [55], and tapered mode converters [56] have been studied, although their performance is limited.

2.5 – Methods for applying a magnetic field

The operation of a MO based isolator requires a magnetic field. Traditionally, an external magnet is packaged with the isolator to provide a static magnetic field. This is undesirable for an integrated isolator, as the magnet adds significant bulk and creates challenges for packaging. It has been shown that latching thin-film garnets can be achieved by incorporating europium during growth to lower the saturation point, offering magnet-free operation [57]. However, the magnetization direction is out-of-plane, and therefore the film must be flipped to be perpendicular to light propagation [58]. This approach has drawbacks when considering the planar nature of waveguides in PIC, as it can only be placed on the edge of the chip or placed in grooves that are pre-etched into the chip.

One solution is to fabricate an electromagnet directly on chip. The electromagnet provides a variable magnetic field strength and a thermal tuning mechanism. This

flexibility is extremely important for an integrated device, as it can account for fabrication imperfections or material variability. For example, the magnetic field can be tuned to be slightly stronger if the Faraday rotation of the garnet is weaker than expected. Furthermore, some isolator geometries such as the microring isolator described in Chapter 3 require a radially orientated magnetic field, which is difficult to achieve with external magnets without compromising the size of the ring [59] or sacrificing overlap between the garnet and the resonator [18].

For an NRPS based optical isolator operating for TM mode, the magnetic field must be transverse to the waveguide, so the electromagnet should be placed on top of the waveguide, as shown in Figure 2.9. This configuration is used in almost all the devices in this work.

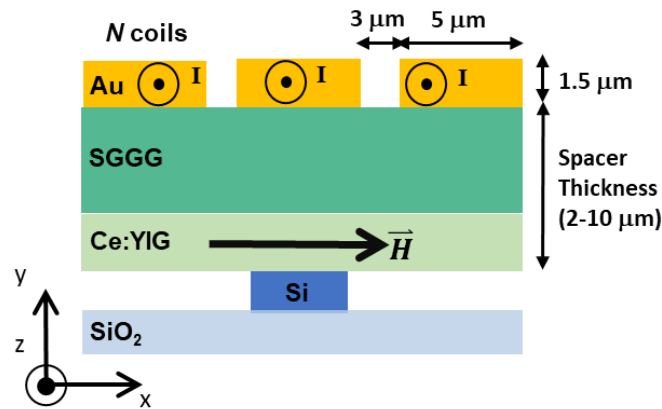


Figure 2.9: Schematic of integrated electromagnet on the backside of the Ce:YIG

Since magnetic field strength decays with distance, it is important to place the electromagnet near the waveguide core. This is also crucial since power dissipation for a given magnetic field in the electromagnet scales quadratically with the distance to the waveguide. Of course, there needs to be a spacer between the MO material and the

electromagnet in order to prevent excess optical loss. The material and thickness of this spacer is determined by the fabrication and process used. For the heterogeneous process, this waveguide to electromagnet distance is minimized by removing the substrate of the bonded garnet, often using a mechanical polishing technique. This is discussed in Chapter 3, and usually results in a spacer layer between 2 and 10 microns thick. A multicoil geometry for the electromagnet can also be adopted to reduce the drive current [60]. While this does not reduce power consumption, it does reduce the power consumption, it reduces the current density in the electromagnet, which is important for avoiding electromigration based failure mechanisms [61]. COMSOL Multiphysics simulations are performed on 1 and 3 coil electromagnets spaced at a distance 2 and 8 microns away from the MO material. The resulting magnetic field and temperature change is shown in Figure 2.10.

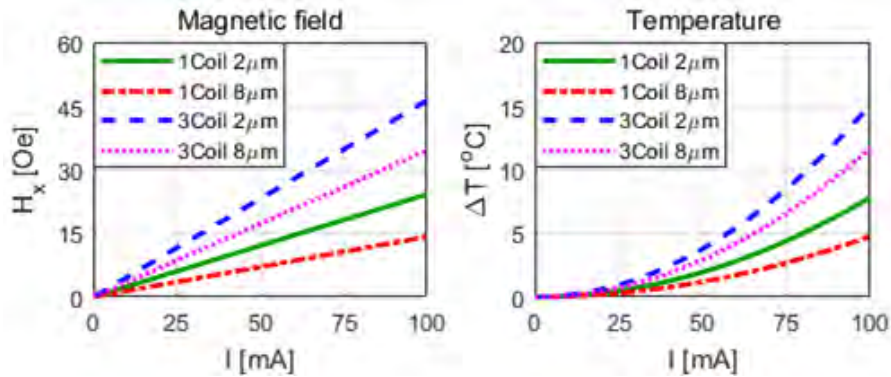


Figure 2.10: Simulations on the magnetic field strength and temperature as a function of spacer thickness and number of coils.

The combined effects of the multicoil electromagnet and thinner spacer layer result in significant improvement in terms of the efficiency of the magnet. However, there are diminishing returns in adding more coils since the outer coils contribute less and less to

the transverse magnetic field. The same goes for reducing spacer layer thickness. In Figure 2.9, a linear shape is assumed for the electromagnet, as it follows a straight waveguide. In the case that the electromagnet is circular, which is useful when it is placed above a ring resonator, the diminishing returns is even more significant, and the resulting magnetic field strength is highly sensitive to the radius of the circle. For practical purposes, 3 coils are enough.

Even with the multicoil solution, the total field strength is on the order of <100 Oe, even when extrapolating Figure 2.10 to higher currents. Therefore, this solution works best when paired with a MO material with low saturation magnetization, such as Ce:YIG in its easy axis (x-direction). When trying to magnetize Ce:YIG in the hard axis, much stronger fields on the order of 2kOe are needed, as was shown in Section 2.2. An integrated electromagnet solution is not practical this point, and stronger magnetic field sources are needed. Testing devices in this configuration is covered in Chapter 5.1.

The major downside with using an integrated electromagnet is the power consumption. One approach could be to deposit a planar thin-film permanent magnet that is deposited on top of the garnet. The remnant magnetization for the easy axis of Ce:YIG is fairly weak [62], and is prone to being demagnetized. Instead, it is possible to deposit a material with high magnetization and coercivity such as samarium cobalt on the backside of the garnet [63]. Once again, a spacer layer such as silica is needed to avoid optical losses in the thin-film magnet. This film can be magnetized locally using an on-chip electromagnet, which allows for more versatile geometries. Ideally, only a short pulse of current is needed to magnetize the thin film, after which it retains the field [64]. This approach is attractive since it maintains a small form factor, while eliminating any

steady state power consumption in the isolator. Further studies should be performed to determine reliability and sensitivity to demagnetization of such an approach.

Summary

Conventional optical isolators and circulators operate based on Faraday rotation, which is a nonreciprocal phenomenon that arises when light interacts with an external magnetic field. This effect can be significantly enhanced by using magneto-optic materials such as the iron garnet family of materials. Incorporating rare earth materials such as cerium, yttrium, or terbium in the garnet are known to further increase Faraday rotation, leading to the selection of cerium-substituted yttrium iron garnet (Ce:YIG) as the material of choice for the devices in this work. When considering waveguide-based isolators and circulators, nonreciprocal phase shift and loss is observed when the magnetic field is placed perpendicular to the waveguide. Nonreciprocal phase shift is the preferred effect among these two, as it is significant even when the magneto-optic material is transparent, which is a key criteria to building photonic integrated circuits. Finally, the source of the magnetic field can also be integrated onto the chip with the use of an electromagnet. For optimal use, the electromagnet can contain multiple coils and should be placed as close to the magneto-optic waveguide as possible. These materials, designs, and effects are exploited to fabricate ring resonator-based isolators (Chapter 3) as well as interferometer-based isolators (Chapter 4).

References

1. M. Faraday, "I. Experimental researches in electricity - Nineteenth series - § 26. On the magnetization of light and the illumination of magnetic lines of force," *Philos. Trans. R. Soc. London* **136**, 1–20 (1846).
2. H. Dötsch, N. Bahlmann, O. Zhuromskyy, M. Hammer, L. Wilkens, R. Gerhardt, P. Hertel, and A. F. Popkov, "Applications of magneto-optical waveguides in integrated optics: review," *J. Opt. Soc. Am. B* **22**, 240 (2005).
3. B. J. H. Stadler and T. Mizumoto, "Integrated magneto-optical materials and isolators: A review," *IEEE Photonics J.* **6**, 1–15 (2014).
4. Y. Shoji, K. Miura, and T. Mizumoto, "Optical nonreciprocal devices based on magneto-optical phase shift in silicon photonics," *J. Opt. (United Kingdom)* **18**, (2015).
5. T. R. Zaman, X. Guo, and R. J. Ram, "Semiconductor waveguide isolators," *J. Light. Technol.* **26**, 291–301 (2008).
6. M. Levy, "The On-Chip Integration of Magneto-optic Waveguide Isolators," *IEEE J. Sel. Top. Quantum Electron.* **8**, 1300–1306 (2002).
7. T. Mizumoto, R. Baets, and J. E. Bowers, "Optical nonreciprocal devices for silicon photonics using wafer-bonded magneto-optical garnet materials," *MRS Bull.* **43**, 419–424 (2018).
8. D. Huang, P. Pintus, and J. E. Bowers, "Towards heterogeneous integration of optical isolators and circulators with lasers on silicon [Invited]," *Opt. Mater. Express* **8**, 2471–2483 (2018).
9. P. Pintus, D. Huang, P. A. Morton, Y. Shoji, T. Mizumoto, and J. E. Bowers, "Broadband TE Optical Isolators and Circulators in Silicon Photonics through Ce:YIG Bonding," *J. Light. Technol.* **8724**, 1–1 (2019).
10. A. Schatz, P. N. McCaffery, "The Faraday Effect," *Q. Rev. Chem. Soc.* **23**, 552–584 (1969).
11. H. Becquerel, "Sur une interprétation applicable au phénomène de Faraday et au phénomène de Zeeman," *C. R. Hebd. Seances Acad. Sci.* **125**, 679–685 (1897).
12. E. Verdet, "Note sur les propriétés optiques des corps transparents soumis à l'action du magnétisme," *Note sur les propriétés Opt. des corps transparents soumis à l'action du magnétisme* **43**, 529–532 (1856).
13. "FIBER OPTIC CIRCULATORS," <https://www.fiberoptics4sale.com/blogs/fiber->

- optic-passive-components/99062406-fiber-optic-circulators.
14. T. R. Zaman, X. Guo, and R. J. Ram, "Faraday rotation in an InP waveguide," *Appl. Phys. Lett.* **90**, (2007).
 15. L. Sun, S. Jiang, and J. R. Marciante, "Compact all-fiber optical Faraday components using 65-wt%-terbium-doped fiber with a record Verdet constant of -32 rad/(Tm)," *Opt. Express* **18**, 12191 (2010).
 16. D. Huang, S. Srinivasan, and J. E. Bowers, "Compact Tb doped fiber optic current sensor with high sensitivity," *Opt. Express* **23**, 29993 (2015).
 17. T. Shintaku, "Integrated optical isolator based on efficient nonreciprocal radiation mode conversion," *Appl. Phys. Lett.* **73**, 1946–1948 (1998).
 18. L. Bi, J. Hu, P. Jiang, D. H. Kim, G. F. Dionne, L. C. Kimerling, and C. A. Ross, "On-chip optical isolation in monolithically integrated non-reciprocal optical resonators," *Nat. Photonics* **5**, 758–762 (2011).
 19. M. Inoue, V. Singh, M. C. Onbasli, D. H. Kim, T. Goto, L. C. Kimerling, C. A. Ross, M. C. Onbasli, D. H. Kim, V. Singh, M. Inoue, L. C. Kimerling, and C. A. Ross, "A nonreciprocal racetrack resonator based on vacuum-annealed magneto-optical cerium-substituted yttrium iron garnet," *Opt. Express* **22**, 19047 (2014).
 20. A. D. Block, P. Dulal, B. J. H. Stadler, and N. C. A. Seaton, "Growth Parameters of Fully Crystallized YIG, Bi:YIG, and Ce:YIG Films With High Faraday Rotations," *IEEE Photonics J.* **6**, 1–8 (2014).
 21. P. Dulal, A. D. Block, T. E. Gage, H. A. Haldren, S. Y. Sung, D. C. Hutchings, and B. J. H. Stadler, "Optimized Magneto-optical Isolator Designs Inspired by Seedlayer-Free Terbium Iron Garnets with Opposite Chirality," *ACS Photonics* **3**, 1818–1825 (2016).
 22. K. Srinivasan and B. J. H. Stadler, "Magneto-optical materials and designs for integrated TE- and TM-mode planar waveguide isolators: a review [Invited]," *Opt. Mater. Express* **8**, 3307 (2018).
 23. M. Yanaga, Y. Shoji, Y. Takamura, S. Nakagawa, and T. Mizumoto, "Compact magneto-optical isolator with cobalt ferrite on silicon photonic circuits," *Appl. Phys. Express* **8**, 8–11 (2015).
 24. X. Y. Sun, Q. Du, T. Goto, M. C. Onbasli, D. H. Kim, N. M. Aimon, J. Hu, and C. A. Ross, "Single-Step Deposition of Cerium-Substituted Yttrium Iron Garnet for Monolithic On-Chip Optical Isolation," *ACS Photonics* **2**, 856–863 (2015).
 25. T. Shintaku and T. Uno, "Related content Preparation of Ce-Substituted Yttrium Iron Garnet Films for Magneto-Optic Waveguide Devices," *Japanese J. Appl.*

- Physics, Part 1 Regul. Pap. Short Notes Rev. Pap. **35**, 4689–4691 (1996).
26. T. Shintaku, A. Tate, and S. Mino, "Ce-substituted yttrium iron garnet films prepared on sputter epitaxy Ce-substituted yttrium iron garnet films prepared on Gd₃Sc₂Ga₃O₁₂ garnet substrates by sputter epitaxy," *Appl. Phys. Lett.* **71**, 1640–1642 (1997).
 27. T. Goto, M. C. Onba, C. A. Ross, M. C. Onbaşlı, and C. A. Ross, "Magneto-optical properties of cerium substituted yttrium iron garnet films with reduced thermal budget for monolithic photonic integrated circuits Taichi," *Opt. Express* **20**, 163–166 (2012).
 28. M. C. Onbasli, L. Beran, M. Zahradník, M. Kucera, R. Antoš, J. Mistrík, G. F. Dionne, M. Veis, and C. A. Ross, "Optical and magneto-optical behavior of Cerium Yttrium Iron Garnet thin films at wavelengths of 200-1770 nm," *Sci. Rep.* **6**, 1–10 (2016).
 29. T. Tepper, F. Ilievski, C. A. Ross, T. R. Zaman, R. J. Ram, S. Y. Sung, and B. J. H. Stadler, "Magneto-optical properties of iron oxide films," *J. Appl. Phys.* **93**, 6948–6950 (2003).
 30. D. C. Hutchings, B. M. Holmes, C. Zhang, P. Dulal, A. D. Block, S. Y. Sung, N. C. A. Seaton, and B. J. H. Stadler, "Quasi-phase-matched faraday rotation in semiconductor waveguides with a magneto-optic cladding for monolithically integrated optical isolators," *IEEE Photonics J.* **5**, 6602512 (2013).
 31. R. Wolfe, V. J. Fratello, and M. McGlashan-Powell, "Thin-film garnet materials with zero linear birefringence for magneto-optic waveguide devices (invited)," *J. Appl. Phys.* **63**, 3099–3103 (1988).
 32. R. Wolfe, R. A. Lieberman, V. J. Fratello, R. E. Scotti, and N. Kopylov, "Etch-tuned ridged waveguide magneto-optic isolator," *Appl. Phys. Lett.* **56**, 426–428 (1990).
 33. R. Wolfe, J. F. Dillon, R. A. Lieberman, and V. J. Fratello, "Broadband magneto-optic waveguide isolator," *Appl. Phys. Lett.* **57**, 960–962 (1990).
 34. P. K. Tien, R. J. Martin, R. Wolfe, R. C. Le Craw, and S. L. Blank, "Switching and modulation of light in magneto-optic waveguides of garnet films," *Appl. Phys. Lett.* **21**, 394–396 (1972).
 35. C. Zhang, P. Dulal, B. J. H. Stadler, and D. C. Hutchings, "Monolithically-Integrated TE-mode 1D Silicon-on-Insulator Isolators using Seedlayer-Free Garnet," *Sci. Rep.* **7**, 1–8 (2017).
 36. D. C. Hutchings, S. Member, B. M. Holmes, A. D. Block, B. J. H. Stadler, S. Member, D. C. Hutchings, S. Member, and B. M. Holmes, "Quasi-Phase-Matched Faraday Rotation in Semiconductor Waveguides With a Magneto-optic Cladding for Monolithically Integrated Optical Isolators Quasi-Phase-Matched Faraday

- Rotation in Semiconductor Waveguides With a Magneto-optic Cladding for Monolithically," *IEEE Photonics J.* **5**, 6602512 (2013).
37. D. Dai, L. Liu, S. Gao, D.-X. Xu, and S. He, "Polarization management for silicon photonic integrated circuits," *Laser Photon. Rev.* **7**, 303–328 (2013).
 38. J. Z. Huang, R. Scarmozzino, G. Nagy, M. J. Steel, and R. M. Osgood, "Realization of a compact and single-mode optical passive polarization converter," *IEEE Photonics Technol. Lett.* **12**, 317–319 (2000).
 39. H. Deng, D. O. Yevick, C. Brooks, and P. E. Jessop, "Design rules for slanted-angle polarization rotators," *J. Light. Technol.* **23**, 432–445 (2005).
 40. D. C. Hutchings and B. M. Holmes, "A waveguide polarization toolset design based on mode beating," *IEEE Photonics J.* **3**, 450–461 (2011).
 41. Z. Wang and D. Dai, "Ultrasmall Si-nanowire-based polarization rotator," *JOSA B* **25**, 747–753 (2008).
 42. K. Ando, T. Okoshi, and N. Koshizuka, "Waveguide magneto-optic isolator fabricated by laser annealing," *Appl. Phys. Lett.* **53**, 4–6 (1988).
 43. H. Shimizu and Y. Nakano, "Fabrication and Characterization of an InGaAsp / InP Active Waveguide Optical Isolator With 14 . 7 dB / mm TE Mode Nonreciprocal Attenuation," *J. Light. Technol.* **24**, 38–43 (2006).
 44. W. Van Parys, B. Moeyersoon, D. Van Thourhout, R. Baets, M. Vanwolleghem, B. Dagens, J. Decobert, O. Le Guezigou, D. Make, R. Vanheertum, and L. Lagae, "Transverse magnetic mode nonreciprocal propagation in an amplifying AlGaInAs/InP optical waveguide isolator," *Appl. Phys. Lett.* **88**, 2004–2007 (2006).
 45. H. Shimizu and Y. Nakano, "Monolithic Integration of a Waveguide Optical Isolator With a Distributed Feedback Laser Diode in the 1.5-um Wavelength Range," *Technology* **19**, 1973–1975 (2007).
 46. F. Auracher and H. H. Witte, "A new design for an integrated optical isolator," *Opt. Commun.* **13**, 435–438 (1975).
 47. W. Zaets and K. Ando, "Optical waveguide isolator based on nonreciprocal loss/gain of amplifier covered by ferromagnetic layer," *IEEE Photonics Technol. Lett.* **11**, 1012–1014 (1999).
 48. P. Pintus, F. Di Pasquale, and J. E. Bowers, "Integrated TE and TM optical circulators on ultra-low-loss silicon nitride platform," *Opt. Express* **21**, 5041 (2013).

49. G. J. G. and M. E. Brodwin, G. J. Gabriel, and M. E. Brodwin, "The Solution of Guided Waves in Inhomogeneous Anisotropic Media by Perturbation and Variational Methods," *IEEE Trans. Microw. Theory Tech.* **13**, 364–370 (1965).
50. E. Ishida, K. Miura, Y. Shoji, H. Yokoi, T. Mizumoto, N. Nishiyama, and S. Arai, "Amorphous-Si waveguide on a garnet magneto-optical isolator with a TE mode nonreciprocal phase shift," *Opt. Express* **25**, 452–462 (2017).
51. O. Zhuromskyy, M. Lohmeyer, N. Bahlmann, H. Dötsch, P. Hertel, and A. F. Popkov, "Analysis of polarization independent Mach-Zehnder-type integrated optical isolator," *J. Light. Technol.* **17**, 1200–1205 (1999).
52. J. Fujita, S. Member, M. Levy, R. M. Osgood, L. Wilkens, and H. Dötsch, "Polarization-independent waveguide optical isolator based on nonreciprocal phase shift," *IEEE Photonics Technol. Lett.* **12**, 1510–1512 (2000).
53. P. Pintus, "Accurate vectorial finite element mode solver for magneto-optic and anisotropic waveguides," *Opt. Express* **22**, 15737 (2014).
54. N. Bahlmann, M. Lohmeyer, O. Zhuromskyy, H. Dötsch, P. Hertel, H. Dötsch, and P. Hertel, "Nonreciprocal coupled waveguides for integrated optical isolators and circulators for TM modes," *Opt. Commun.* **161**, 330–337 (1999).
55. O. Zhuromskyy, M. Lohmeyer, N. Bahlmann, P. Hertel, H. Dötsch, A. F. Popkov, and H. Do, "Analysis of nonreciprocal light propagation in multimode imaging devices," *Opt. Quantum Electron.* **32**, 885–897 (2000).
56. R. Y. Y. Amaguchi, Y. U. Y. A. S. Hoji, and T. E. M. Izumoto, "Low-loss waveguide optical isolator with tapered mode converter and magneto-optical phase shifter for TE mode input," *2018 Opt. Fiber Commun. Conf. Expo.* **26**, 21271–21278 (2018).
57. R. R. Abbott, V. J. Fratello, S. J. Licht, and I. Mnushkina, "Article comprising a Faraday rotator that does not require a bias magnet," (2004).
58. D. Karki, V. Stenger, A. Pollick, and M. Levy, "Thin-film magnetless Faraday rotators for compact heterogeneous integrated optical isolators," *J. Appl. Phys.* **121**, (2017).
59. M.-C. Tien, T. Mizumoto, P. Pintus, H. Kromer, and J. E. Bowers, "Silicon ring isolators with bonded nonreciprocal magneto-optic garnets," *Opt. Express* **19**, 11740 (2011).
60. P. Pintus, D. Huang, C. Zhang, Y. Shoji, T. Mizumoto, and J. E. Bowers, "Microring-Based Optical Isolator and Circulator with Integrated Electromagnet for Silicon Photonics," *J. Light. Technol.* **35**, 1429–1437 (2017).

61. J. R. Black, "Electromigration—A brief survey and some recent results," *Electron Devices, IEEE Trans.* **16**, 338–347 (1969).
62. S. Ghosh, S. Keyvavinia, W. Van Roy, T. Mizumoto, G. Roelkens, W. Van Roy, T. Mizumoto, G. Roelkens, and R. Baets, "Ce:YIG/Silicon-on-Insulator waveguide optical isolator realized by adhesive bonding," *Opt. Express* **20**, 1839 (2012).
63. M. Levy, R. M. Osgood, H. Hegde, F. J. Cadieu, R. Wolfe, and V. J. Fratello, "Integrated optical isolators with sputter-deposited thin-film magnets," *IEEE Photonics Technol. Lett.* **8**, 903–905 (1996).
64. K. Okazeri, K. Muraoka, Y. Shoji, S. Nakagawa, N. Nishiyama, S. Arai, and T. Mizumoto, "Self-Holding Magneto-Optical Switch Integrated with Thin-Film Magnet," *IEEE Photonics Technol. Lett.* **30**, 371–374 (2018).

Chapter 3

Microring based nonreciprocal devices

The microring resonator has been arguably the most studied device in integrated photonics over the last decade. The term “microring” is used loosely to include all sorts of waveguide based integrated resonators with varying radii and shape. Silicon photonics has been an ideal platform for ring resonators, as the high index contrast between the silicon core and surrounding silicon dioxide cladding allow for tight confinement of the optical mode and very small bend radii. An overview of silicon based microrings can be found in [1], and some basic concepts will be presented in Section 3.1. The following sections will then introduce nonreciprocal materials and properties into the microrings to realize resonant optical isolators and circulators [2].

3.1 Microring resonator

Like any optical resonator, the microring has a resonant condition for which the light adds up constructively upon making a round-trip. The resonant condition is satisfied when the accumulated phase of light in the resonator (βL) is an integer multiple of 2π . Typically, it is more convenient to express this resonant condition in terms of the wavelength, as given in Equation 3.1), where m is an integer and L is the physical round

trip length in the cavity. The spacing between adjacent resonant wavelengths is known as the free spectral range (FSR) and given in Equation 3.2. Note that this equation assumes that the FSR is much smaller than the resonant wavelength.

$$\lambda_m = \frac{n_{eff} \cdot L}{m} \quad (3.1)$$

$$FSR = \frac{\lambda^2}{L \cdot n_g} \quad (3.2)$$

Typically, the ring resonator is accessed through the placement of one or more “bus” waveguides that provide evanescent coupling in and out of the resonator. An “all-pass” configuration is shown in Figure 3.1 for which a single waveguide is in proximity to the ring with radius R and circumference L . The single-pass coupling to the ring is denoted as κ while the single-pass transmission along the bus waveguide is t . In most scenarios, lossless coupling is assumed such that $\kappa^2 + t^2 = 1$. Propagation loss in the ring itself is considered, with a power attenuation constant α . The fields E_{in} and E_{out} represent the input and output of the resonator, while E_{r1} and E_{r2} are the fields inside the resonator immediately prior and after the coupling region.

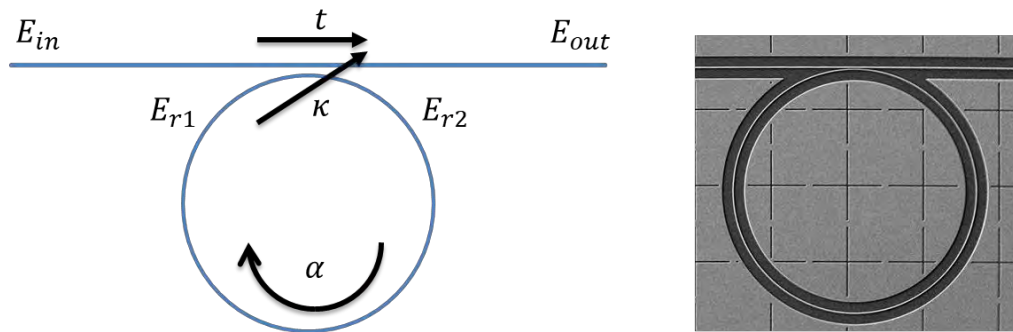


Figure 3.1: Schematic and SEM image of an all-pass ring resonator

The transfer function can be easily derived via a series of relations as shown in the following equations.

$$E_{out} = tE_{in} + \kappa E_{r1} \quad (3.3)$$

$$E_{r2} = \kappa^* E_{in} + t^* E_{r1} \quad (3.4)$$

$$E_{r1} = e^{(j\beta - \alpha/2)L} \cdot E_{r2} \quad (3.5)$$

Substitution of the equations shown above and squaring the field intensities results in a well-known power transfer function for the all-pass ring resonator [3].

$$\frac{|E_{out}|^2}{|E_{in}|^2} = \frac{t^2 + e^{-\alpha L} - 2te^{-\alpha L/2}\cos(\beta L)}{1 + t^2e^{-\alpha L} - 2te^{-\alpha L/2}\cos(\beta L)} \quad (3.6)$$

When the wavelength is off-resonance such that $\beta L \neq 2m\pi$, and under the assumption that α is small such that $e^{-\alpha L} \sim 1$, Equation 3.6 implies that $|E_{out}|$ and $|E_{in}|$ are equal in magnitude, hence the term “all-pass”. On the other hand, when the resonant condition $\beta L = 2m\pi$ is satisfied, the magnitude of the transfer function depends on the strength of the coupling as well as the loss in the resonator. When the power lost per round trip is equal to the single pass coupled power into the ring, mathematically $|\kappa|^2 = (1 - e^{-\alpha L})$ or alternatively $|t|^2 = e^{-\alpha L}$, Equation 3.6 becomes equal to zero. This is known as the critical coupling regime of the ring. Under this condition, all the resonant light is eventually dissipated in the ring, and none of it reaches the output. The extinction ratio of the resonator is defined as the ratio between the off-resonance transmission

($\beta L = 2m\pi + \pi$) and on-resonance transmission ($\beta L = 2m\pi$). The equation for the extinction ratio (ER) of an all-pass ring is given in Equation 3.7.

$$ER = \frac{(t + e^{-\alpha L/2})^2}{(1 + te^{-\alpha L/2})^2} \bigg/ \frac{(t - e^{-\alpha L/2})^2}{(1 - te^{-\alpha L/2})^2} \quad (3.7)$$

Realistically, the extinction ratio is never infinite, even if the critical coupling condition is satisfied. This can be due to a variety of reasons such as polarization conversion in bent waveguides [4], interference with other Fabry-Perot modes, backscattering in the ring waveguide [5] or coupler [6], or losses in the coupling region [7], for example to higher order modes [8]. The extinction ratio may also be limited due to measurement capabilities, such as the limited polarization extinction ratio of lensed fibers.

The other commonly used ring resonator device is known as an “add-drop” configuration, in which the ring is connected to two bus waveguides. This creates a device with four ports, as shown in Figure 3.2. Traditionally, if light is input from port 1, then port 3 is known as the drop port, while port 2 is the thru port. Port 4 is referred to as the add port, and only interacts with the light from port 1 through backscattering in the ring or couplers, which is assumed to be negligible for simplicity.

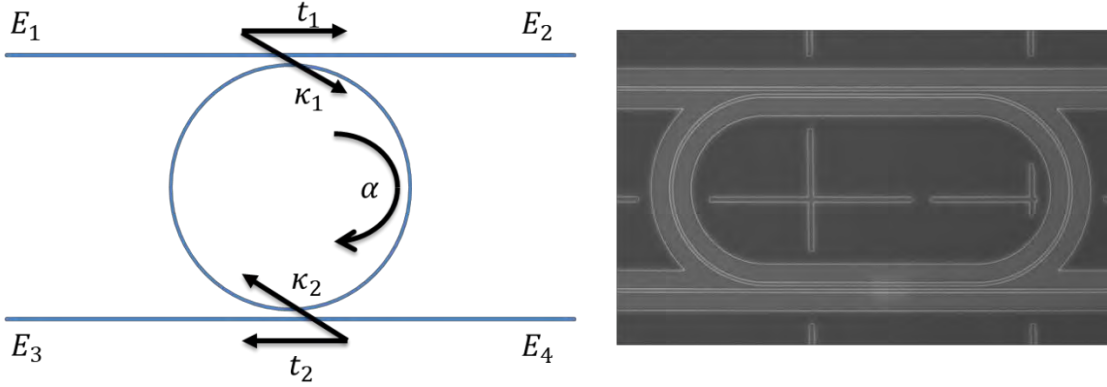


Figure 3.2: Schematic and SEM image of an add-drop ring resonator

The transfer functions for the add-drop ring configuration are shown below [1].

$$\frac{|E_2|^2}{|E_1|^2} = \frac{t_1^2 + t_2^2 e^{-\alpha L} - 2t_1 t_2 e^{-\alpha L/2} \cos(\beta L)}{1 + t_1^2 t_2^2 e^{-\alpha L} - 2t_1 t_2 e^{-\alpha L/2} \cos(\beta L)} \quad (3.8)$$

$$\frac{|E_3|^2}{|E_1|^2} = \frac{(1 - t_1^2)(1 - t_2^2)e^{-\alpha L/2}}{1 + t_1^2 t_2^2 e^{-\alpha L} - 2t_1 t_2 e^{-\alpha L/2} \cos(\beta L)} \quad (3.9)$$

The ER for the thru port, as defined as the ratio between off-resonance and on-resonance transmission is given in Equation 3.10. The ER for the drop port, as defined as the ratio between on-resonance to off-resonance transmission (flipped as to keep positive ER) is given in Equation 3.11.

$$ER_{thru} = \frac{(t_1 + t_2 e^{-\alpha L/2})^2}{(1 + t_1 t_2 e^{-\alpha L/2})^2} \bigg/ \frac{(t_1 - t_2 e^{-\alpha L/2})^2}{(1 - t_1 t_2 e^{-\alpha L/2})^2} \quad (3.10)$$

$$ER_{drop} = \frac{(1 - t_1^2)(1 - t_2^2)e^{-\alpha L/2}}{(1 - t_1 t_2 e^{-\alpha L/2})^2} \bigg/ \frac{(1 - t_1^2)(1 - t_2^2)e^{-\alpha L/2}}{(1 + t_1 t_2 e^{-\alpha L/2})^2} \quad (3.11)$$

From Equation 3.10, the critical coupling condition occurs when $|t_1|^2 = |t_2|^2 e^{-\alpha L}$. However, symmetric coupling is used more often in practice, such that $t_1 = t_2$. This is especially true when any of the ports can be used as an input port. When engineering the response of an add-drop filter, most of the design choices lie in the engineering of the coupling to the ring. This is because the loss in the ring is often a combination of waveguide design as well as fabrication prowess, which may be outside of the researcher's control. Furthermore, the critical coupling condition is often hard to hit, and most resonators in practice are undercoupled or overcoupled depending on the application.

The final relevant parameter of the microring as it pertains to this work is the quality factor (Q) of the resonator. The Q-factor is the ratio of stored energy in the resonator to the power loss per round trip in the resonator. It is also a comparison of the sharpness of the resonator relative to the resonance frequency, given by the resonance wavelength of the resonator divided by the full-width half maximum (FWHM) of the resonance spectrum. The Q-factors for an all-pass and add-drop ring resonator are given in Equations 3.12 and 3.13 respectively [1].

$$Q_{all-pass} = \frac{\pi n_g L \sqrt{t e^{-\alpha L/2}}}{\lambda (1 - t e^{-\alpha L/2})} \quad (3.12)$$

$$Q_{add-drop} = \frac{\pi n_g L \sqrt{t_1 t_2} e^{-\alpha L/2}}{\lambda(1 - t_1 t_2 e^{-\alpha L/2})} \quad (3.13)$$

The Q-factors here are otherwise referred to as the loaded-Q of the resonator. They take both the intrinsic losses in the resonator as well as the coupling into the resonator into account. Often, the intrinsic-Q of the resonator, or the Q-factor in absence of coupling into the resonator, is quoted, since it is a direct measurement of the propagation losses in the resonator. The loaded quality is related to the intrinsic quality factor by Equation 3.14 where the energy losses due to the coupler are also taken into account.

$$\frac{1}{Q_{load}} = \frac{1}{Q_{int}} + \frac{1}{Q_{coupling}} \quad (3.14)$$

In practice, the loaded Q-factor can be immediately calculated from the spectral response of the ring resonator, and the intrinsic Q-factor can be estimated by analyzing the extinction ratio of the resonance. This equivalence is given in Equation 3.15 for an all-pass resonator, where the \pm refers to the under and over-coupled regimes respectively, and $T(\lambda_{res})$ is the transfer function (Equation 3.6) evaluated at resonance [9]. Finally, the propagation loss in the resonator can be calculated based on Equation 3.16 [10].

$$Q_{load} = \frac{2Q_{int}}{1 \pm \sqrt{T(\lambda_{res})}} \quad (3.15)$$

$$\alpha = \frac{\lambda_{res}}{Q_{int} \cdot R \cdot FSR} \quad (3.16)$$

Thus, it is clear from Equation 3.15 that the loaded Q is half of the intrinsic Q at critical coupling for an all-pass ring resonator. Furthermore, the inverse relationship between loss and Q-factor in Equation 3.16 is apparent and can be used to estimate waveguide loss from a ring resonator test structure. This is generally more accurate than cutback methods and consumes significantly less footprint than long waveguide spiral test structures. However, it should be noted that bend loss and coupler induced loss are indistinguishable in Equation 3.16, and the calculated loss values are an overestimate of propagation loss.

3.2 Microring optical isolator

Design

The use of resonant devices to enhance nonreciprocal effects such as magneto-optic effects has been proposed for over a decade. Photonic crystal based waveguides were theoretically studied and proposed to enhance NRPS effects while miniaturizing the devices [11,12]. The use of a microresonator to perform optical isolation and circulation was first proposed in 2007 [13], with additional theoretical work being carried out in the following years [14]. However, it was not until 2011 that the concept was demonstrated through the combination of silicon microrings with magneto-optic garnet [15,16]. Since then, continuous improvements have been made to increase isolation, decrease footprint, and provide fabrication compatibility with other silicon

photonic devices. These improvements have led to the microring isolators discussed in this section [17–20].

The microring optical isolator in this work consists of an all-pass microring-based filter that is coupled to a straight waveguide, as schematically shown in Figure 3.3. Both the microring and the bus waveguide are made of silicon ($n_{\text{Si}}=3.44$) with a bonded Ce:YIG layer ($n_{\text{Ce:YIG}}=2.22$), which was previously grown on a substituted gadolinium gallium garnet ($n_{\text{SGGG}}=1.97$) substrate. The waveguide is covered with a sputtered silicon dioxide cladding ($n_{\text{SiO}_2}=1.44$) outside of bonded areas. A radially orientated magnetic field can be applied to the ring using an electromagnet that is deposited on the backside of the bonded garnet, as discussed in Section 2.5. In the initial demonstration of this device, only a single coil was used for the electromagnet.

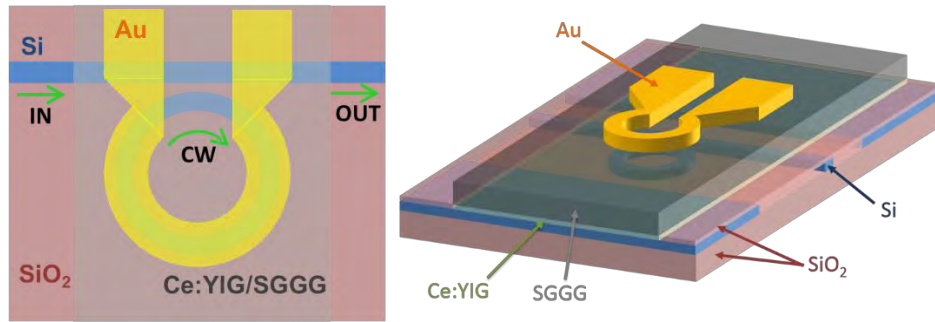


Figure 3.3: Schematic of the microring isolator

In this device, forward propagating light is defined as input from the left side, coupling light into the clockwise mode in the resonator. Backward propagating light is defined as input from the right side, coupling light into the counterclockwise mode. In the absence of any radial magnetic field, the device behaves as any other reciprocal ring resonator, exhibiting the same transfer function for forward and backward propagating

light. Spectrally, the device has the same resonant condition for both clockwise (λ_{CW}) and counterclockwise (λ_{CCW}) modes, resulting in the same resonant wavelength.

$$\lambda_{CW}(H_r = 0) = \lambda_{CCW}(H_r = 0) \quad (3.17)$$

When current is applied to the electromagnet and a radially orientated magnetic field is applied to the ring, the Ce:YIG begins to magnetize in a direction that is perpendicular to the direction of light propagation. This is identical to the Voigt configuration as shown in Figure 3.4, which produces an effective index difference (Δn_{eff}) and NRPS ($\Delta\beta$) between the CW and CCW modes for TM polarized light. This leads to a different resonant condition for CW and CCW modes, and a resonant wavelength split ($\Delta\lambda_{MO}$) between forward and backwards propagating light arises, as given in Equation 3.18. Thus, optical isolation is achieved when the resonance of the backwards (CCW) mode is aligned to the operating wavelength, as depicted in Figure 3.5. The amount of optical isolation is dependent on the extinction ratio of the ring, which is maximized in the critical coupling regime.

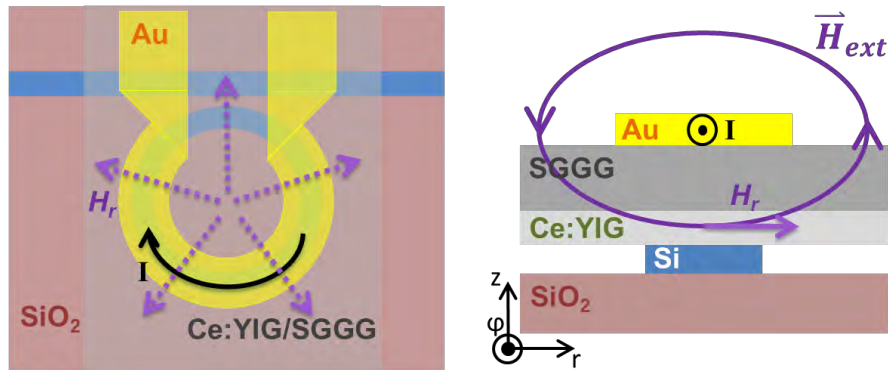


Figure 3.4: Schematic of the integrated electromagnet on top of the microring isolator

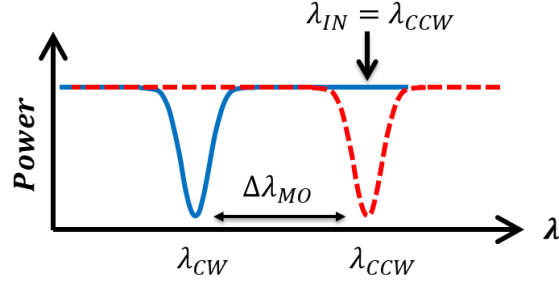


Figure 3.5: Depiction of the resonant wavelength split caused by NRPS

$$\Delta\lambda_{MO} = \frac{\Delta n_{eff}}{n_g} \lambda \quad (3.18)$$

The design of the isolator begins with optimization of the waveguide cross-section in order to provide the strongest NRPS effect. Using the methodology discussed in Section 2.4, the NRPS and resonant wavelength split (RWS) is calculated for a range of silicon waveguide and Ce:YIG cladding dimensions. The results are plotted in Figure 3.6, for TM polarized light at a wavelength of 1550nm and assuming a saturation Faraday rotation of -4500 degrees/cm for the Ce:YIG. A width of 600nm for the silicon waveguide was simulated, which was chosen for the waveguide to only support a single TM mode in both the Ce:YIG clad as well as SiO₂ clad regions. Simulations for different widths near 600nm show similar results, which is expected given the TM polarization of light.

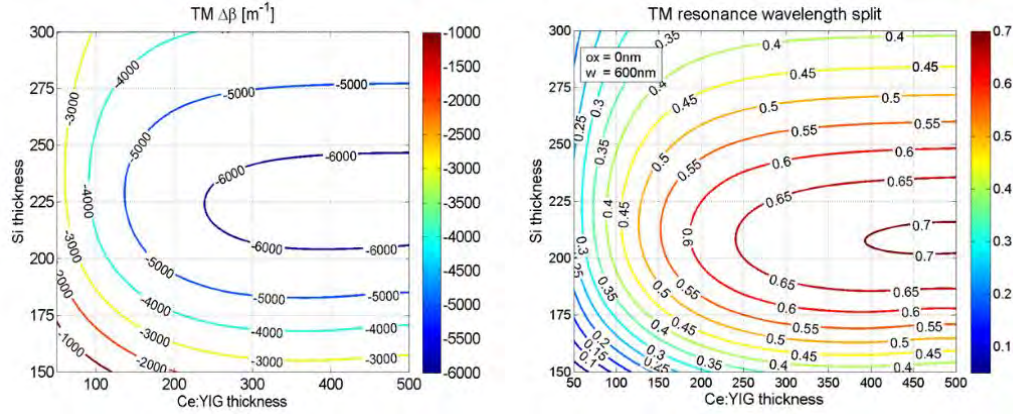


Figure 3.6: Simulated results for NRPS and resulting RWS as a function of silicon and Ce:YIG thicknesses.

The final waveguide cross-section is selected to be a 220nm thick by 600nm wide silicon waveguide, with a 400nm thick Ce:YIG top cladding. This is near the optimal value in the contour plots in Figure 3.6, and easily realizable given the SOI and Ce:YIG wafers present at the time. An important detail that needs to be taken into account is the presence of a thin oxide layer between the silicon and Ce:YIG that is usually present due to the plasma assisted O_2 wafer bonding process [21]. The thickness in this work is assumed to be 10nm, although AFM measurements later revealed this thickness to be as thin as 5nm. Factors such as the presence of native oxide, the oxide activation parameters, and the cleaning procedures of the materials prior to the bonding are likely to change this thickness. The thickness of this oxide layer is critical to the amount of NRPS, since the mode is centered on the Si/Ce:YIG boundary. Thicker oxide layers severely degrade the NRPS and RWS, as shown in Figure 3.7. Even a 10nm oxide layer decreases the maximum RWS by roughly 20% to a value of 0.55nm. This problem is enhanced in devices in which adhesive polymer (BCB) is used in place of the oxide [22]. A 60nm thick BCB layer, which is typical, will reduce the NRPS by over 3 times. The oxide

thickness variation is also by far the least tolerant to variation, although in practice, thickness variation is much less common than width variation during fabrication.

Fabrication tolerance of the RWS to various parameters is shown in Figure 3.7.

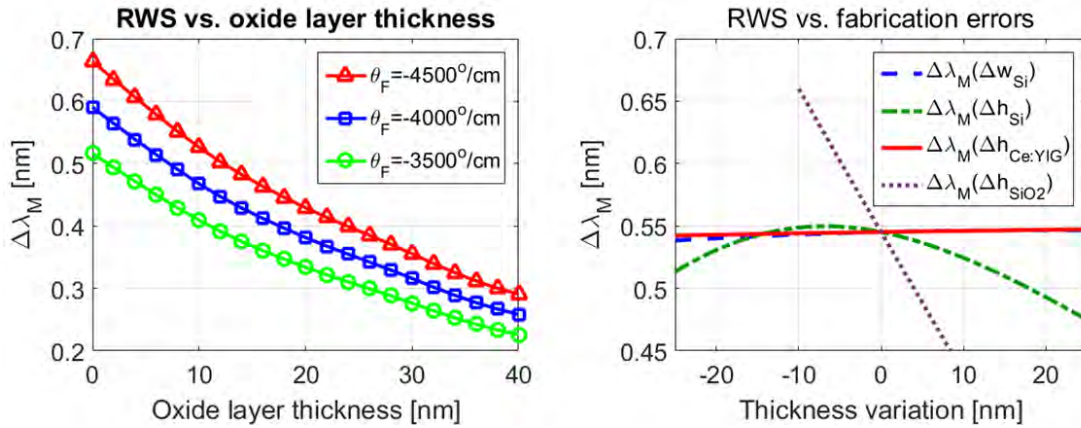


Figure 3.7: Simulations of the sensitivity of RWS with respect to thickness variation in the layers of the MO waveguide.

Once the waveguide cross-section is established, the next step is to simulate the bent waveguide that will be in the ring resonator. The key parameters are the bend radius and coupling gap between the ring and bus waveguide. The dependence of bend loss on radius is simulated with Lumerical MODE and plotted in Figure 3.8 for several waveguide parameters such as silicon thickness and width, as well as bonding oxide thickness. Intuitively, stronger confinement in waveguides results in smaller bend radii, which is apparent from higher bend loss from TM modes compared to TE modes. The Ce:YIG thickness is assumed to be 400nm. In all simulations, rings with larger than 25 micron radius should be free from bend loss.

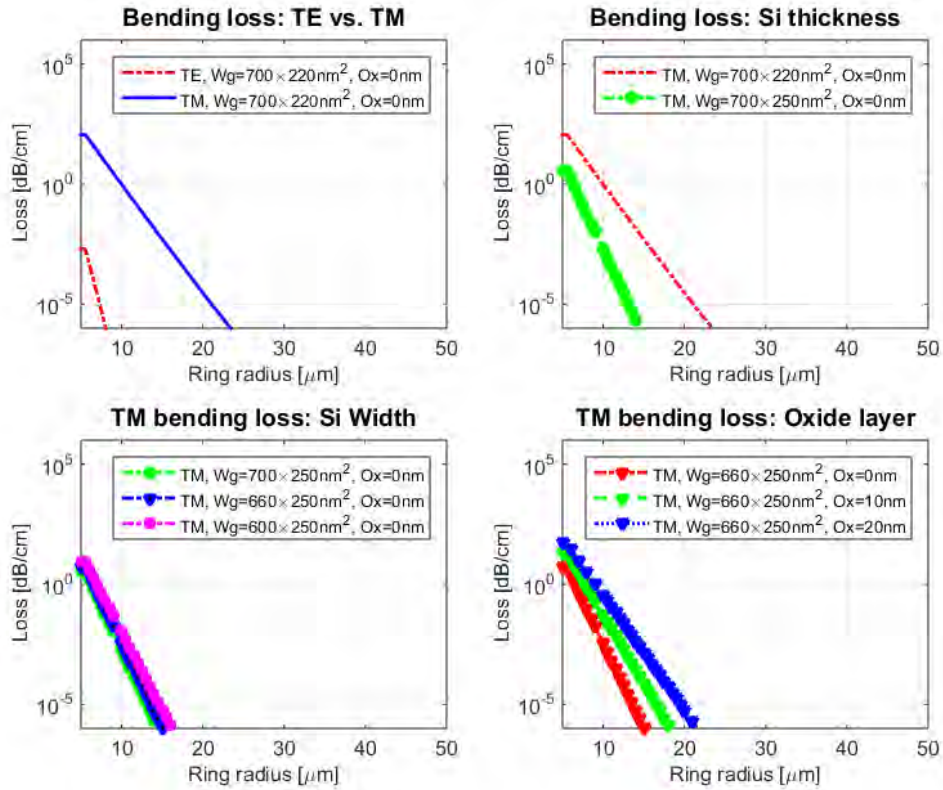


Figure 3.8: Simulations of the bend loss for a variety of MO waveguide geometries with different widths and thicknesses.

The last design parameter is the coupling coefficient κ into the ring resonator from the bus waveguide. For a straight-to-curved coupler used in this work, this is a strong function of ring radius as well as coupling gap. Generally, the radius of the ring is fixed, and the coupling gap is varied, as shown in Figure 3.9 for a 35 micron radius ring. The simulation was performed with Lumerical FDTD software, where only the coupling region was simulated. The power coupling ratio κ^2 is shown as a function of wavelength and coupling gap.

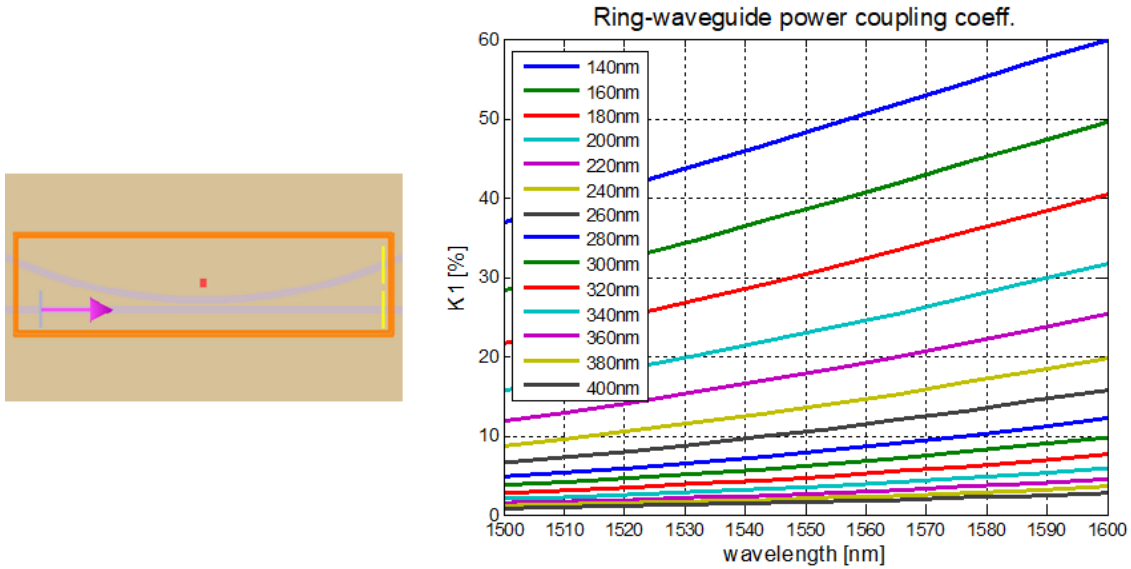


Figure 3.9: Simulations of the coupling into the MO ring for different gaps ranging from 140nm to 400nm for a ring radius of 35 microns.

As previously mentioned, the key to obtaining large optical isolation is to achieve near critical coupling to the resonator. As a result, the propagation loss in the ring should be estimated. For the first generation of devices, the propagation loss in the resonator was estimated in the 20-30dB/cm range based on literature values of 40-60dB/cm loss in Ce:YIG and roughly 45% confinement in the Ce:YIG [23]. Given the simulations in Figure 3.9, the coupling gap was determined to be between 220 to 260nm, which gives roughly 10 to 15% power coupling into the ring. Splits were laid out on mask centered around the simulated values.

Fabrication

Fabrication of the devices begins with preparing an SOI wafer of the appropriate thickness. The first generation of devices used an 230nm thick silicon device layer on 1 micron buried oxide (BOX), which was achieved by thinning down a 500nm thick silicon device layer SOI wafer via thermal oxidation and buffered HF etching. The oxidation was performed in a dry (no water vapor) oxidation furnace at a temperature of 1050C for 24 hours. The exact oxidation time needs to be fine-tuned, but was generally within 10% of the values given by oxide growth calculators [24]. Subsequent fabrication runs used a “standard” 220nm silicon device layer on a 2 micron BOX, which was popularized by imec. Simulations showed that there is not a significant difference caused by the 10nm height difference. The difference in BOX thickness does not affect optical device performance, but can be a limiting factor in thermal dissipation, as it inhibits heat from flowing from the device layer to the silicon substrate.

The fabrication procedure is depicted in Figure 3.10. The SOI wafer is patterned using an ASML 5500 deep-UV stepper using a positive UV210-0.3 photoresist and AR2 DUV antireflectant. Through optimization of the lithography dose and focus, gaps and lines as small as 200nm can be repeatedly achieved. However, the optimal conditions to achieve the smallest dimensions are often different for lines and gaps. Therefore, mask bias may be needed if both line and gap dimensions are critically small. The silicon waveguides as well as vertical channels (for outgassing) are etched in a single step using a $C_4F_8/SF_6/Ar$ etch chemistry in a ICP etcher (Si Deep RIE/Flourine ICP). The exact etch parameters varied over different fabrication runs, partially due to the tool being refitted and upgraded. An Intellemetrics LEP500 etch rate monitor was later installed on the tool

to allow for real-time laser etch monitoring. While all the waveguides in this work were etched fully to the BOX, the etch rate monitor ensured that the etch depth would be successful, regardless of the etch rate, which is extremely temperature sensitive in the tool. Etch optimization was performed multiple times over this work, as etch conditions in the tool drift over time. Verticality of the waveguides and smooth sidewalls were achieved, as shown in the waveguide SEMs in Figure 3.11.

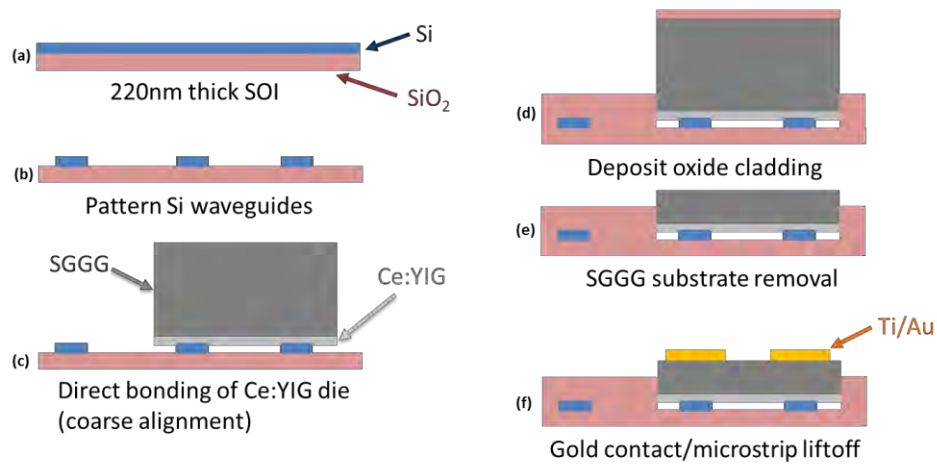


Figure 3.10: Fabrication flow for integrated optical isolators and circulators

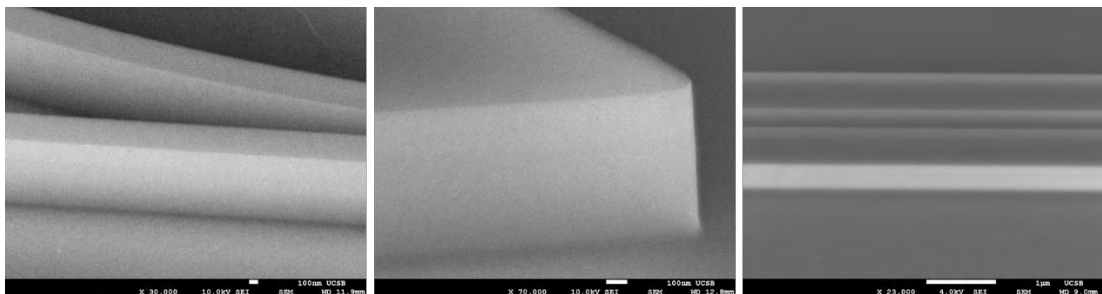


Figure 3.11: SEM images of the silicon waveguides used in the microring isolator prior to Ce:YIG bonding.

After the waveguides are etched and cleaned, both the SOI wafer and Ce:YIG dies are prepared for bonding. The Ce:YIG on SGGG is provided courtesy of Professor Tetsuya

Mizumoto and Professor Yuya Shoji of Tokyo Institute of Technology. It is a 2" wafer measuring roughly 300 microns in thickness. Due to the difficulties in cleaving garnet substrates, the individual dies are diced out. Typically, the dies are 5 to 10mm in length, and 1-2mm in width, and require special care in handling, especially during cleaning. The Ce:YIG appears yellowish in color, while the SGGG substrate is completely transparent. It is near impossible to tell which side is "up" once the dies have been diced and there is no reference flat. During the cleaning procedure of garnet with acetone and isopropanol, it is common to lose track of the correct orientation of the garnet. Tricks to keep track of the correct side for bonding include scribing a mark on the backside prior to dicing, as well as analyzing the edges of the die for chipping, which is much less significant on the side with the thin-film Ce:YIG. Other researchers have prepared the Ce:YIG samples with a bevel shape [25]. After cleaning of the samples, an EVG810 tool is used to activate the surface of the two materials with an oxygen plasma. This 30 second activation is nearly identical to the procedure used for bonding III-V materials to silicon [26]. Finally, the activated surfaces of the two are brought into contact, forming a spontaneous bond. Since rough alignment is necessary between the Ce:YIG dies and the silicon wafer, a Finetech flip-chip bonder is used. Multiple dies can be bonded at once, which is usually the case for the devices in this work. Figure 3.12 shows the Ce:YIG in various stages of preparation from a full wafer [27] to diced out pieces to spontaneously bonded dies on a silicon wafer.

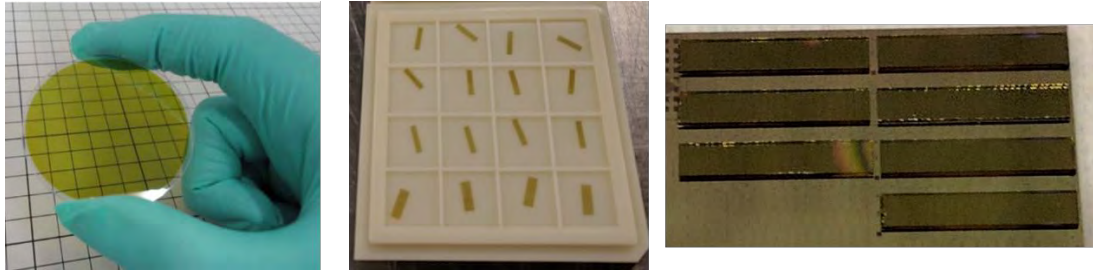


Figure 3.12: Images of Ce:YIG/SGGG 2'' wafer and individual dies (bonded on Si)

The transparent nature of the garnet allows for some interesting post-bond observations, since the silicon waveguides underneath the Ce:YIG/SGGG is immediately visible following bonding. The bond yield can be determined at this point, prior to any substrate removal processes. This is often not the case with III-V bonding, in which the final bond yield is not known until the substrate removal is complete. Rainbow patterns and fringes are often visible following the initial bond, which is indicative of delamination. Nine times out of ten, this delamination is caused by vertically protruding particulates either on the silicon or Ce:YIG. Depending on the size and height of the particle, the delamination may be local, or protrude out to the edge of the die. Some microscope images are shown in Figure 3.13 that show the waveguides under the bonded Ce:YIG, as well as some bond fail areas stemming from particles. A small particle causes only a local delamination, while a larger particle can cause an entire corner to delaminate.

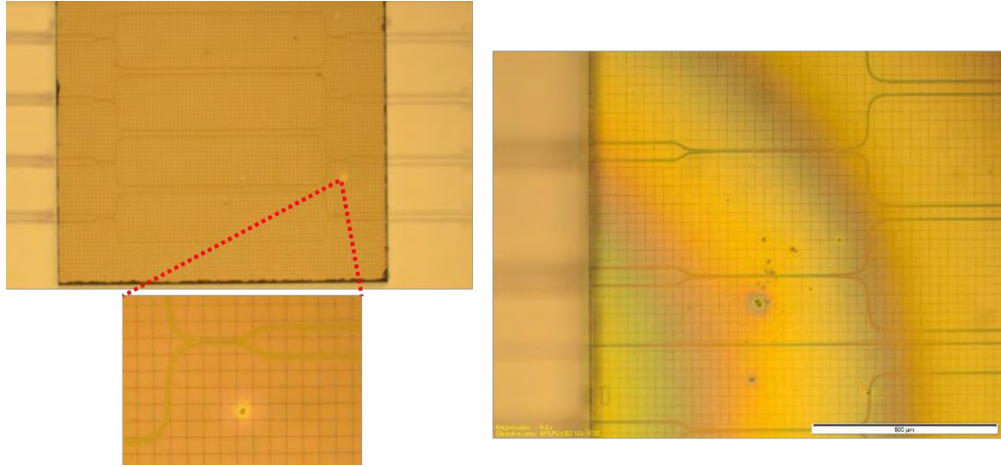


Figure 3.13: Micrographs of various Ce:YIG/Si bond fails stemming from particulates of varying sizes

Another observation is that sometimes, the surfaces will only be in intimate contact in the immediate area where the force was applied during the spontaneous bond (where the vacuum was applied by the flip chip bonder to pick up the piece). Other areas are often not in direct contact, possibly due to bowing of the wafer or the die. Upon applying slight pressure on the back of the bonded die, the dark, well-bonded areas will spread, as the materials have some degree of flexibility, until hopefully the entire die is firmly bonded, as shown in Figure 3.14. Next, the bond is further strengthened by clamping the pieces between a graphite fixture and annealing the parts at 200C for 6 hours. It is very much possible that 6 hours is not needed, but the necessary experiments were not carried out. Experiments were carried out at 250C and 300C, but anneals at those higher temperatures often led to cracked samples, stemming from the large CTE mismatch between silicon and Ce:YIG. In the fixture, a flexible graphite sheet is placed directly on top of the chip in order to prevent shear during the anneal. However, it was found that this graphite sometimes left residue on the chip, and an additional aluminum foil was

used in between the chip and graphite sheet to prevent any residue from sticking to the waveguides. Figure 3.15 shows SEM images of the edge of the bonded Ce:YIG die on silicon. The dicing leaves a slightly jagged edge, which sometimes is not in intimate contact with the silicon. This is consistent with observations made during III-V bonding to silicon, in which the edges of the die are common bond fail areas.

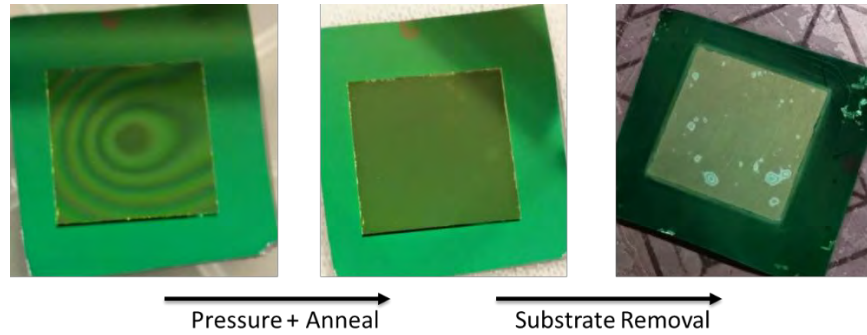


Figure 3.14: Progression of Ce:YIG on silicon after bonding, anneal, and substrate removal respectively.

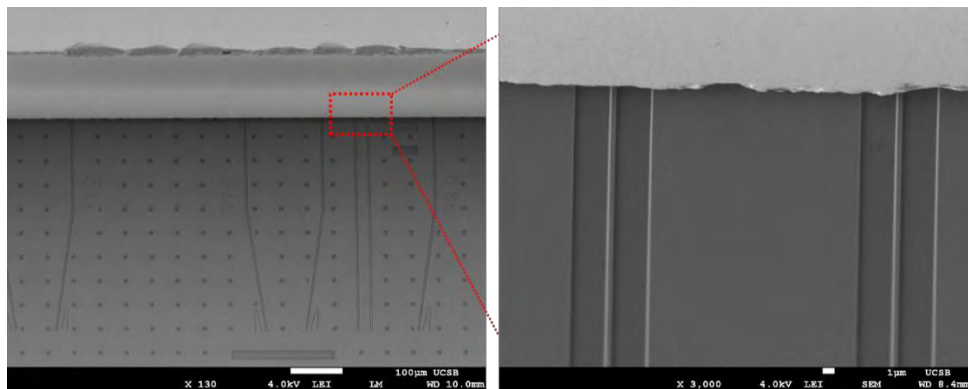


Figure 3.15: SEM images of the waveguides entering the bonded Ce:YIG regions, from which some chipping can be observed.

Arguably the most crucial step in the process is the substrate removal following the bond and anneal. As mentioned in Chapter 2, the substrate of the bonded garnet must be thinned to <10 microns to have efficient magnetic field generation from the

electromagnet. This substrate removal is primarily done with a purely mechanical grinding process (Allied MultiPrep). The standard III-V substrate removal process usually stops when the bonded layer is around 100 microns tall, before a wet etch is used to complete the process. An etch stop (InGaAs) layer in the III-V epi is the enabler in this process, as it has 1000:1 selectivity with the HCl etch used to etch InP. Unfortunately, we are not aware of any similar etch stops that can be included in the SGGG/Ce:YIG stack. For all the devices in this work, the grinding process was used all the way to thin the substrate from 300 microns to less than 10 microns. This is done through a combination of precise leveling (chip to chuck, chuck to polishing arm) as well as using a series of progressively finer polishing films. Leveling is crucial, as the waveguides would be damaged and scratched if exposed to the polishing film. After some practice, it is possible to repeatedly thin down the Ce:YIG to under 10 microns thick. With some patience and careful levelling, the substrate can be thinned down to only 5 microns in this work without damage to the rest of the chip. The thickness variation across the die and chip depends on the levelling but is usually within 2 to 3 microns.

Further improvements can be made in the substrate removal process. With dynamic levelling of the wafer, substrate thickness as thin as 1 micron should be achievable. A chemical substrate removal process is advantageous for increased uniformity and repeatability but may be difficult to implement for garnets without a dedicated etch stop layer. An alternate method for substrate removal could be “smart cut” [28], in which a defect layer is planted in the garnet using heavy ion implantation, and then released using thermal or chemical treatment [29]. If this implantation is done prior to bonding, then a thin film of garnet could be transferred to silicon following wafer bonding and

subsequent release process. Thus, ion implantation should be deep enough to avoid roughening the surface prior to bonding, but not so deep as to increase the distance to the waveguide too much. The film release can also be done prior to bonding, but the handling of such a thin, brittle garnet film poses a challenge [30]. For monolithic processes where the garnet is deposited instead of bonded, the fabrication could be further simplified, as the distance between the waveguide and electromagnet can be precisely controlled during cladding deposition.

One issue with a purely mechanical substrate removal process is the residue from the grinding. The waveguides should be protected during the process, or the residue (mostly garnet) may attach themselves to the silicon and become extremely resistant to cleaning. This is shown in Figure 3.16, which led to a run with extremely high loss for the waveguides. Several methods were considered and experimented with to protect the waveguides including spinning a resist layer or melting a wax layer, as well as to clean the waveguides after substrate removal with wet chemistry. Each of these had some drawbacks. Putting on a resist or wax layer made it harder to level the chip precisely and exposes the chip to more temperature cycling due to the baking. The wet etching in sulfuric or phosphoric acid cleaned up the waveguides but came at the cost of undercutting the chips. Ultimately, the choice was made to deposit a 1-micron thick sputtered (low temperature) SiO₂ cladding prior to the substrate removal, as detailed in Figure 3.10. With this cladding in place, the residue is far enough away from the optical mode that it can be ignored. SEM images of the chip after substrate removal are shown in Figure 3.16. A focused ion beam (FIB) image of the cross section is also shown.

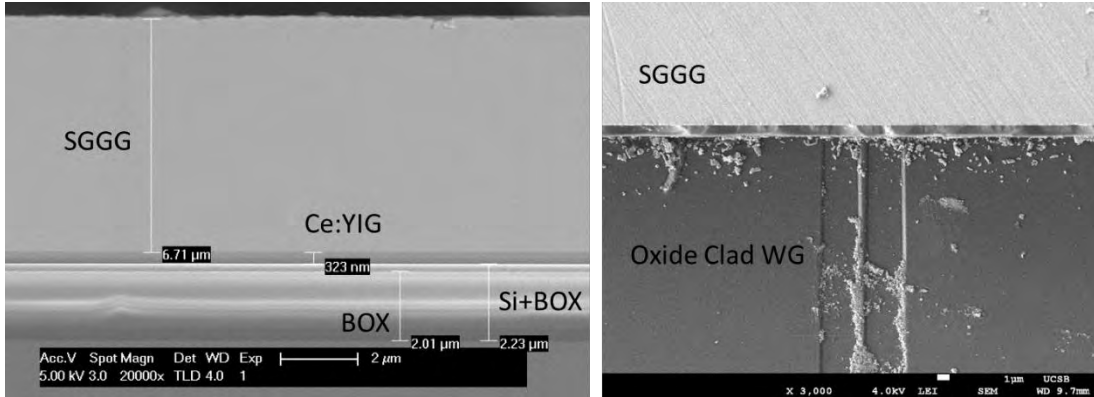


Figure 3.16: SEM images of the bonded cross-section, as well as the transition into the bonded areas after substrate removal is complete.

After the substrate removal is complete, the only remaining step is to deposit the electromagnet. This is done using a bi-layer PMGI/SPR resist combination to generate a controllable undercut of roughly 1 micron, followed by e-beam evaporation of titanium (~20nm) and gold (~1500nm). This allows for the metal lines to be spaced closely together, which is important when the electromagnet contains multiple coils, as was discussed in Section 2.5. However, only a single coil was used in the first demonstration of these devices. Images of the completed microring isolators are shown in Figure 3.17.

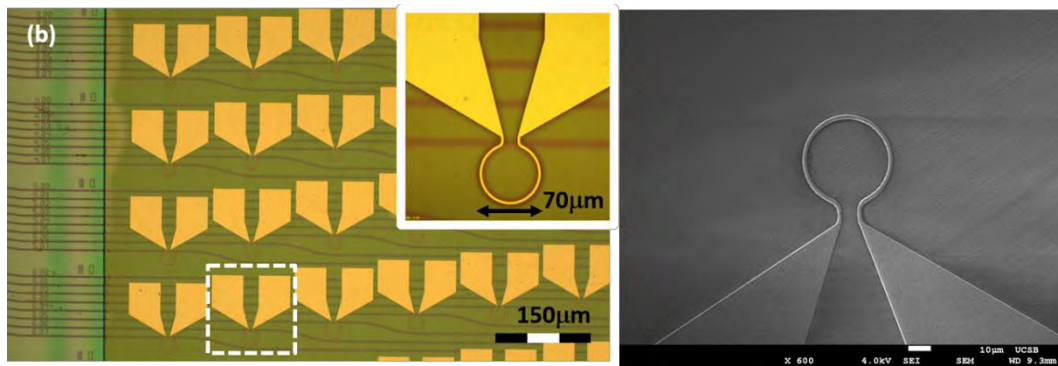


Figure 3.17: Micrograph and SEM image of an array of completed microring isolators.

Characterization

The optical characterization was carried out at room temperature (20°C) on a temperature-controlled stage. Two polarization maintaining (PM) lensed fiber with 2.5-micron spot size were securely clamped in a fiber rotator and rotated to a TM polarization. We measure a polarization extinction ratio of at least 26dB. The PM fibers are aligned to the edge couplers of the isolator, and the transmission spectra of the device is measured using a tunable laser (Keysight 8160) and synchronized power sensor. A 10pm step size was used when scanning a wide wavelength range (>40nm), while a much smaller 0.1pm step size was used when scanning across a single resonance of the ring.

The current was applied using a through beryllium copper probes and swept from 0 to 220mA. To test for isolation, we can either switch the input/output fibers (changing propagation direction) or switch the direction of the current (changing magnetic field direction). Mathematically, these are equivalent since it is the polarity of the magnetic field with respect to the propagation direction of light that causes the NRPS. Practically, there are some subtle differences between the two methods, since the forward and backwards transmission spectra are not taken simultaneously. When switching the input and output fibers, one must take care that both fibers are PM and aligned to the TM polarization with similar PER in order to preserve the same launch conditions. If the magnetic field is switched instead, one must make sure that all other factors in the measurement, especially temperature, stay constant. This is especially important for resonator devices, which are very sensitive to temperature. Over the course of this work, both testing methods were used multiple times and the results were consistent,

regardless of the method used. For the microring isolators, changing the direction of current does not significantly affect the temperature of the device, since the electromagnet is only a resistor and Joule heating is not affected by the direction of the current. Therefore, this is the methodology used for testing, as it is quicker and easier than switching fibers.

The results for the microring isolator with highest isolation ratio is shown in Figure 3.18, in which 32dB of optical isolation is measured near 1555nm. A total of 80mA was supplied to the electromagnet, accounting for 9.6mW of power dissipation given the measured 1.5 Ohm resistance of the electromagnet.

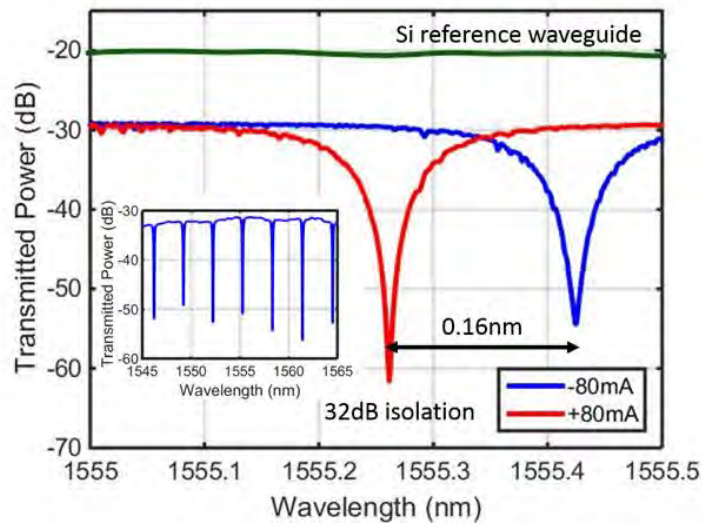


Figure 3.18: Experimental results of the microring isolator showing the difference between forward and backwards transmission.

The optical loss of the device is measured by comparing our device to a straight Si reference waveguide of the same dimensions, but without the bonded Ce:YIG. Of the 10dB loss, we simulate 1.2dB of scattering loss at the interfaces between the channel waveguide with a silica cladding and the Ce:YIG bonded waveguide using Lumerical

FDTD software. The remaining 8.8dB is due to the presence of the Ce:YIG layer. Since the length of the bus (3.5mm) is much longer than the isolator (70 micron diameter) due to placement of splits on the mask as seen in Figure 3.17, there are the equivalent length of eight isolators, including the microstrip and contacts, along the bus waveguide. Therefore, the excess loss of a single isolator is $(1.2+8.8/8) = 2.3\text{dB}$. The excess loss can be further reduced by considering silicon nitride cladding ($n = 2$) in place of silicon dioxide due to a smaller refractive index contrast with the Ce:YIG ($n = 2.22$). This is consistent with the measurement of the loaded quality factor of the microring to be 15000 at the critical coupling condition, or an intrinsic Q near 30000. This gives an estimate of the total loss in ring to be 19.5dB/cm.

The MO resonance wavelength split $\Delta\lambda_{MO}$ between CW and CCW propagation is 0.16nm for the 80mA of applied current, which is far below the simulated 0.55nm of RWS for Ce:YIG with saturated magnetization. Since the microring is narrowband, any resonance split larger than 0.1nm will result in an isolation that is equal to the full extinction ratio of the microring, as is the case here. Therefore, a strong magnet and full saturation of the Ce:YIG magnetization is not needed for optical isolation. Increasing the current increases the magnetic field, which will also increase the RWS. However, the increase in current also heats up the electromagnet, which results in a thermal shift $\Delta\lambda_T$ in the resonant wavelength. The net effect is a shift $\Delta\lambda_T \pm \Delta\lambda_{MO}/2$ on the resonant wavelength, since $\Delta\lambda_T$ is a reciprocal effect, as seen in Figure 3.19. The RWS and thermal shift for a resonance is plotted as a function of applied current.

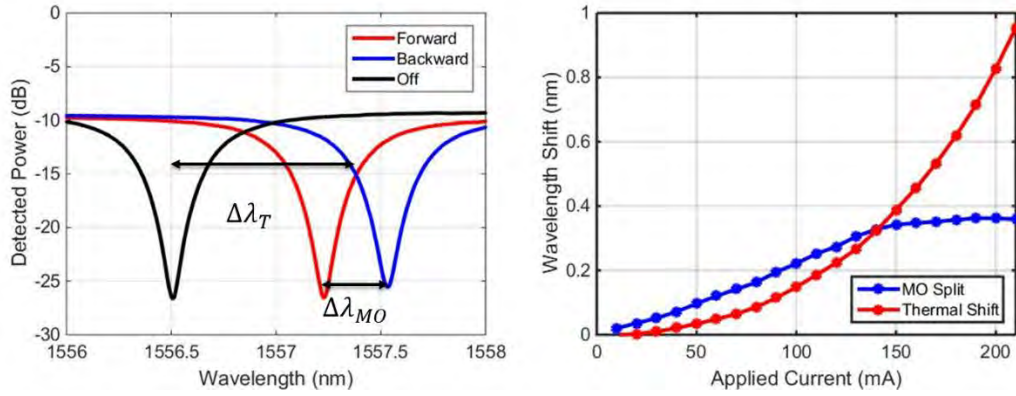


Figure 3.19: Measurements of the thermal induced resonance shift on top of the RWS as a function of the applied current into the microring isolator.

The thermal shift $\Delta\lambda_T$ increases quadratically with current (linearly with power) as expected. This can be used to tune the device to match the operating wavelength of the laser or PIC. For this device, the wavelength can be tuned over roughly 0.9nm while maintaining high (>20dB) isolation. This is limited by the electromagnet, which was observed to degrade at high currents (>250mA). Following device runs showed thermal tuning greater than the FSR of the ring, enabling much wider tunability, which is detailed in Chapter 5.

The RWS seems to increase linearly or sub linearly until it rolls over and saturates at a value of 0.36nm, which is smaller than the predicted 0.55nm. The primary reason for this is the reduction of Faraday rotation at higher temperatures, which was measured to be $\frac{d\theta_F}{dT} = 44^\circ/K$ [31]. Therefore, the RWS is a function of temperature in addition to the magnetic field. The local temperature of Ce:YIG has a strong dependence on the applied current, as well as the SGGG thickness, as discussed in Chapter 2. For the device considered here, the SGGG is measured to be 5 microns thick. The magnetic field and

temperature are plotted in Figure 3.20 as a function of current for this device, using COMSOL Multiphysics.

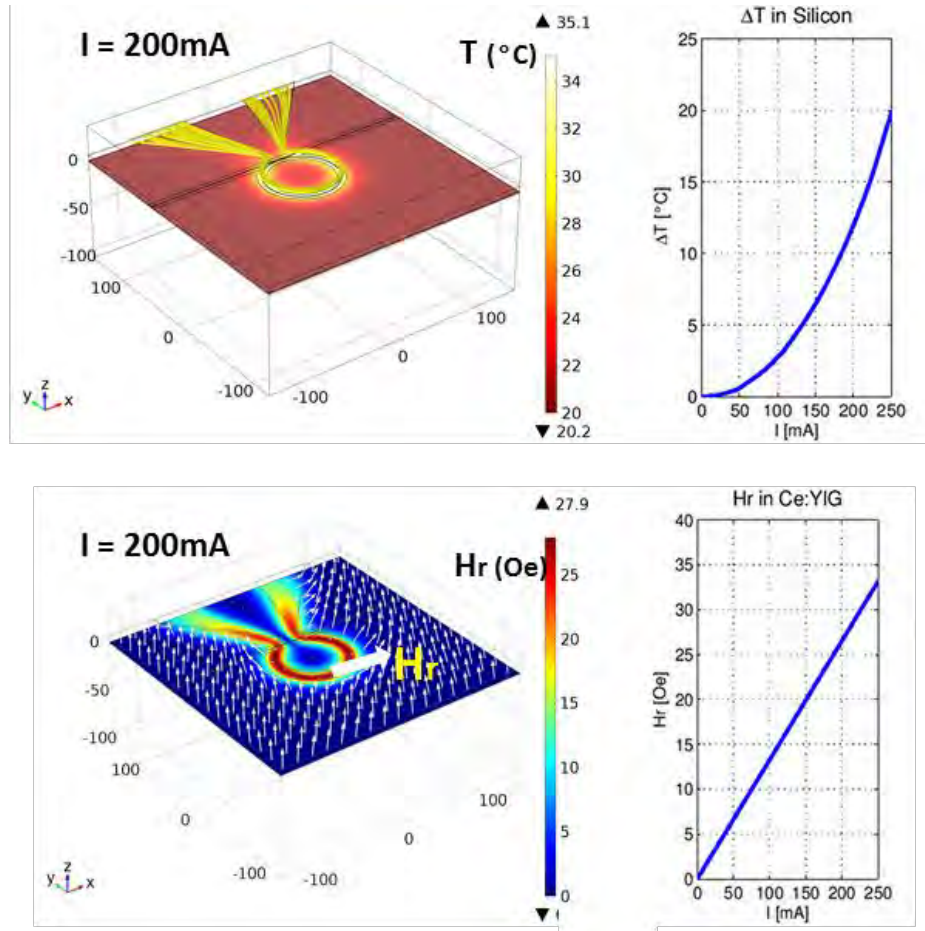


Figure 3.20: Simulations of the magnetic field and temperature in the microring isolator as a function of applied current.

Using these simulations, it is possible to fully model the current dependence on $\Delta\lambda_T$ and $\Delta\lambda_{MO}$, as given in Equations 3.19 and 3.20. Table 2 contains the relevant modal temperature dependences for each material in the waveguide needed for Equation 3.19. The Faraday rotation for Ce:YIG below saturation $\theta_F(H_r)$ was given in Chapter 2, and $\Delta\lambda_{MO}^0$ and θ_F^0 represent the saturated, room-temperature values of RWS (0.55nm) and

Faraday rotation (-4500 deg/cm). The model accurately depicts the device performance of the microring isolator, as shown in Figure 3.21.

$$\Delta\lambda_T(H_r, T) = \frac{\lambda}{n_g} \left(\sum_i \frac{\partial n_{eff}}{\partial n_i} \cdot \frac{\partial n_i}{\partial T} \right) \Delta T \quad (3.19)$$

$$\Delta\lambda_{MO}(H_r, T) = \frac{\Delta\lambda_{MO}^0}{\theta_F^0} \left[\theta_F(H_r) + \frac{d\theta_F}{dT} \cdot \Delta T \right] \quad (3.20)$$

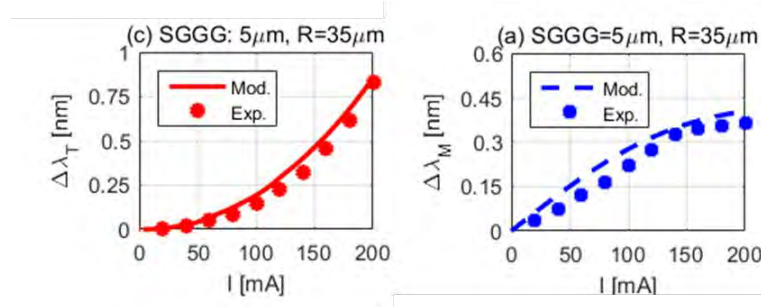


Figure 3.21: Comparison of experimental and predicted thermal and RWS

Material Parameter	dn _i /dT [K ⁻¹]	dn _{eff} /dn _i
Ce:YIG	9.1e-5	0.405
Si	1.86e-4	0.691
SiO ₂	1.0e-5	0.275
Air	1.0e-6	0.021

Table 3.1: Modal refractive index change with temperature.

One of the drawbacks of the microring isolator is the limited isolation bandwidth, that is unavoidable due to the resonant nature of the device. The isolation bandwidth $IR(BW)$ of the device is defined in Equation 3.21 [19]. Here, S_{FW} and S_{BW} represent the field transfer functions of the forward and backward directions respectively.

$$IR(BW) = \frac{\int_{\lambda_{IN}-BW/2}^{\lambda_{IN}+BW/2} |S_{FW}(\lambda)|^2 d\lambda}{\int_{\lambda_{IN}-BW/2}^{\lambda_{IN}+BW/2} |S_{BW}(\lambda)|^2 d\lambda} \quad (3.21)$$

To increase the isolation bandwidth, a device with two cascaded microring isolators is fabricated. To provide the largest isolation, the amplitude of the currents in the two electromagnet is chosen such that the CCW resonances of the two rings are aligned with the input signal wavelength (λ_{IN}), while the CW resonances fall apart, at longer and shorter wavelength, respectively. A schematic plot of each isolator spectra and the cascaded transfer function are shown in Figure 3.22. The light propagates from IN-port to OUT-port without much attenuation, while in the opposite direction the light is coupled into both of the rings. The fabricated devices are also shown, in which smaller microrings with 20 micron radius are used. The rings are separated by 100 microns to reduce thermal crosstalk effects, although the effects were still somewhat present. They are sufficiently far away from each other that there is no magnetic field crosstalk.

The device is tested using the same methods as for the single microring isolator. Near critical coupling was achieved at 1503nm, in which the forward (CW) and backward (CCW) spectrum was recorded in Figure 3.23. The rings were slightly different from each other due to fabrication, such that the driving current in ring 1 (195mA) was slightly different than that of ring 2 (-170mA) to compensate for the wavelength mismatch. A total of 28dB of optical isolation was measured, which is likely limited by the PER of the lensed fiber. Upon adding a polarizer to the output fiber, the isolation was measured to be as large as 36dB.

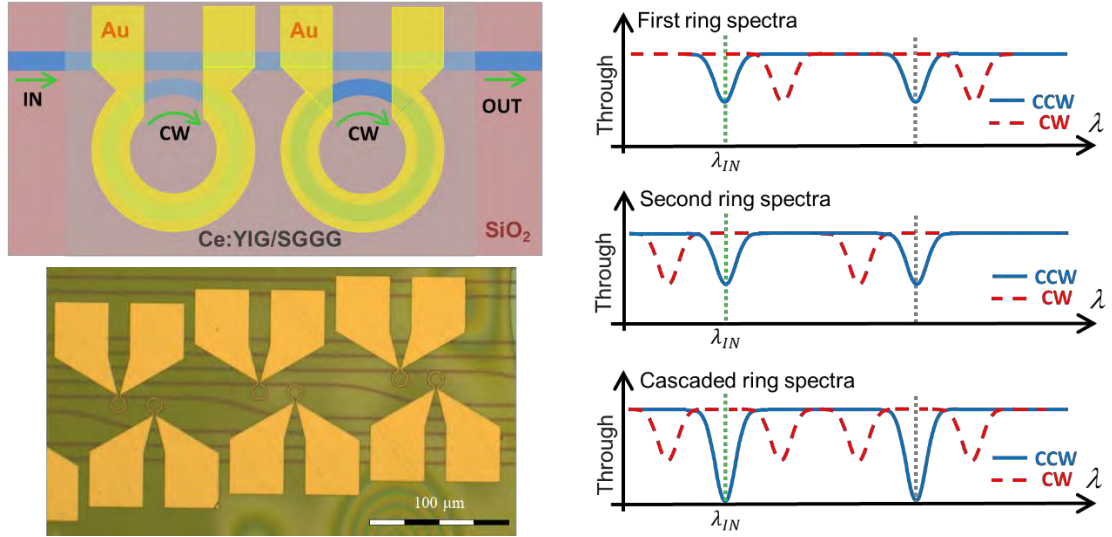


Figure 3.22: Schematic, micrograph, and principle of operation for the cascaded microring isolator.

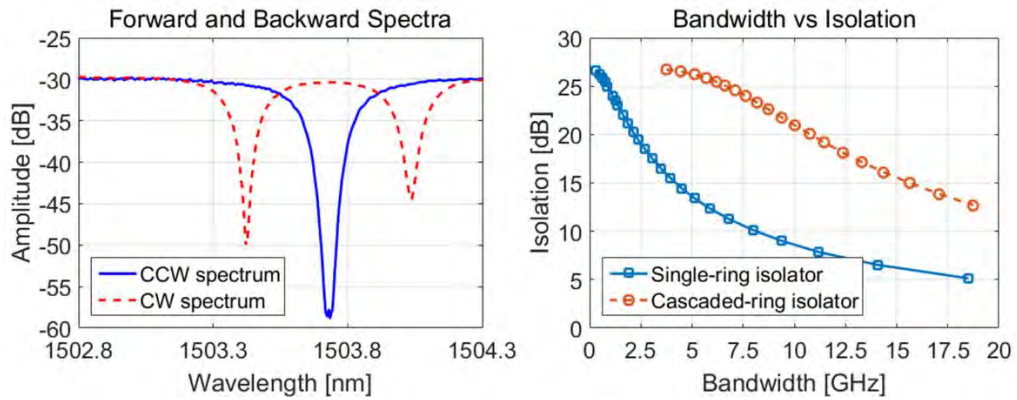


Figure 3.23: Experimental results of the cascaded microring isolator showing nonreciprocal transmission between the forward and backward directions over a larger optical bandwidth.

The isolation bandwidth of the cascaded ring isolator is calculated according to Equation 3.21, and compared with that of a single ring isolator. From Figure 3.23, the cascaded ring isolator significantly improves the isolation bandwidth, with over 10GHz of bandwidth at 20dB of isolation compared with only 2.5GHz for a single ring. Adding additional rings could increase the isolation bandwidth further, although other

problems will arise. One such problem is an increase in insertion loss, as each ring adds some loss, even when off-resonance. Another problem is the addition of more electromagnets introduces more power dissipation and heating, which will reduce the RWS.

At most, the 20dB-isolation bandwidth will be equal to roughly half the RWS (around 20GHz at 1550nm), or the overlap between CW and CCW spectra will be significant, leading to increased loss. Therefore, for systems that require wideband optical isolation, such as a modulated light source at 25 or 50 GBaud for data communications, the microring isolator could be of limited use on its own. A simple workaround to this problem is to include an add-drop microring filter in series with the optical isolator. This additional ring can be silicon only and have a higher quality factor than the microring isolator. Thus, it can filter out all the reflections outside the isolation bandwidth of the isolator, as it is more narrowband. Alternatively, A wideband isolator based on a Mach-Zehnder interferometer which can satisfy these bandwidth requirements is the topic of Chapter 4.

3.3 Microring optical circulator

Design

The microring optical circulator makes use of the add-drop ring architecture rather than the all-pass architecture used for the isolator. The operating principle is almost identical to that of the microring optical isolator, except the light in the resonator is

coupled into a second waveguide adjacent to the ring. The device has four optical ports, and the light circulates in a nonreciprocal fashion when a radial magnetic field is applied.

When the magnetic field is pointing radially inwards, the operating wavelength is aligned to the CCW resonance of the ring, as in Figure 3.24. Under these conditions, the wavelength of light entering from port 1 (red arrow) is not aligned with the ring resonance, and therefore the light passes through to port 2. Meanwhile, light injected from port 2 (blue arrow) excites the CW ring resonance, and it will be dropped to port 3. Thus, the circulation direction in this configuration is 1->2->3->4->1. If the magnetic field is flipped to a radially outward direction, as shown in the bottom half of Figure 3.24, then the same operating wavelength is now aligned to the CW resonance. In this alternate configuration, the light circulates from 1->4->3->2->1. Thus, the circulation direction can be reconfigured by simply switching the direction of current in the electromagnet. This also opens the possibility of using the device as a nonreciprocal switching element, which is further discussed in Chapter 7.

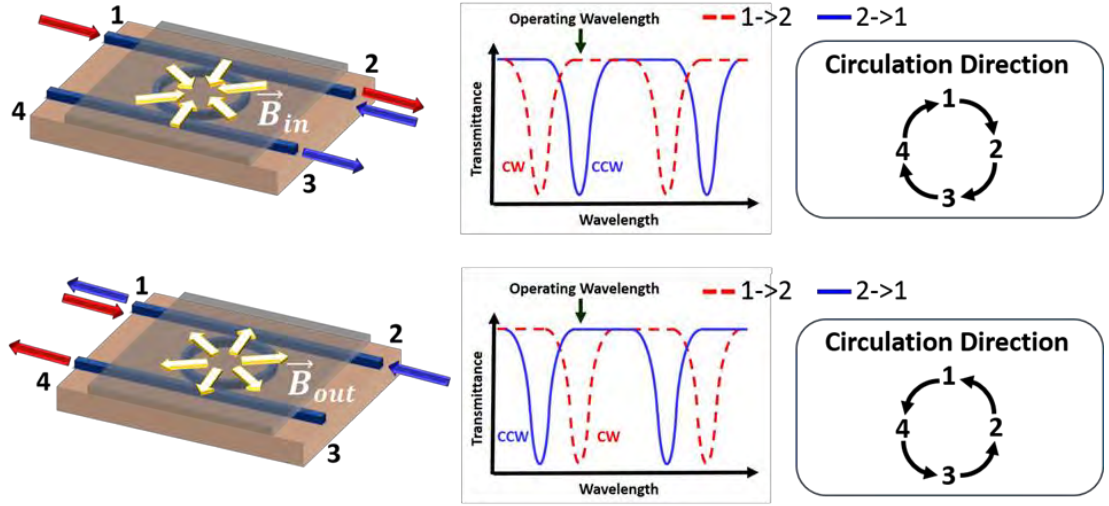


Figure 3.24: Schematic of microring optical circulator

For a multi-port device such as a circulator, the transfer function of the device is best represented by a scattering matrix. In Equation 3.22, a 4x4 matrix relates the amplitudes of the input (A_i^+) and output (A_j^-) fields at each of the ports, with the assumption that backscattering is negligible.

$$\begin{pmatrix} A_1^- \\ A_2^- \\ A_3^- \\ A_4^- \end{pmatrix} = \begin{pmatrix} 0 & S_{12} & 0 & S_{14} \\ S_{21} & 0 & S_{23} & 0 \\ 0 & S_{32} & 0 & S_{34} \\ S_{41} & 0 & S_{43} & 0 \end{pmatrix} \begin{pmatrix} A_1^+ \\ A_2^+ \\ A_3^+ \\ A_4^+ \end{pmatrix} \quad (3.22)$$

Furthermore, the device is designed with symmetric couplers on each side of the ring, such that $S_{12} = S_{34}$, $S_{21} = S_{43}$, $S_{14} = S_{32}$, and $S_{41} = S_{23}$. Critically, the device is nonreciprocal, so the scattering matrix is not symmetric $S_{ij}(\lambda) \neq S_{ji}(\lambda)$. Instead, given the equivalence of switching magnetic field and propagation direction, Equation 3.23 is true.

$$S_{ij}(\lambda \pm \Delta_{MO}/2) = S_{ji}(\lambda \mp \Delta_{MO}/2) \quad (3.23)$$

The design of the circulator follows the same principles as the isolator, in which the NRPS is maximized. Therefore, it has the same waveguide cross-section. The selection of coupling gap is once again key to the design, as it determines the extinction ratio and isolation ratio as given in Equations 3.10 and 3.11. The gap and the ring-waveguide power coupling coefficient ($K=\kappa^2$) has been chosen so that S41, S34, S23 and S12 have the same amplitude at the operating wavelength λ_{IN} . This occurs at a coupling power of roughly 11.9%, as shown in Figure 3.25. An alternate design strategy is to select the coupling gap such that the isolation ratio between the different port combinations is the same. This results in an optimal coupling gap of 10.5%.

Ultimately, the difference between these designs was within the fabrication accuracy of the gap, which is targeted to be ± 15 nm. The splits on mask were centered around a gap of 220nm. Simulations predict an isolation ratio of 13dB between all the ports. In some cases, the isolation ratio between two of the ports is more important than the others, since the input port is fixed. Examples of this include the use of a circulator in a fiber Bragg grating sensor. In these scenarios, the design of the circulator can be changed such that the two coupling gaps are not the same, such that the ring is in the critical coupling regime.

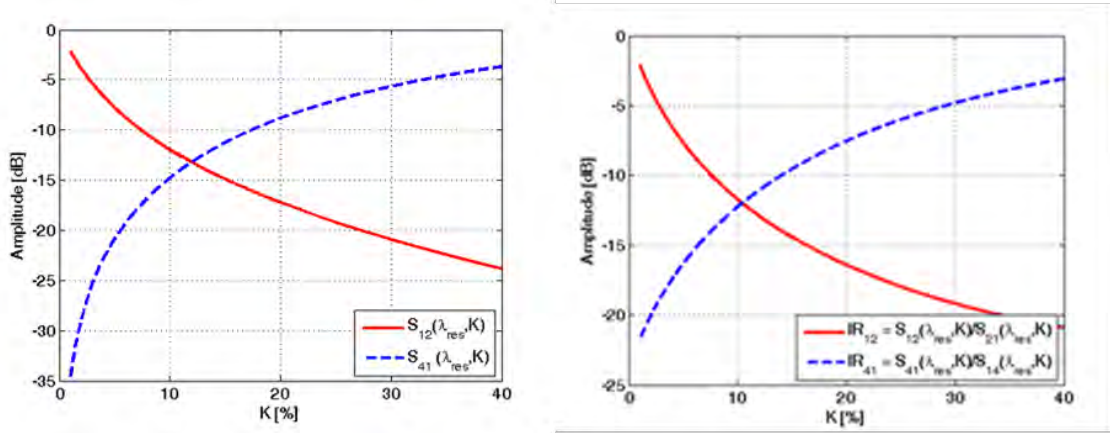


Figure 3.25: Extinction ratio between various ports for different design criteria regarding the coupling strength into the ring.

Characterization

The device is fabricated using the same procedure as the microring optical isolator. We characterize the device at room temperature (20°C) using a similar setup to the one used for the optical isolator. A polarization maintaining (PM) lensed fiber as input, while fibers are aligned to Ports 2 and 4 simultaneously. This is done by angling the facets on the ports in opposite directions, such that two fibers can approach the chip on the same side at once, as shown in Figure 3.26. This can also be realized by using a PM fiber array such as the one offered by Chiral Photonics [32]. The tunable laser is swept and the power at each of the ports is recorded. Finally, the measurement is repeated for each of the input ports of the circulator and depicted in Figure 3.27 for an operating current of 200mA. The experimental results on the left match up extremely well with the simulations on the right.

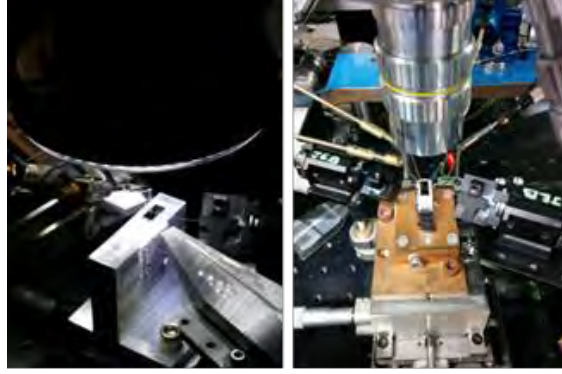


Figure 3.26: Picture of test setup used to characterize optical circulators

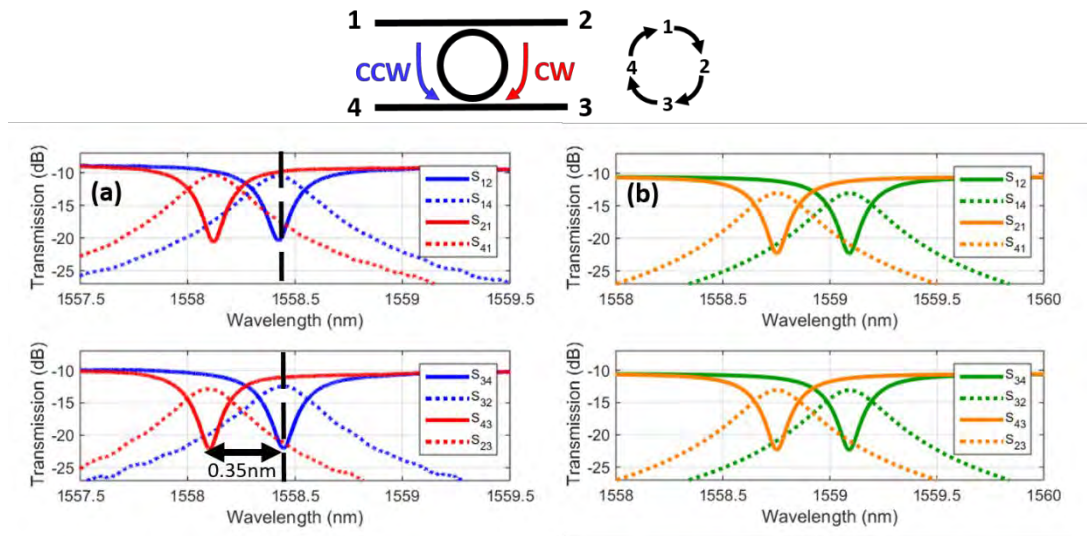


Figure 3.27: Simulated and experimental spectra of the transmission through the microring circulator operating near 1558nm.

From the experimental results, the scattering matrix can be extracted at the operating wavelength of 1558.4nm, as shown in Table 3.2. The missing entries are paths that are only obtainable due to strong back-reflection. The values of S_{13} , S_{31} , S_{24} , and S_{42} are very low (less than -40dB), and the measurement to quantify the backscattered light at each port (S_{ii} , for $i=1,2,3,4$) is dominated by reflections off the polished facet as well as the lensed fiber used for the coupling.

		Input Port			
		1	2	3	4
Output Port	1	-	-20.7	-	-10.5
	2	-9.7	-	-21.0	-
	3	-	-12.4	-	-22.0
	4	-17.2	-	-11.0	-

Table 3.2: Measured S-matrix values for the optical circulator in dB. These values are extracted from the measurements in Figure 3.27.

In this table, the highlighted entries depict the insertion loss for the forwards circulating path and range from 9.7dB to 12.4dB. Such large values are due to the Ce:YIG clad bus waveguides (3.5mm) which are much longer than the actual microring size and can be straightforwardly reduced.

As formerly stated, the isolation ratio is defined as the ratio of forward to backward transmitted power between two adjacent ports. The largest isolation ratio is 11dB and it is measured between Port 1 and Port 2, and between Port 3 and Port 4 (i.e., IR12 and IR34). Vice versa, the smallest isolation ratio is 6.7dB that is measured between Port 1 and Port 4 (i.e., IR14). Another important key feature to evaluate the performance of the device is the crosstalk at the output port (XT). It can be defined as the ratio between the sum of transmitted signal powers from all undesired ports and the transmitted signal power from the desired output port. From Table III, it is calculated as the difference between the entries in any horizontal row. The crosstalk in this device ranges from -6.2dB at Port 4, to -11.3dB at Port 2. The results are summarized below in Table 3.3.

	$\Delta\lambda_{M0}=0.55$ (simulated)	$\Delta\lambda_{M0}=0.35$ (simulated)	$\Delta\lambda_{M0}=0.35$ (experiment)
$IR_{12}= S_{21} ^2/ S_{12} ^2$	12.0 dB	11.6 dB	11.0 dB
$IR_{23}= S_{32} ^2/ S_{23} ^2$	12.0 dB	8.5 dB	8.6 dB
$IR_{34}= S_{43} ^2/ S_{34} ^2$	12.0 dB	11.6 dB	11.0 dB
$IR_{41}= S_{14} ^2/ S_{41} ^2$	12.0 dB	8.5 dB	6.7 dB
$XT_1= S_{12} ^2/ S_{14} ^2$	-14.3 dB	-10.18 dB	-10.2 dB

$\text{XT}_2= S_{23} ^2/ S_{21} ^2$	-10.0 dB	-10.0 dB	-11.3 dB
$\text{XT}_3= S_{34} ^2/ S_{32} ^2$	-14.3 dB	-10.18 dB	-9.6 dB
$\text{XT}_4= S_{41} ^2/ S_{43} ^2$	-10.0 dB	-10.0 dB	-6.2 dB

Table 3.3: Optical isolation and crosstalk between the ports for the device measured in Figure 3.27.

The measured IR are smaller than the simulated values because the device is operating below the saturation magnetization value ($\Delta\lambda_{MO}<0.55\text{nm}$), as shown in the table. Both the isolation ratio and the crosstalk of the device can be improved by increasing the RWS and differentiating the CW and CCW resonance even further. Alternatively, a higher order ring filter can be used, such as a 2nd order coupled ring.

The demonstrated 4-port circulator can be used as a building block for more complex nonreciprocal devices and networks. Here, we demonstrate how our device design can be expanded to realize circulators with an arbitrary number of input/output ports. We will only consider devices using the microring architecture; nevertheless, the principles shown here can be carried over to design multi-port MZI circulators as well. In this section, we present for the first time, to the best of our knowledge, a fully circulating, dynamically reconfigurable 6-port optical circulator with up to 14.4dB of isolation.

The simplest design for a multi-port microring circulator involves a single central ring with multiple bus waveguides. While the simplicity in only using one ring is attractive, the optical crosstalk between the ports would likely be a critical issue due to the recirculation of the signal in the central ring. Moreover, the footprint will enlarge with increasing number of ports. An alternate design that we present here uses multiple rings laid out in the geometry depicted below. Figure 3.28 shows the schematic for a six port circulator using two identical rings and three bus waveguides. In general, this multi-port architecture can be easily expanded to an arbitrary number of ports. If we use (N-

1) rings with (N) bus waveguides, we are able to achieve a circulator with (2N) ports. Odd numbers of ports can be realized by using a loop mirror at the end of one of the bus waveguides, as was previously demonstrated with a 3-port circulator.

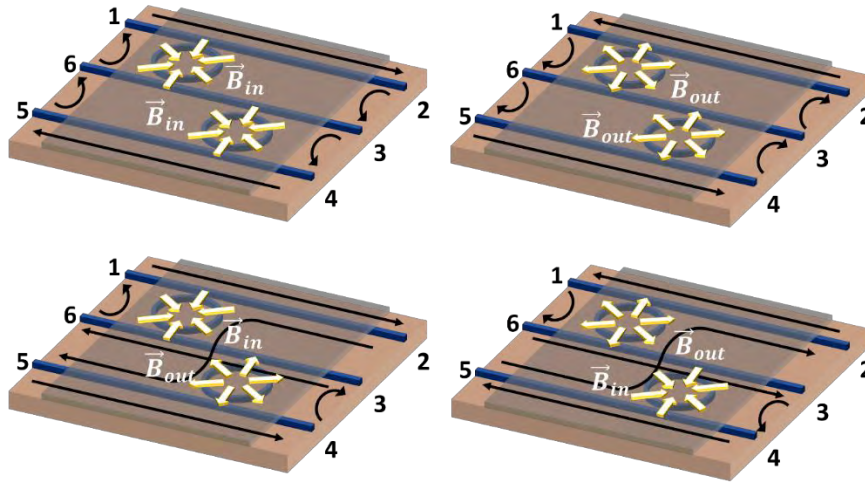


Figure 3.28: Schematic of a six-port microring circulator

As long the rings are separated far enough such that the magnetic field in one ring does not significantly affect the others, then we can magneto-optically tune the (N-1) rings independently and reconfigure the circulator in $2(N-1)$ ways. For a six-port circulator, it is possible to obtain the four different configurations shown above depending on the orientation of the magnetic field in the two rings. We fabricated this six-port optical circulator using two 20 micron radius ring resonators and three bus waveguides. In theory, the rings should be identical with the same resonance wavelength, but this is often not the case due to fabrication imperfections and non-uniformities of the wafer or the etch process. Our result shows the intrinsic resonances of the two rings are over 1nm apart, meaning they must be thermally tuned together in order for the circulator to operate at a common wavelength for all of the ports.

Furthermore, we must apply enough current to observe a significant RWS in each of the rings for nonreciprocal behavior.

In this design, the single microstrip can be used to meet both aforementioned requirements for single wavelength circulation and compensate the fabrication. Applying different current in each ring, we found that the optimal conditions for 6-port circulation in the device under test are $I_1=\pm 185\text{mA}$ for the top ring and $I_2=\pm 262\text{mA}$ for the bottom ring. Due to the angling of the output facets and limited spacing between adjacent facets, it was not possible to simultaneously test all input and output combinations. Instead, we use each of the six ports as an input successively and measure the transmission spectra through all the accessible output ports, as shown below in Figure 3.29.

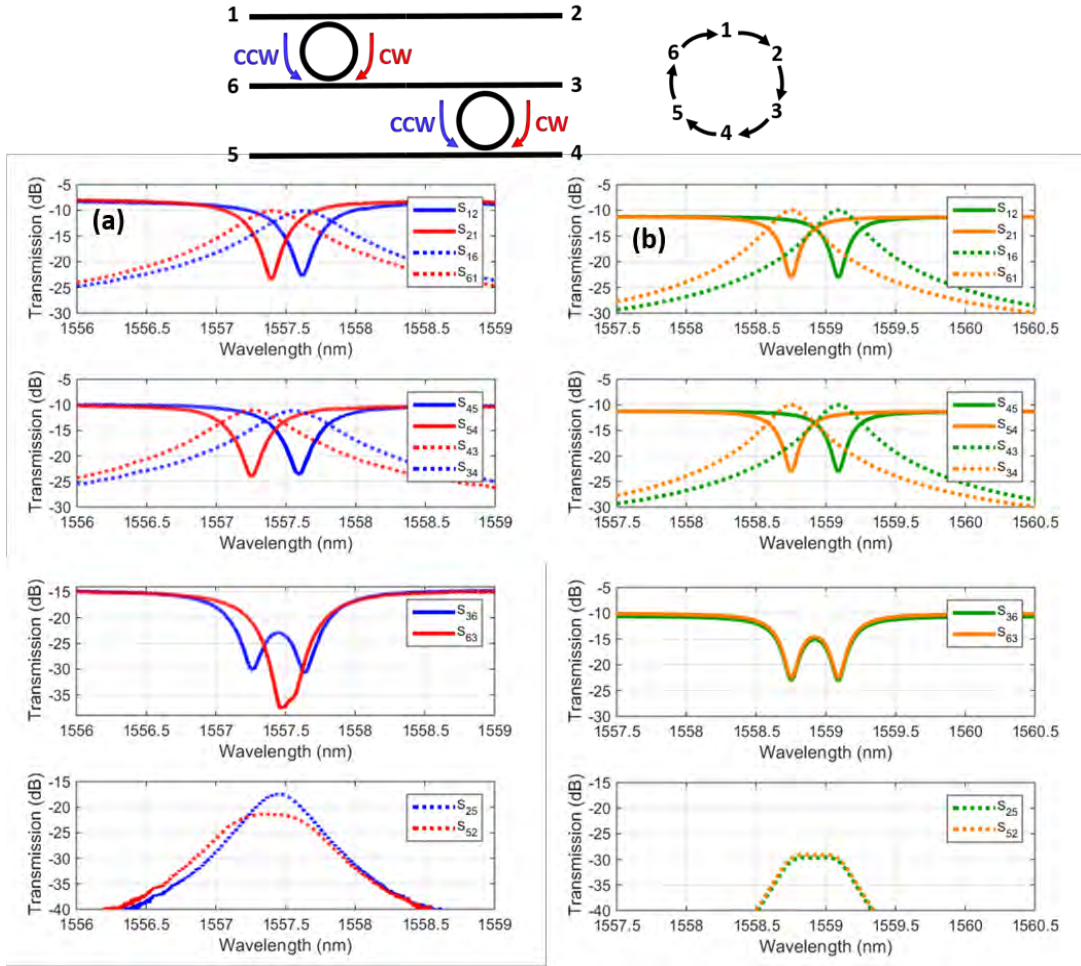


Figure 3.29: Simulated (left) and experimental (right) transmission spectra of the six-port circulator operating near 1557.5nm.

		Input Port					
		1	2	3	4	5	6
Output Port	1	-	-22.5	-	-	-	-10.1
	2	-11.2	-	-26.5	-	-20.4	-
	3	-	-12.1	-	-15.5	-	-29.3
	4	-	-	-11.3	-	-23.5	-
	5	-	-23.0	-	-12.0	-	-27.0
	6	-12.6	-	-30.3	-	-14.3	-

Table 3.4: Measured S-matrix values for the six-port optical circulator in Figure 3.29 in dB.

Although the predicted RWS is 0.35nm, from the measured spectra we observe a RWS of 0.25nm for the top ring while the RWS of the bottom one is 0.35nm. This is reasonable considering the applied current was larger for the bottom ring in order to compensate the fabrication variation. In this configuration, the operating wavelength near 1557.6nm is on resonance with the CCW modes of both rings, causing a circulation path of 1->2->3->4->5->6->1. From these measurements we can extract the scattering parameters of the device at the working wavelength. Once again, the highlighted entries show the insertion loss along the forward circulation path, and the isolation and crosstalk for each port can be extracted by analyzing the table. Here, we find the largest isolation ratio is 14.4dB between Ports 2 and Port 3, while the smallest isolation ratio is 2.5dB between Ports 1 and Port 6. The insertion losses along the forward circulating path range from 10.1 to 14.3dB, which is similar to what was measured in the 4-port device, and can be reduced by shortening the length of the Ce:YIG cladding above the bus waveguides. Overall better device performance can be achieved by aligning the resonances with better fabrication accuracy or a separate thermal tuner. Alternatively, a coupled ring resonator system (with two or more rings) can be used to increase the extinction ratio.

Coupled ring circulators

A schematic of the coupled microring circulator is shown in Figure 3.30. Coupled ring resonators are often used to increase the extinction ratio, the pass band flatness, as well as the roll-off of the filter [33]. These characteristics are also applicable to the design of microring circulators. Since the light propagates in the two rings in opposite directions,

it is necessary to align the CW resonance of one with the CCW resonance of the other. To do this, individual electromagnets should be included on each ring, to allow for independent control of the local magnetic field as well as the temperature. A comparison of predicted isolation ratio and bandwidth between the single ring circulator and the coupled ring circulator is shown in Figure 3.30. The isolation of both the through ports (1->2) as well as the drop ports (1->4) are shown. Compared with the single ring, the coupled ring offers higher isolation ratios up to 18dB, while maintaining the same bandwidth characteristics.

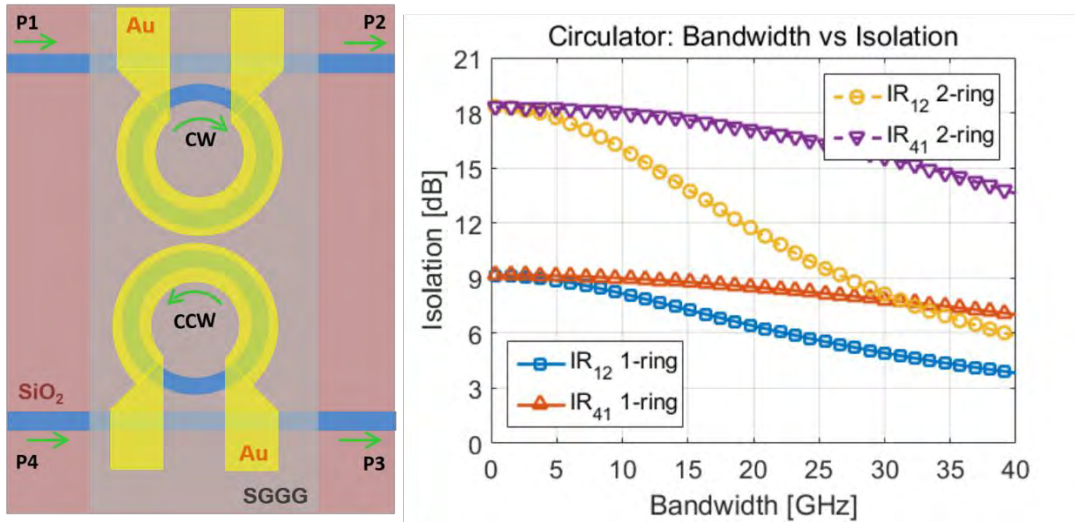


Figure 3.30: Schematic and simulated performance of a coupled ring circulator showing the improvement in isolation bandwidth and ratio compared with a single ring.

This device was fabricated using the same procedures detailed for other devices in this chapter. Due to fabrication imperfections, the two rings must be thermally tuned together. The electromagnet was also placed higher above the waveguides (10 microns) than usual, due to some difficulties in the substrate thinning. This led to a less than optimal 0.25nm RWS, which decreased the achievable isolation ratio since the CW and

CCW spectra have significant overlap. Nevertheless, the demonstration showed that the extinction ratios in Figure 3.31 could be as high as 18dB, which far exceeds the performance of the single ring circulator. If the fabrication can be improved such that the RWS is as large as 0.4nm, then the benefits of using a coupled microring circulator would be realized.

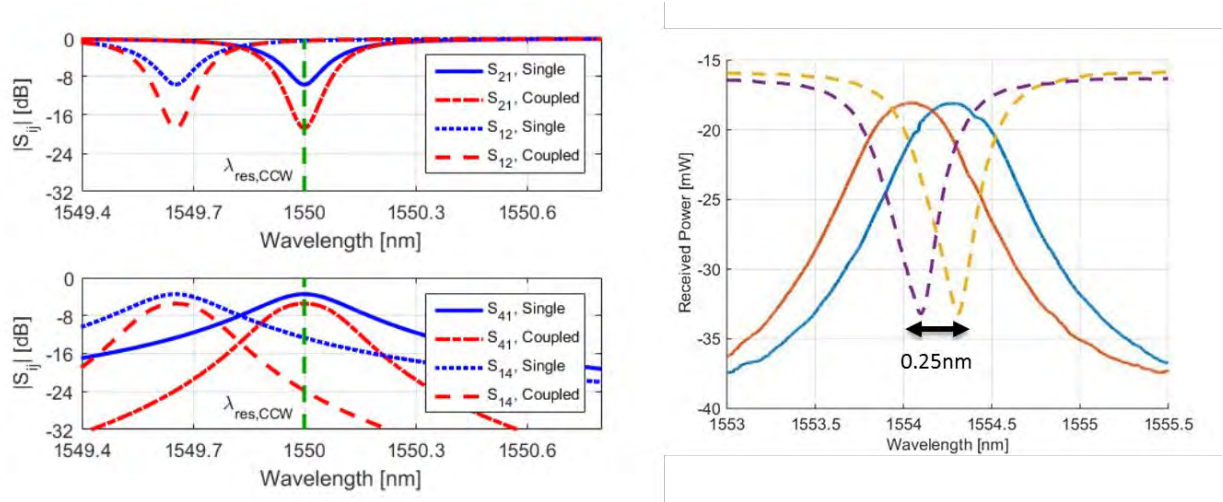


Figure 3.31: Simulated (left) and experimental (right) transmission spectra of the coupled ring circulator.

Summary

The microring resonator is a key device in present day and future photonic integrated circuits due to its small footprint, low power consumption, and ease of fabrication. When magneto-optic material is introduced into the resonator, the symmetry of the system is broken, and the resonant conditions for clockwise and counterclockwise propagating light are different. This can be used to create microring optical isolators and circulators. The electromagnet is key to this device, as it allows for a radial magnetic field to be generated along the entire microring, rather than a uniform

field placed along straight sections. This increase the interaction length of the MO effect, which resulted in a record resonant wavelength split of 0.35nm between the CW and CCW modes and isolation ratios up to 32dB. This can be further improved if less heating is generated by the electromagnet, as Faraday rotation decreases with temperature.

On the other hand, the extreme wavelength sensitivity to fabrication and environmental conditions in the ring can be overcome by thermal tuning, which is easily achieved by the electromagnet. For larger photonic integrated circuits which may involve multiple microrings, this tunability is critical. All of the typical scalability arguments associated with microrings apply to isolators and circulators, meaning that multiple rings can be combined to create nonreciprocal photonic networks.

Despite these attractive features, the microring isolator has low operating bandwidth. One way to increase the isolation bandwidth is to use higher order filters in the form of cascaded or coupled microresonators. However, despite these improvements, the isolation bandwidth remains on the order of 10GHz, which is not sufficient for most data transmission experiments. For these applications, a non-resonant device such Mach-Zehnder interferometer is preferred for their large operating bandwidth. These devices are discussed in the next chapter. A summary of the demonstrated devices in this chapter and their relevant parameters is given below.

Single Microring Isolator (TM-mode)	Value
Ring Radius	35 microns
Coupling Gap	270nm
Resonance Wavelength Split	0.35nm @ 200mA
Power Consumption	9.6mW @ 80mA
Isolation Ratio	32dB
20dB Isolation Bandwidth	2.5 GHz
Insertion Loss	Total 10dB, Extracted 2.3dB single device

Cascaded Microring Isolator (TM-mode)	Value
Ring Radius	20 microns
Coupling Gap	240nm
Resonance Wavelength Split	0.31nm (x2) @ 200mA
Power Consumption	62mW @ ~190mA
Isolation Ratio	36dB
20dB Isolation Bandwidth	10 GHz
Insertion Loss	Total 10dB

4-port Microring Circulator (TM-mode)	Value
Ring Radius	20 microns
Coupling Gap	220nm
Resonance Wavelength Split	0.35nm @ 200mA
Power Consumption	34.4mW @ 200mA
Isolation Ratio	12.4dB
20dB Isolation Bandwidth	N/A
Insertion Loss	~ 10dB

6-port Microring Circulator (TM-mode)	Value
Ring Radius	20 microns
Coupling Gap	220nm
Resonance Wavelength Split	0.35nm @ 200mA
Power Consumption	89.1mW @ 260mA
Isolation Ratio	14.4dB
20dB Isolation Bandwidth	N/A
Insertion Loss	~ 10dB

References

1. W. Bogaerts, P. de Heyn, T. van Vaerenbergh, K. de Vos, S. Kumar Selvaraja, T. Claes, P. Dumon, P. Bienstman, D. van Thourhout, and R. Baets, "Silicon microring resonators," *Laser Photonics Rev.* **6**, 47–73 (2012).
2. H. Kroemer, J. Bowers, and M.-C. Tien, "Ring resonator based optical isolator and circulator," U.S. patent 8,396,337 B2 (2013).
3. J. Heebner, R. Grover, and T. Ibrahim, *Optical Microresonators. Theory, Fabrication and Application* (Springer, 2008).
4. A. Melloni, F. Morichetti, and M. Martinelli, "Polarization conversion in ring resonator phase shifters," *Opt. Lett.* **29**, 2785 (2004).
5. B. E. Little, J.-P. P. Laine, and S. T. Chu, "Surface-roughness-induced contradirectional coupling in ring and disk resonators," *Opt. Lett.* **22**, 4–6 (1997).
6. M. A. Popović, C. Manolatou, and M. Watts, "Coupling-induced resonance frequency shifts in coupled dielectric multi-cavity filters," *Opt. Express* **14**, 1208–1222 (2006).
7. G. Cusmai, F. Morichetti, P. Rosotti, R. Costa, and A. Melloni, "Circuit-oriented modelling of ring-resonators," *Opt. Quantum Electron.* **37**, 343–358 (2005).
8. D. T. Spencer, J. F. Bauters, M. J. R. Heck, and J. E. Bowers, "Integrated waveguide coupled Si₃N₄ resonators in the ultrahigh-Q regime," *Optica* **1**, 153 (2014).
9. P. E. Barclay, K. Srinivasan, and O. Painter, "Nonlinear response of silicon photonic crystal microresonators excited via an integrated waveguide and fiber taper," *Opt. Express* **13**, 801 (2005).
10. L. Luo, G. S. Wiederhecker, J. Cardenas, C. Poitras, and M. Lipson, "High quality factor etchless silicon photonic ring resonators," *Opt. Express* **19**, 6284 (2011).
11. Z. Wang and S. Fan, "Optical circulators in two-dimensional magneto-optical photonic crystals," *Opt. Lett.* **30**, 1989 (2005).
12. N. Kono and M. Koshiba, "Three-dimensional finite element analysis of nonreciprocal phase shifts in magneto-photonic crystal waveguides," *Opt. Express* **13**, 9155–9166 (2005).
13. N. Kono, K. Kakihara, K. Saitoh, and M. Koshiba, "Nonreciprocal microresonators for the miniaturization of optical waveguide isolators," *Opt. Express* **15**, 7737–7751 (2007).

14. D. Jalas, A. Petrov, M. Krause, J. Hampe, and M. Eich, "Resonance splitting in gyrotropic ring resonators," October **35**, 3438–3440 (2010).
15. M.-C. Tien, T. Mizumoto, P. Pintus, H. Kromer, and J. E. Bowers, "Silicon ring isolators with bonded nonreciprocal magneto-optic garnets," *Opt. Express* **19**, 11740 (2011).
16. L. Bi, J. Hu, P. Jiang, D. H. Kim, G. F. Dionne, L. C. Kimerling, and C. A. Ross, "On-chip optical isolation in monolithically integrated non-reciprocal optical resonators," *Nat. Photonics* **5**, 758–762 (2011).
17. D. Huang, P. Pintus, C. Zhang, Y. Shoji, T. Mizumoto, and J. E. Bowers, "Electrically driven and thermally tunable integrated optical isolators for silicon photonics," *IEEE J. Sel. Top. Quantum Electron.* **22**, 271–278 (2016).
18. D. Huang, P. Pintus, C. Zhang, Y. Shoji, T. Mizumoto, and J. Bowers, "Silicon microring isolator with large optical isolation and low loss," *Opt. Fiber Commun. Conf. Th1K.2* (2016).
19. P. Pintus, D. Huang, C. Zhang, Y. Shoji, T. Mizumoto, and J. E. Bowers, "Microring-Based Optical Isolator and Circulator with Integrated Electromagnet for Silicon Photonics," *J. Light. Technol.* **35**, 1429–1437 (2017).
20. P. Pintus, T. Mizumoto, and J. E. Bowers, "Novel Nonreciprocal Devices with Integrated Electromagnet for Silicon Photonics," *Eur. Conf. Opt. Commun. ECOC* 704–706 (2016).
21. D. Liang, G. Roelkens, R. Baets, and J. E. Bowers, "Hybrid integrated platforms for silicon photonics," *Materials (Basel)*. **3**, 1782–1802 (2010).
22. S. Ghosh, S. Keyvavinia, W. Van Roy, T. Mizumoto, G. Roelkens, W. Van Roy, T. Mizumoto, G. Roelkens, and R. Baets, "Ce:YIG/Silicon-on-Insulator waveguide optical isolator realized by adhesive bonding," *Opt. Express* **20**, 1839 (2012).
23. Y. Shoji, K. Miura, and T. Mizumoto, "Optical nonreciprocal devices based on magneto-optical phase shift in silicon photonics," *J. Opt. (United Kingdom)* **18**, (2015).
24. B. Cleanroom, "Oxide Growth Calculator," <https://cleanroom.byu.edu/OxideTimeCalc>.
25. Y. Shoji, M. Ito, Y. Shirato, and T. Mizumoto, "MZI optical isolator with Si-wire waveguides by surface-activated direct bonding," *Opt. Express* **20**, 18440 (2012).
26. D. Liang, J. E. Bowers, D. C. Oakley, A. Napoleone, D. C. Chapman, C.-L. Chen, P. W. Juodawlkis, and O. Radaý, "High-Quality 150 mm InP-to-Silicon Epitaxial Transfer for Silicon Photonic Integrated Circuits," *Electrochem. Solid-State Lett.* **12**, H101

- (2009).
27. T. Amemiya, A. Ishikawa, Y. Shoji, P. N. Hai, M. Tanaka, T. Mizumoto, T. Tanaka, and S. Arai, "Three-dimensional nanostructuring in YIG ferrite with femtosecond laser," *Opt. Lett.* **39**, 212 (2014).
 28. M. Bruel, "The History , Physics , and Applications of the Smart-Cut ® Process," *MRS Bull.* 35–39 (1998).
 29. M. Levy, "The On-Chip Integration of Magneto-optic Waveguide Isolators," *IEEE J. Sel. Top. Quantum Electron.* **8**, 1300–1306 (2002).
 30. M. Levy, R. M. Osgood, A. Kumar, and H. Bakhru, "Crystal ion slicing of single-crystal magnetic garnet films," *J. Appl. Phys.* **83**, 6759–6761 (1998).
 31. K. Furuya, T. Nemoto, K. Kato, Y. Shoji, and T. Mizumoto, "Athermal operation of a waveguide optical isolator based on canceling phase deviations in a Mach-Zehnder interferometer," *J. Light. Technol.* **34**, 1699–1705 (2016).
 32. "Chiral Photonics PROFA (1D)," <https://www.chiralphotonics.com/products/one-dimensional>.
 33. P. Pintus, F. Gambini, S. Member, D. Fowler, M. Fournier, S. Faralli, C. Kopp, and C. J. Oton, "Large-FSR Thermally Tunable Double-Ring Filters for WDM Applications in Silicon Photonics Large-FSR Thermally Tunable Double-Ring Filters for WDM Applications in Silicon Photonics," *IEEE Photonics J.* **9**, 1–10 (2017).

Chapter 4

Mach-Zehnder interferometer (MZI) based isolators and circulators

The previous chapter covered resonant nonreciprocal devices using the microring architecture. The main concern with such devices is the limited bandwidth of operation. When considering wideband operation ranging from tens to hundreds of GHz, a non-resonant interferometric device can be considered such as a Mach-Zehnder interferometer. Other devices such as directional couplers, multimode interferometers (MMI) can also be used, but the MZI structure is attractive due to its ability to operate in a push-pull regime. This is a common technique seen in optical modulators, and effectively halves the working length of the device. The free spectral range of a MZI can easily be adjusted by changing the path imbalance between the arms, which is used to tune the isolation bandwidth of the isolator.

4.1 Mach-Zehnder Interferometers

While the previous section covered resonant nonreciprocal devices, it is also possible to utilize the NRPS effects in a nonresonant interferometer. One widely used optical

device is the Mach-Zehnder interferometer, or MZI. The basic working principle of a MZI is to split a coherent light source into two beams, and then recombine them after each beam has propagated a certain distance. Interference will occur when the beams combine, which is sensitive to the relative phase $\Delta\varphi$ between the two beams. In the case that the two arms are identical, the MZI is in a balanced configuration. As with the microring, the MZI is a widely used building block in integrated photonics, and the basic concepts are reviewed here. A schematic of a 1x2 MZI is shown below in Figure 4.1. In its simplest configuration, it has an input port, an output port, and a pair of 1:2 splitters such as a Y-junction.

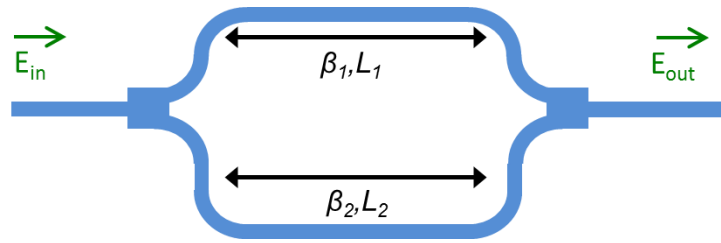


Figure 4.1: Schematic of a MZI using a pair of 1x2 splitters

If the two splitters are identical and 50:50, the field and power transfer function of the MZI can be expressed in Equations 4.1 and 4.2. Note that the propagation losses are ignored here, which is valid if waveguide losses are low and the two arms are close in length.

$$\frac{E_{out}}{E_{in}} = \frac{1}{2}(e^{-j(\beta_2 L_2)} + e^{-j(\beta_1 L_1)}) \quad (4.1)$$

$$\frac{|E_{out}|^2}{|E_{in}|^2} = \cos^2\left(\frac{\beta_2 L_2 - \beta_1 L_1}{2}\right) = \cos^2\left(\frac{\Delta\varphi}{2}\right) \quad (4.2)$$

From these equations, it is apparent that transmission is near unity when the phase difference is an integer multiple of 2π , and zero for odd multiples of π . Spectrally, the transmission through the MZI will have fringes separated by an FSR given in Equation 4.3 where ΔL is the physical path difference $|L_2 - L_1|$.

$$FSR = \frac{\lambda^2}{\Delta L \cdot n_g} \quad (4.3)$$

The same analysis can be extended to a 2x2 MZI depicted in Figure 4.2. This is a four-port device just like the add-drop ring filter. The splitter in this MZI is most commonly a multimode interferometer (MMI), a directional coupler, or an adiabatic splitter. For now, the assumption is to use a directional coupler. The transmission matrix and transfer functions for the 2x2 MZI are given in Equations 4.4. The couplers are assumed to be lossless such that $|\kappa_i|^2 + |t_i|^2 = 1$. As with the 1x2 MZI, the propagation loss in the arms is ignored for now.

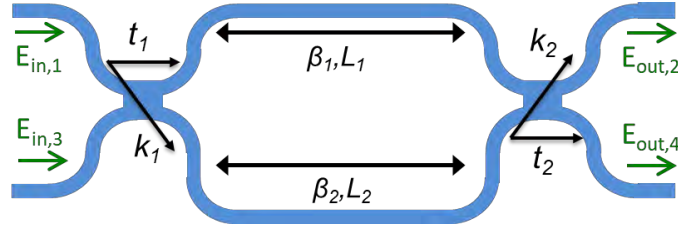


Figure 4.2: Schematic of a MZI using a pair of 2x2 splitters.

$$\begin{pmatrix} E_{out,2} \\ E_{out,4} \end{pmatrix} = \begin{pmatrix} t_2^* & \kappa_2 \\ \kappa_2^* & t_2 \end{pmatrix} \cdot \begin{pmatrix} e^{-j\beta_1 L_1} & 0 \\ 0 & e^{-j\beta_2 L_2} \end{pmatrix} \cdot \begin{pmatrix} t_1 & \kappa_1^* \\ \kappa_1 & t_1^* \end{pmatrix} \begin{pmatrix} E_{in,1} \\ E_{in,3} \end{pmatrix} \quad (4.4)$$

$$\frac{|E_{out,4}|^2}{|E_{in,1}|^2} = 4(\kappa t)^2 \cos^2\left(\frac{\Delta\varphi}{2}\right) \quad (4.5)$$

In practice, the couplers are often designed to be identical such that $\kappa = \kappa_1 = \kappa_2$. The light travelling from port 1 to 2 is known as the “bar” configuration, while going from port 1 to port 4 is known as the “cross” configuration. The power transfer functions for the cross configuration is given in Equation 4.5, if no light is input from port 3. One thing to note is that the extinction ratio of the cross port remains high no matter what the coupling ratios are, if they are the same for the two couplers. This can be intuitively understood as the light going “across” a coupler and “through” a coupler each, causing the two paths to be symmetric with respect to the couplers. For the bar port, one of the paths goes “across” two couplers, while the other goes “through” two couplers, which can lead to intensity mismatch unless the coupling ratio is 50:50, leading to reduced extinction ratio. In the case that the couplers are 50:50, which is often the goal, the transfer functions of the cross and bar ports can be simplified even further to $\cos^2\left(\frac{\Delta\varphi}{2}\right)$ and $\sin^2\left(\frac{\Delta\varphi}{2}\right)$ respectively. The extinction ratio is high for all port combinations in this case, which is ideal for the optical circulator. The FSR for the 2x2 MZI is the same as the one for the 1x2 MZI.

4.2 MZI based isolator

Design and Fabrication

The concept of using a nonreciprocal optical interferometer as an optical isolator dates back to as early as 1975 [1]. Early works almost focused exclusively on etching waveguides on GGG substrates. A brief summary of the development of these early integrated optical isolators was covered in Chapter 2, as well found in references such

as [2]. As semiconductor lasers became mainstream and PIC technology started developing, researchers such as Professor Mizumoto began exploring the use of wafer bonding to guide the light in a semiconductor waveguide and using the MO material as a cladding. These demonstrations included bonding to a GaInAsP/InP waveguide in 2000 [3] as well as silicon in 2003 [4], although a full isolator on silicon was not achieved until 2008 [5]. Over the last decade, the results of MZI based optical isolators and circulators have continued to improve in terms of isolation ratio, optical bandwidth, insertion loss, and fabrication compatibility with other PIC elements. As with the microring devices in Chapter 3, the integrated electromagnet is central to the operation of MZI isolators in this chapter. While a MZI isolator with integrated electromagnet was demonstrated as early as 1990 [6], it was not utilized in conjunction with semiconductor waveguides until now.

The schematic of the MZI isolator is shown in Figure 4.3, in which the splitter is either a 1x2 Y-splitter or a 2x2 directional coupler.

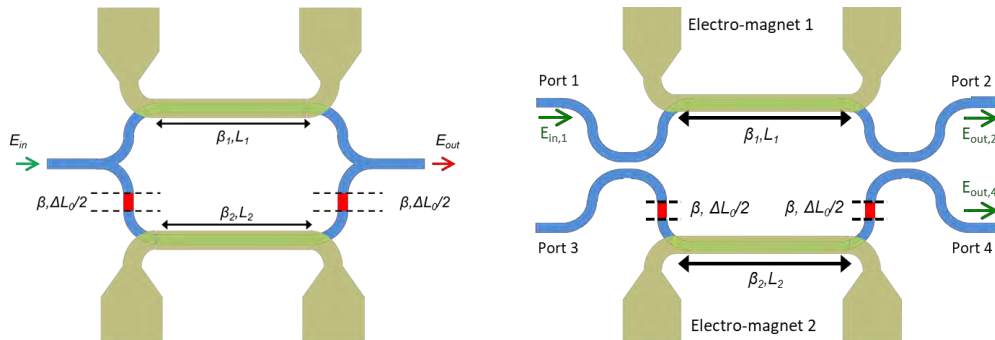


Figure 4.3: Schematic of the MZI isolator with electromagnets.

Here, L_1 and L_2 are the lengths of the two electromagnets, above the two arms, which is the extent of the interaction length between the magnetic field and the waveguide. For

the devices considered here, the two electromagnets are identical such that $L_1 = L_2 = L$. The physical path difference ΔL_0 between the two arms is split into two sections on one of the arms, as shown in Figure 4.3. all other sections of the interferometer arms such as bends are identical. The phase constant of the waveguide when there is no magnetic field applied is β , while β_1 and β_2 represent the phase constants under the influence of a magnetic field in the top and bottom arms respectively. The optical path imbalance $\Delta\varphi$ between the two arms is then defined as Equation 4.7.

$$\Delta\varphi = \beta \cdot \Delta L_0 + \beta_2 L_2 - \beta_1 L_1 \quad (4.7)$$

As discussed in Chapter 3, the current induces a magneto-optic NRPS $\Delta\varphi_{MO} = \Delta\beta L$ as well as a reciprocal phase shift due to Joule heating $\Delta\varphi_{TH}$. When the currents in the two arms are equal in magnitude but opposite in direction (analogous to push-pull operation), the phase constants of the two arms can be written as follows, where the plus or minus refer to the forward and backward directions respectively.

$$\beta_1 = \beta \mp \Delta\varphi_{MO}/2 + \Delta\varphi_{TH} \quad (4.8)$$

$$\beta_2 = \beta \pm \Delta\varphi_{MO}/2 + \Delta\varphi_{TH} \quad (4.9)$$

From these equations while the sign of $\Delta\varphi_{MO}$ changes with the current, the Joule heating is the same for the two arms under the assumptions that the currents $|I_1| = |I_2|$ are of equal magnitude and $\Delta L_0 \ll L$. The operating principle of the MZI isolator is to ensure that the two arms of the unbalanced MZI interfere constructively in the forward direction $\Delta\varphi_F = 2m\pi$, and destructively in the backwards direction $\Delta\varphi_B = 2n\pi + \pi$ for integers m and n .

$$\Delta\varphi_F = \beta \cdot \Delta L_0 + \Delta\varphi_{MO} = 2m\pi \quad (4.10)$$

$$\Delta\varphi_B = \beta \cdot \Delta L_0 - \Delta\varphi_{MO} = 2n\pi + \pi \quad (4.11)$$

For all devices considered in this work, $m = n + 1$ such that $\Delta\varphi_F - \Delta\varphi_B = \pi$. This provides the shortest MZI, which in turn reduces the footprint and insertion loss of the device. From this, $\Delta\varphi_{MO}$ must be equal to $\pi/2$, which sets a target length for the MZI arms and electromagnet. Since the waveguide cross-section (width = 600nm) is identical to that used for the microring isolator, the same simulations can be used. The RWS was experimentally determined to be 0.36nm at a driving current of 200mA and predicted to be as large as 0.55nm in absence of Joule heating, and 0.7nm if there is no bonding oxide. The RWS and $\Delta\beta$ can be related by Equation 4.12 and the required electromagnet length is reported in Table 4.1 for a wavelength of 1550nm. For the devices in this chapter, a conservative length $L = 940$ microns was selected. This allows some room for error in case the Faraday rotation or magnetic field is not as strong as the devices in Chapter 3. Furthermore, a smaller drive current can be used. However, if size (and insertion loss) is more of a concern, then smaller lengths could be chosen, assuming that the magnetic field is strong enough to saturate the Ce:YIG.

$$\Delta\beta = \Delta\lambda_{MO} \cdot \frac{2\pi n_g}{\lambda^2} \quad (4.12)$$

$\Delta\lambda_{MO}$ (ring)	$\Delta\beta$	L
0.20 nm	1.674 rad/mm	0.938 mm
0.35 nm	2.929 rad/mm	0.536 mm
0.55 nm	4.603 rad/mm	0.341 mm
0.70 nm	5.858 rad/mm	0.268 mm

Table 4.1: MZI isolator length splits.

While the reciprocal path difference ΔL_0 does not affect the NRPS, it does determine the FSR of the MZI from Equation 4.3. If the goal is to realize a broadband MZI, ΔL_0 should

be selected to be small so that the FSR is large, and the fringes are separated. On the other hand, fabrication inaccuracies make it extremely difficult to place the center of the MZI fringe at 1550nm, much like it is difficult to exactly hit a resonance wavelength in a microring. A tuning mechanism is needed, which can be achieved by slightly imbalancing the drive currents $|I_1|$ and $|I_2|$ to thermally tune the MZI fringes. This is expanded upon in the characterization section.

The integer values of m and n are tabulated in Table 4.2. The FSR and isolation bandwidth at 20dB is also calculated based on the MZI model and parameters in this chapter. Both waveguide and material dispersion is taken into account, as well as the wavelength dependence of Faraday rotation, which is shown in Figure 4.4 [7].

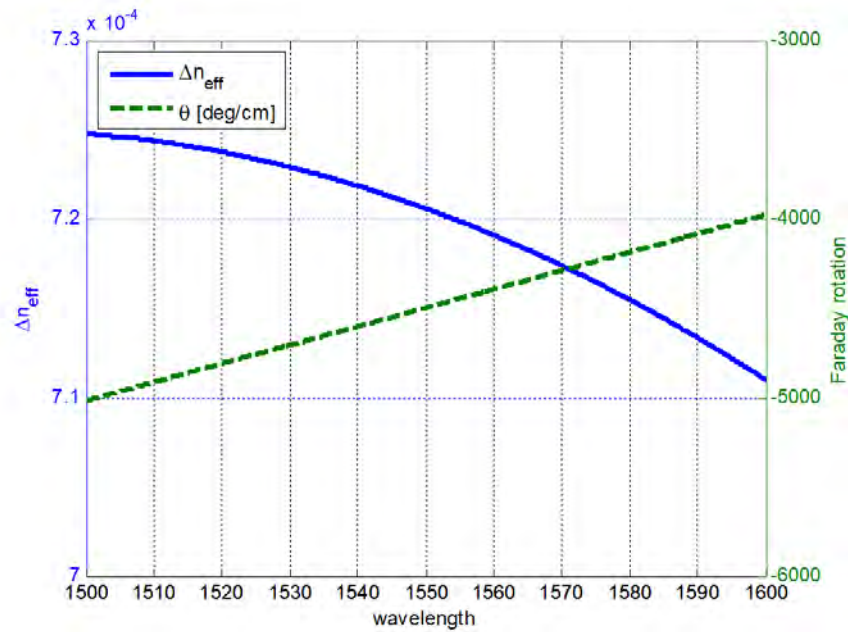


Figure 4.4: Simulated wavelength dependence on effective index and Faraday rotation. Further details on the simulations are found in [7].

M	N	ΔL	FSR	20dB Isolation BW
2	1	1.25 μm	602.8 nm	37 nm
6	5	4.09 μm	183.5 nm	11.5 nm
21	20	14.77 μm	50.8 nm	3.2 nm
201	200	142.9 μm	5.2 nm	0.3 nm

Table 4.2: MZI Isolator bandwidth splits.

Finally, the design and selection of the splitters in the MZI is crucial to the extinction ratio, and isolation ratio of the device, much like the importance of critical coupling in the microring isolator. For all devices in this work, the splitters are placed under the Ce:YIG. The reason for this is to avoid any reflections in the arms when the light enters the bonded garnet areas. Having such reflections within the interferometer is extremely problematic, as it will introduce additional interference fringes based on Fabry-Perot resonances in the spectra. Such reflections outside the interferometer will still affect the performance of the device, but not as significantly as having them inside the MZI. Ultimately, it is best to reduce the reflections as much as possible especially when integrating isolators with lasers, which is discussed in Chapter 6.

For the MZI isolator, both a 1x2 Y splitter, a 2x2 direction coupler, and a 2x2 MMI were considered. Beginning with the MMI, the simulated device performance was poor due the placement of the MMI under the Ce:YIG. There are many studies and papers on MMI design [8], and one of the crucial design aspects is reducing the reflections from the MMI. A commonly used strategy is to taper the width of the waveguide leading up to the central imaging region, but this leads to mode conversion from TM₀ to TE₁ when the waveguide cross-section is asymmetric in the vertical dimension. In fact, this mode conversion is a crucial aspect of the polarization rotator devices discussed in Chapter 5. Nevertheless, it is undesirable in an MMI as shown in Figure 4.5. The fundamental TE

mode, as simulated by the eigenmode expansion method in Lumerical MODE, has certain MMI lengths at which it produces a 50:50 splitting ratio. However, the MMI behavior as a function of length is much more chaotic for an input TM mode. In fact, the partial transition from TM₀ to TE₁ is visible in the taper leading up to the MMI. It may be possible to produce a functional MMI component for TM modes if the taper is eliminated, but due to other difficulties mentioned above, MMIs were not considered in the MZI isolator.

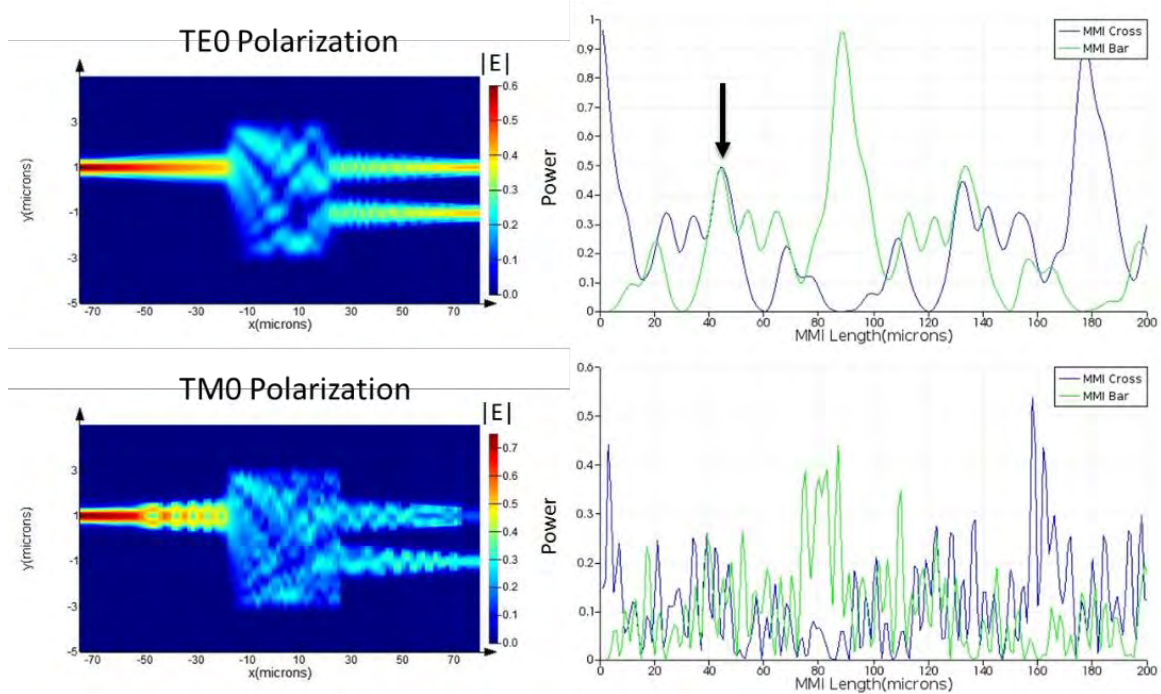


Figure 4.5: FDTD and EME simulations of the MMI with bonded Ce:YIG on top for TE and TM polarizations. A length of 42 microns is selected for the TE polarization, giving a 50:50 split, but no appropriate lengths are available for TM modes.

Directional couplers are extremely well studied devices, and their pros and cons are well known. They are used because of their simplicity and compactness. Furthermore, the backreflection from a directional coupler is generally considered to be negligible.

However, since they operate based on modal beating, there is an inherent wavelength dependence for the splitting ratio. Furthermore, directional couplers are extremely sensitive to fabrication variations, such as the coupling gap, which directly affects the beat length of the coupler. Simulations in Figure 4.6 of a directional coupler with 200nm and 300nm gap. The beat length is much shorter in the 200nm gap coupler, which is understandable given the stronger coupling coefficient.

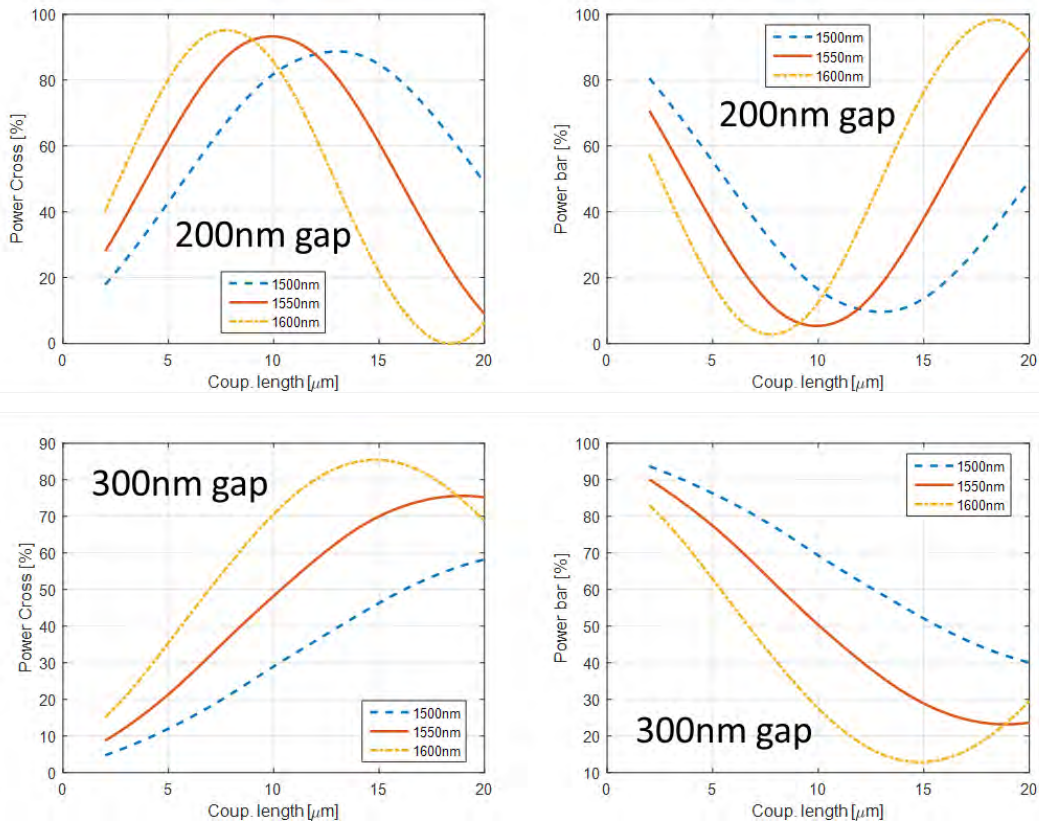


Figure 4.6: EME simulations of a directional coupler with Ce:YIG bonded on top for TM polarization for different wavelengths and coupling gaps. The cross (left) and bar (right) transfer functions are shown.

Y-splitters operate adiabatically, which should guarantee a wavelength independent 50:50 splitting ratio. However, this is often not the case, as fabrication imperfections can cause the splitting ratio to be uneven. Another common issue with Y-splitters is the

reflection that occurs at the splitting region, as well as the sensitivity to the branching angle. Therefore, a modified Y-junction is simulated based on the previous results in [9] and shown in Figure 4.7. A comparison of these couplers is shown in Figure 4.8, in which the standard Y-junction has the worst extinction ratio, as well as noticeable ripples in the spectra, caused by reflections. The directional coupler has the best performance among the three.

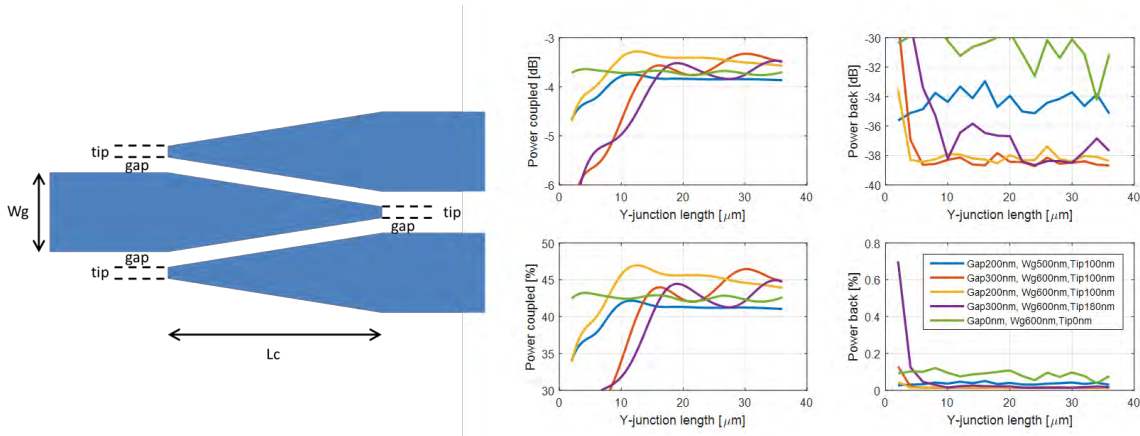


Figure 4.7: FDTD simulations for a tapered gap Y-junction with bonded Ce:YIG on top for TM polarization.

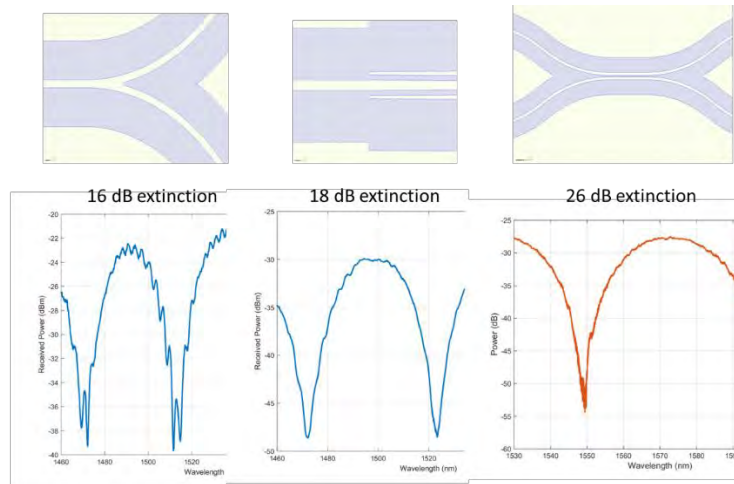


Figure 4.8: Experimental comparison of a Y-junction, a tapered Y-junction, and a directional coupler in terms of extinction ratio in a MZI with bonded Ce:YIG.

Another type of splitter, known as an adiabatic 3dB coupler, is further discussed in Section 4.3. The device was fabricated using the same process flow as the one in Chapter 3 for the microring isolators, with some minor changes. First of all, the length of the Ce:YIG die bonded to the chip was reduced from 3.5mm to 1.5mm, in an effort to reduce insertion loss. Second of all, the SGGG thickness was left at 10 microns as opposed to 5, due to some difficulties in levelling the polisher at the time of the fabrication. This results in weaker magnetic fields, as was discussed in Section 2.5, which means a stronger current is required to saturate the magnetization in the Ce:YIG. The final device schematic and microscope image are shown in Figure 4.9.

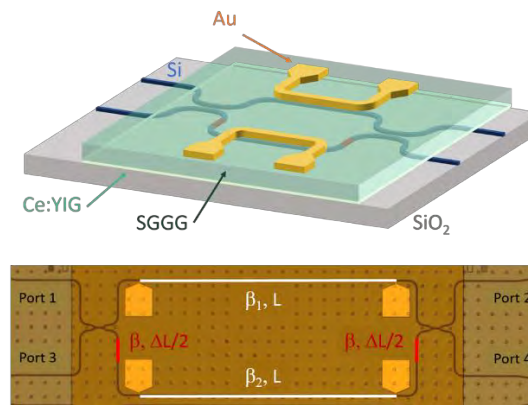


Figure 4.9: Schematic and micrograph of MZI isolator.

Device Characterization

Characterization was performed using the same procedures detailed in Chapter 3. For testing the device as an isolator, the light is injected from Port 1, and measured out of Port 4. Figure 4.10 depicts the spectrum from a narrowband device with $m=201$ and $n=200$. The devices are characterized using a tunable laser (1460nm to 1580nm), coupled into the TM mode of the device, and a power meter used to record the power.

The excess loss of the device caused by the Ce:YIG is ~ 8 dB, as normalized to a reference silicon waveguide with the same length. The origin of this loss primarily comes from propagation loss through the Ce:YIG clad silicon waveguide (~ 5 dB) as well as the transition of the waveguide into the bonded area (~ 1 dB each). From comparison to a Ce:YIG clad waveguide without the MZI, we see that the directional couplers and extra path length in the bottom arm accounts for another ~ 1 dB of loss. Shrinking the length of the interferometer (L) further could reduce the loss even further.

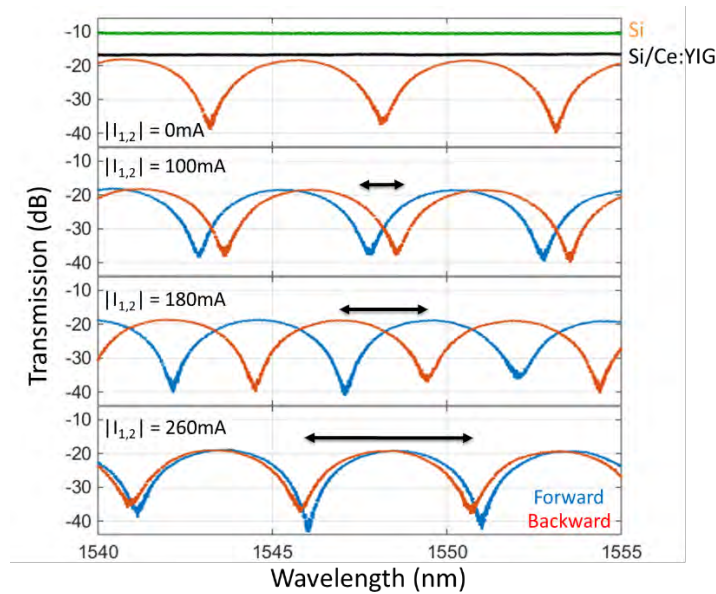


Figure 4.10: Experimental transmission spectra through the MZI isolator for different applied currents in the electromagnet.

The MZI fringes are very uniform with extinction ratio over 20dB. When no current is applied to either arm, the forward and backward spectra are aligned. As we increase the equal but opposite currents I_1 and I_2 in the electromagnets, we observe a wavelength split between the minima of the forward and backward spectra. When $|I_1| = |I_2| = 180$ mA, the minima of the backward spectra align with the maxima of the forward

spectra, which results in the maximum optical isolation. Given the 4 Ohm resistance of each microstrip, this corresponds to 130mW of power dissipated due to Joule heating per microstrip. The fringe separation as a function of current can be used to extract the phase difference between forward and backward propagation in the two arms ($2 \cdot \Delta\varphi_{MO}$). This is plotted in Figure 4.11 as a function of the drive current. For a phase difference of π for optimal optical isolation, which is obtained near 180mA. When the current is larger than 280mA, we see a roll off and saturation of the magneto-optic effect. This is because of a decrease in Faraday rotation due to Joule heating, as was also observed in our previous microring isolator devices. The Faraday rotation is also slightly weaker at longer wavelengths (1580nm vs 1460nm) as expected. This device showed a sublinear dependence between the NRPS and applied current, the reason for which may be tied to the sublinear magnetization of the Ce:YIG when it is not saturated.

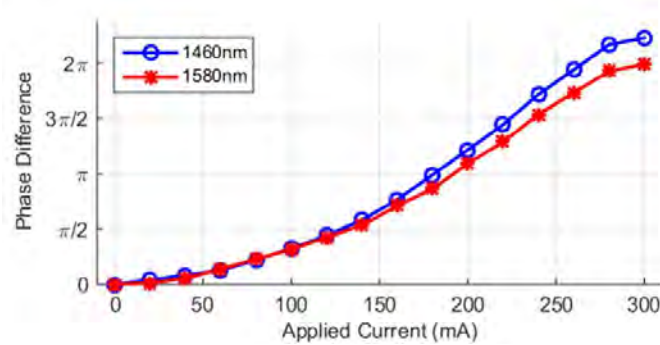


Figure 4.11: Extracted optical path difference between forward and backwards propagation in the MZI based on the data in Figure 4.10.

Improvements on substrate removal to thin the SGGG even further will decrease the current required since magnetic field strength is inversely proportional with substrate thickness. Furthermore, while the first-generation device only used a single coil electromagnet, while multicoil designs discussed in Chapter 2.5 can help reduce the

current requirement. A subsequent run with $L = 1\text{mm}$ showed significantly improved performance in terms of power requirements. The results are shown in Figure 4.12 for several different SGGG thicknesses and electromagnet designs. For the best 3-coil design, the optimum isolation criteria of the phase difference between forward and backward arms $2 \cdot \Delta\phi_{MO} = 180$ degrees is achieved with only 13mA of current, resulting in only 3.6mW of dissipated power for a 20 Ohm resistance.

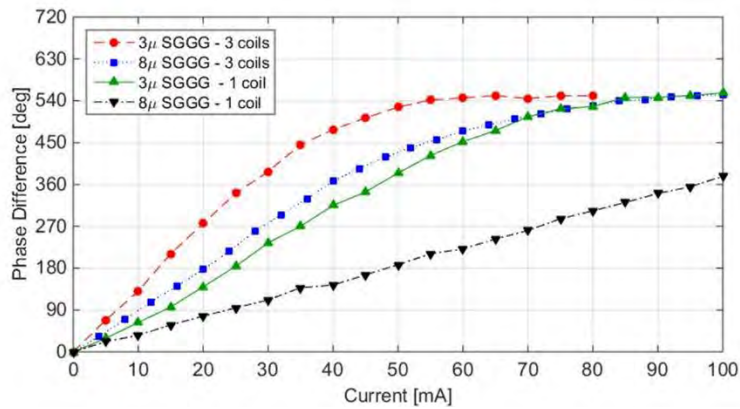


Figure 4.12: Comparison of MZI isolator with various electromagnet geometries based on data in this chapter, as well as subsequent fabrication runs, detailed in Chapter 5.

To achieve broadband isolation, ΔL_0 is reduced to 1.25 microns ($m=2, n=1$). Due to the large FSR, only a single fringe is visible. Phase errors between the two arms blueshift the minimum of the spectra near 1450nm instead of the designed 1550nm, which is outside the range of the tunable laser. It is possible redshift the spectrum by slightly unbalancing the currents I_1 and I_2 , since the electromagnets can be controlled independently. However, doing so will also cause some thermal unbalance between the arms, and $\Delta\phi_{TH}$ can no longer be ignored. Thus, the maxima of the forward spectrum are not exactly aligned with the minima of the backward spectrum. Nevertheless, as long the unbalance is not too large, optical isolation can still be observed.

The best working conditions are shown in Figure 4.13, where both the simulated and measured spectra are shown. We observe a maximum of 29dB of isolation at 1523nm, with an excess loss of ~ 9 dB compared to our reference silicon waveguide. This is slightly higher than the narrowband device and may be a result of the imperfect phase conditions due to the unbalanced current. There are some ripples in the spectra, which are caused by reflections at the bonding interface. When we sweep the current I_2 through the bottom, a longer arm from 200 to 240 mA, as shown in Figure 4.14, the central wavelength for isolation continuously shifts to longer wavelengths. If we instead increase the current through the top shorter arm, the central wavelength will blueshift. Since the FSR of this MZI is so large, small changes in phase result in large shifts in spectra. As a result, the central isolation wavelength can easily be tuned over 100nm (limited by tuning range of the laser).

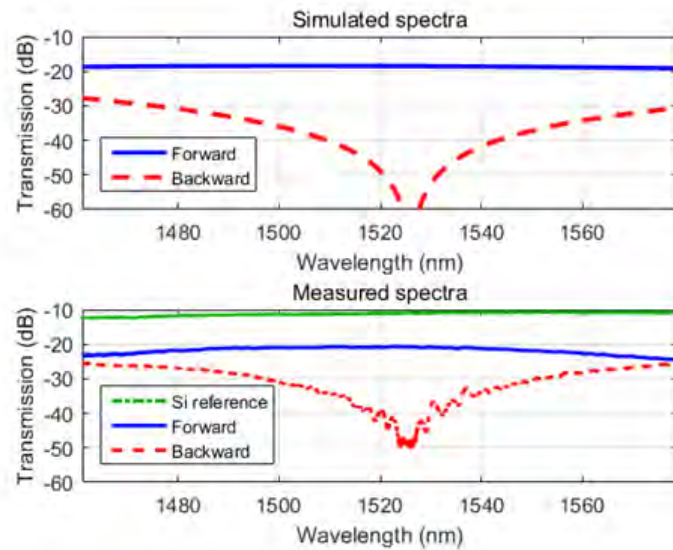


Figure 4.13: Experimental spectra of the broadband MZI isolator. Only a single fringe is visible within the tuning range of the laser.

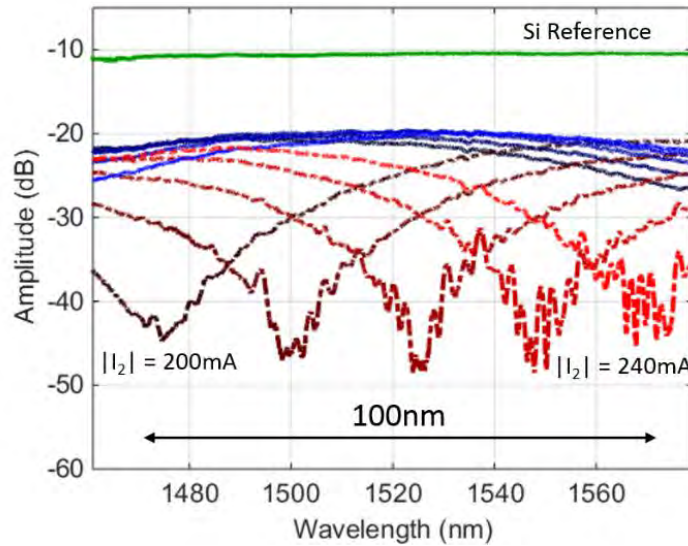


Figure 4.14: Wavelength tuning of the broadband MZI isolator by unbalancing one of the arms slightly (+/- 20mA).

Care must be taken to provide a smooth transition into the Ce:YIG clad areas to avoid these spurious reflections. One option may be to use a silicon nitride cladding ($n=2.0$) instead of silica cladding for waveguides outside the bonded region to better match the Ce:YIG ($n=2.20$) and SGGG ($n=1.97$). Another option would be to use a mode with less overlap with the top surface, such as the TE₀ or TE₁ mode, and then convert into TM₀ mode before the phase shifters. This approach is used in Chapter 5.

Finally, the isolation bandwidth of the isolator at different operating wavelengths is calculated according to Equation 3.21. The results are shown in Figure 4.15. We find that 20dB of isolation ratio is guaranteed over 14nm for the worst case (1547.87nm), and 18nm for the best case (1523.95nm). While we were unable to measure isolation bandwidth for spectra with minima near the limits of the tuning range of the laser, we expect similar performance across the whole 100nm.

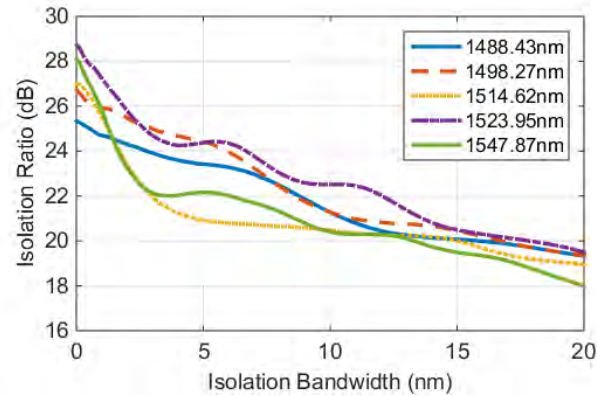


Figure 4.15: Extracted isolation bandwidth for the broadband MZI isolator.

4.3 MZI based Circulator

Since a 2x2 splitter was used, the device covered in Chapter 4.2 can be used as a circulator as well. For the device to function as a circulator, it must show high extinction ratios for both the bar and the cross configuration. However, this is generally not the case unless the directional coupler is exactly 50:50. As discussed previously, the cross-port has high extinction ratio as long as the two couplers are identical. This is not the case for the bar-port, and a comparison is shown in Figure 4.16. While the cross-port shows 15 to 20dB of extinction throughout the whole 120nm wavelength range, the bar (thru) port has much less extinction ratio, ranging from 5 to 15dB. There is also significant wavelength dependence on the extinction ratio for the bar-port, due to the wavelength dependence of the directional coupler. Directional couplers are not suitable to achieve broadband optical circulation, since the extinction ratio is inherently tied to the splitting ratio, which is wavelength dependent. Simulations in Figure 4.17 show that for 20dB of extinction (isolation), the coupling ratio must be within 5% of 50:50. This

puts extreme requirements on the design and fabrication of the coupler to be exact. To realize a broadband optical circulator, the splitters must be designed such that they are 50:50 over a large wavelength range. This can be done using an adiabatic 50:50 coupler design, which is further explored in Chapter 5.

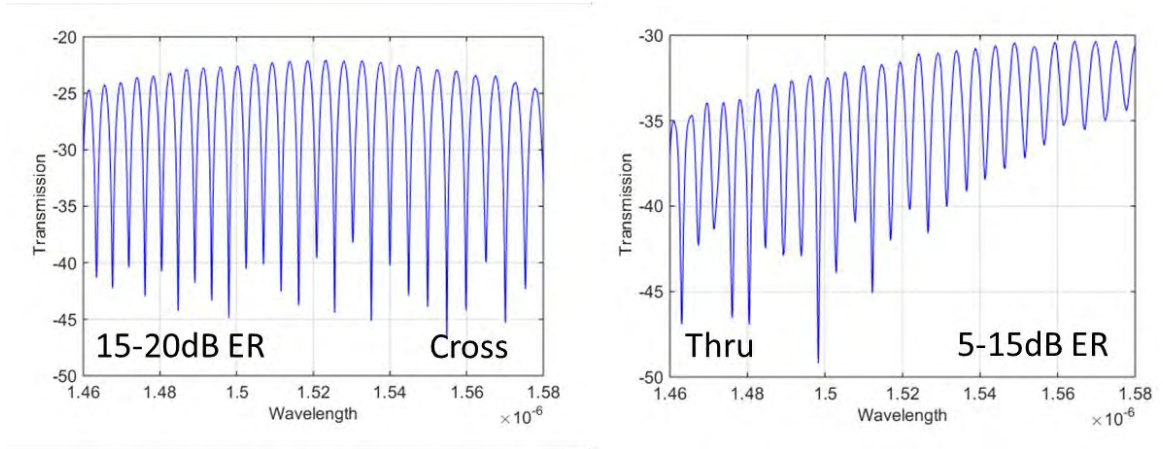


Figure 4.16: Experimental spectra of the cross and bar ports of a MZI circulator.

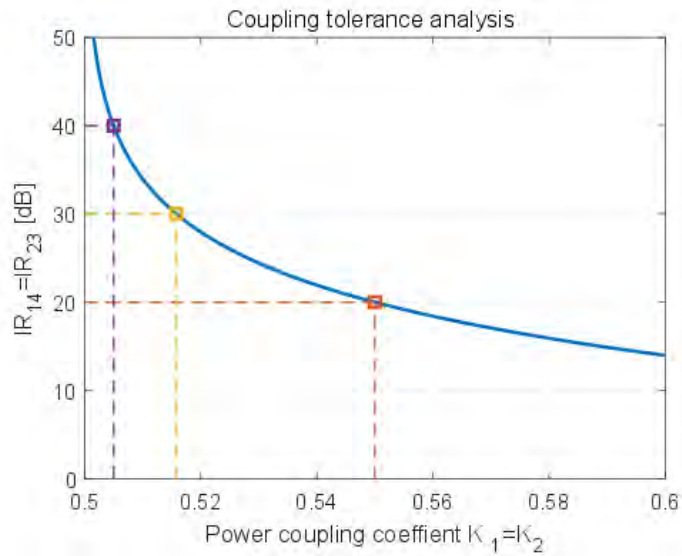


Figure 4.17: Dependence on the extinction ratio versus power coupling.

Summary

MZI isolators were demonstrated with high performance, up to 29dB of isolation. The wideband MZI design results in broad optical isolation of more than 20dB over a record 14nm. This is achieved by using the electromagnets to fine tune the magnetic fields over the two arms to center the MZI fringe in the wavelength range of interest. This can be done to tune the operating wavelength over a measured 100nm. Push-pull operation of the electromagnets on the two arms is utilized in combination with multi-coil electromagnet geometries to decrease the power consumption from an initial 260mW to 3.6mW. While the same design can be used to realize a MZI optical circulator, the coupling ratio must be guaranteed to be 50:50 over large wavelengths to achieve a broadband device. For this, directional couplers are not optimal, and other splitters should be considered.

Narrowband MZI-Isolator (TM-mode)	Value
Common Arm Length	940 microns
Arm Imbalance	142.9 microns
Designed FSR	5.2nm
Power Consumption	260mW @ 180mA
Isolation Ratio	20dB
20dB Isolation Bandwidth	0.3nm
Insertion Loss	8dB

Broadband MZI-Isolator (TM-mode)	Value
Common Arm Length	940 microns
Arm Imbalance	1.25 microns
Designed FSR	602.8nm
Power Consumption	260mW @ 180mA
Isolation Ratio	29dB
20dB Isolation Bandwidth	18nm
Insertion Loss	9dB

References

1. F. Auracher and H. H. Witte, "A new design for an integrated optical isolator," *Opt. Commun.* **13**, 435–438 (1975).
2. B. J. H. Stadler and T. Mizumoto, "Integrated magneto-optical materials and isolators: A review," *IEEE Photonics J.* **6**, 1–15 (2014).
3. H. Yokoi, T. Mizumoto, N. Shinjo, N. Futakuchi, and Y. Nakano, "Demonstration of an optical isolator with a semiconductor guiding layer that was obtained by use of a nonreciprocal phase shift," *Appl. Opt.* **39**, 6158–6164 (2000).
4. H. Yokoi, T. Mizumoto, and Y. Shoji, "Optical nonreciprocal devices with a silicon guiding layer fabricated by wafer bonding," *Appl. Opt.* **42**, (2003).
5. Y. Shoji, T. Mizumoto, H. Yokoi, I. W. Hsieh, and R. M. Osgood, "Magneto-optical isolator with silicon waveguides fabricated by direct bonding," *Appl. Phys. Lett.* **92**, 90–93 (2008).
6. T. Mizumoto, H. Chihara, N. Toku, and Y. Naito, "Verification of waveguide-type optical circulator operation," *Electron. Lett.* **26**, 199–200 (1990).

7. Y. Shoji and T. Mizumoto, "Wideband design of nonreciprocal phase shift magneto-optical isolators using phase adjustment in Mach-Zehnder interferometers," *Appl. Opt.* **45**, 7144 (2006).
8. D. J. Thomson, Y. Hu, G. T. Reed, and J. M. Fedeli, "Low loss MMI couplers for high performance MZI modulators," *IEEE Photonics Technol. Lett.* **22**, 1485–1487 (2010).
9. Y. A. N. G. W. Ang, S. H. G. Ao, K. E. W. Ang, Y. Wang, S. Gao, K. Wang, and E. Skafidas, "Ultra-broadband and low-loss 3 dB optical power splitter based on adiabatic tapered silicon waveguides," *Opt. Lett.* **41**, 2–5 (2016).

Chapter 5

Optical isolation for TE polarization

All the devices described so far have operated for the TM polarization of light. This is due to the nonreciprocal phase shift being optimized for TM modes, when considering the heterogeneous approach of adding MO material to silicon. However, semiconductor lasers typically emit in TE polarization, which limits the compatibility of the isolator with the laser. In this chapter, we explore the possibility to achieve NRPS for TE polarizations. We also look at the use of a polarization rotator, which can be placed in between the laser and the isolator (circulator). Results for both approaches are shown, and the first optical circulator on silicon for TE polarization is realized [1].

5.1 Nonreciprocal phase shift for TE polarization

In Chapter 2, the origin of the NRPS effect in magneto-optic waveguides was discussed, and the polarization dependence of NRPS was introduced. The wafer bonding approach used for the devices in Chapters 3 and 4 is not suitable to achieve NRPS for TE mode. Another approach must be taken to realize optical isolators and circulators intrinsically operating for TE polarized light using NRPS effects. One early work uses a garnet rib waveguide on GGG substrate in which a domain wall or compensation wall is

introduced in the center of the waveguide [2]. This can produce a waveguide in which the halves are magnetized with opposite signs. Thus, the symmetry of the waveguide in the x-direction is broken, and can be used to achieve NRPS [3,4]. More recently, researchers have proposed [5,6] and experimentally demonstrated NRPS for TE mode by depositing another material such as amorphous silicon side by side with a garnet waveguide [7]. Both approaches are depicted in Figure 5.1. The downside to all these approaches is compatibility with other photonic devices, since they all make use of lattice matched GGG substrates. Silicon substrates and waveguides should be used to integrate the isolators and circulators further and increase their applications.



Figure 5.1: Schematic for waveguide designs to achieve NRPS for TE modes

If silicon substrates are to be used, a monolithic approach must be pursued to deposit garnet on the silicon. Significant efforts have been made in exploring such a monolithic approach towards integrating magneto-optic material onto silicon and silicon nitride waveguides by several research groups across the world including MIT [8–13] and the University of Minnesota [14–17]. We explored such approach through collaborations with these groups, in an effort to realize a monolithic optical isolator operating for TE modes.

The basic design was shown in Chapter 2 and consists of a silicon waveguide with a magneto-optic cladding on the side. The waveguide must be asymmetric, so the MO material must only coat one side of the waveguide. One way to do this is to fully clad the waveguide, etch a trench in the cladding on the side of the waveguide, and deposit the MO material everywhere. This procedure is depicted below in Figure 5.2, and the simulations are shown in Figure 5.3 for a silicon height of 220nm. Since the refractive index silicon exceeds that of Ce:YIG, the mode remains confined in the silicon core, even when the width of the Ce:YIG is much larger. However, the silicon should not be too skinny, as it complicates the fabrication and lithography. A silicon width of 350nm or 450nm was chosen, and up to 0.35nm of RWS is expected, assuming a Faraday rotation of -4500 deg/cm. If the Faraday rotation is weaker, as is often the case with the deposited garnets, then this RWS will decrease accordingly. MZI structures were also designed with various splits on the length of the MO section. This can be a clearer indication of whether any nonreciprocal phase shift was achieved.

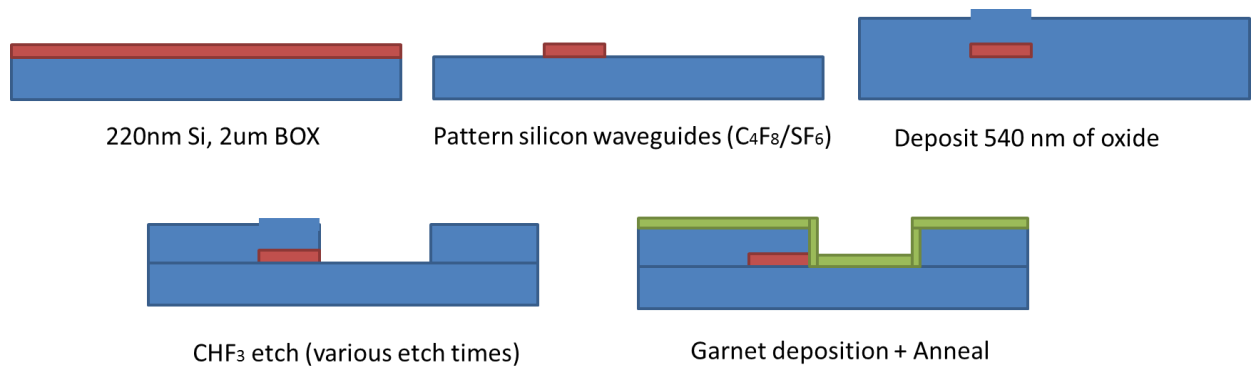


Figure 5.2: Process flow for preparing MO isolators for TE polarization

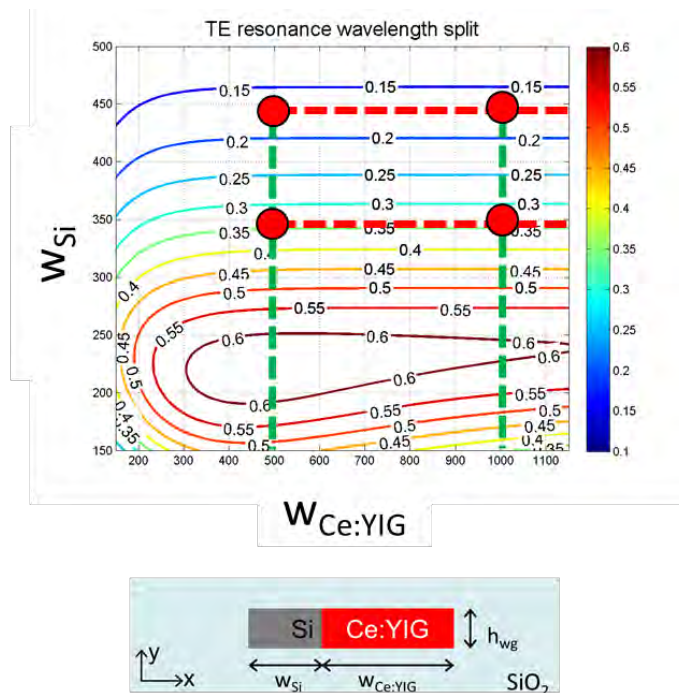


Figure 5.3: Simulation of the RWS for different silicon and Ce:YIG widths.

Both microring and MZI based devices were fabricated following these simulation parameters, and SEM images are shown in Figure 5.4 both prior and after garnet deposition and RTA. In this particular example, a Bi:YIG thin film was deposited by collaborators at MIT using a YIG seed layer to promote crystallization. The method of deposition was pulsed laser deposition. There is clearly some incident angle during the deposition, as the sidewall coverage on one side is much greater than the other. A rapid thermal anneal was performed (generally > 800C) to crystallize the garnet into the correct phases.

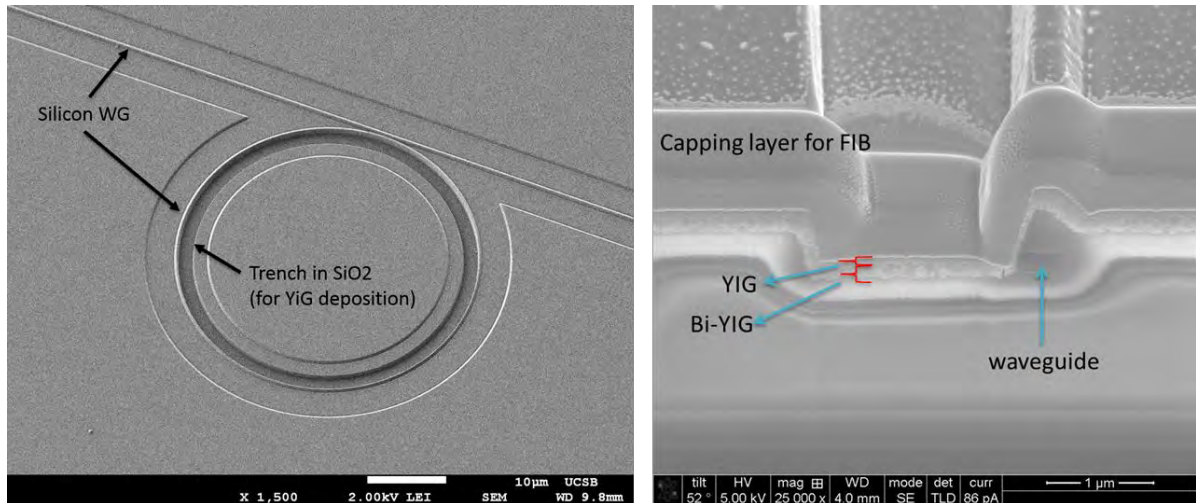


Figure 5.4: SEM images of the waveguides with the trench adjacent to the waveguide, and the cross-section after garnet deposition.

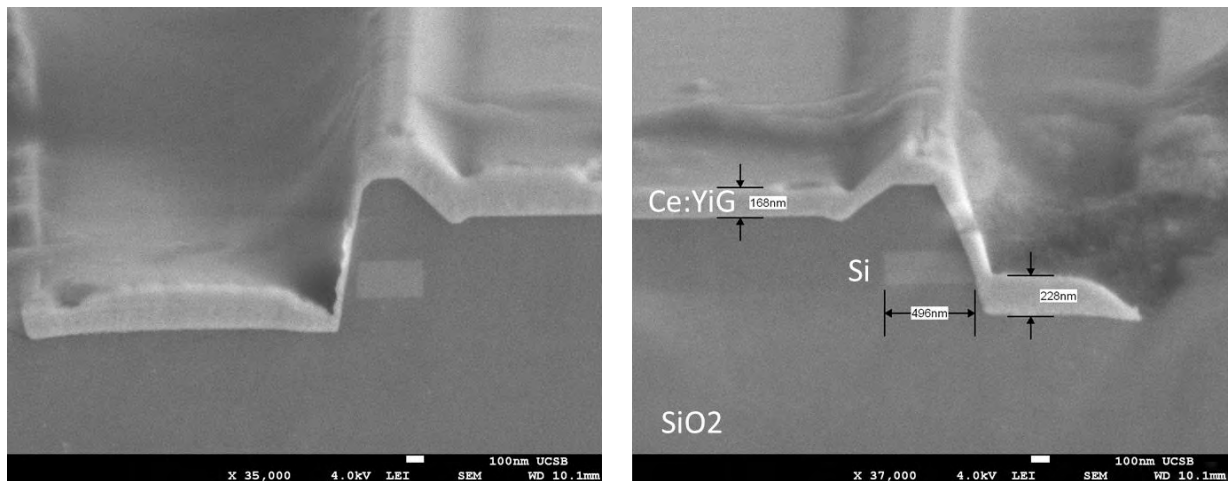


Figure 5.5: SEM images of the occasional misalignment in the trench.

Several complications arose during the fabrication of these devices. The alignment of the oxide trench and the waveguide becomes crucial, as misalignment as shown in Figure 5.5 can cause an oxide layer to form between the silicon and the Ce:YIG. It was already established in Chapter 3 that the presence of this oxide layer greatly reduces the NRPS. The other concern is that the trench etch does not stop at the bottom of the

waveguide but goes into the buried oxide. This causes an offset in the heights of the silicon and Ce:YIG waveguide sections. To get around this, it is possible to overetch the trench, and then rely on sidewall coating of the garnet onto the waveguide.

However, this also has its drawbacks. First of all, the sidewall coverage is much poorer than a blanket deposition, and the garnet thicknesses on the sidewall are only half of what is on top of the wafer, or even less. Growths of films exceeding 400nm resulted in cracking due to thermal expansion mismatch during the rapid thermal anneal. Thus, it is not possible to achieve a thick sidewall coating using conventional deposition methods without rotation of the sample. Second of all, Since the sidewall coating is affected by the angle, it causes a non-uniform waveguide cross-section in the ring resonator. This can be compensated by designing a racetrack resonator or using a MZI instead. Finally, it is unclear what the quality of the garnet is when it is on a sidewall.

Despite these issues, the SEM images of the cross-section show that the MO material is side by side with the silicon waveguide. The samples were diced and polished for testing.

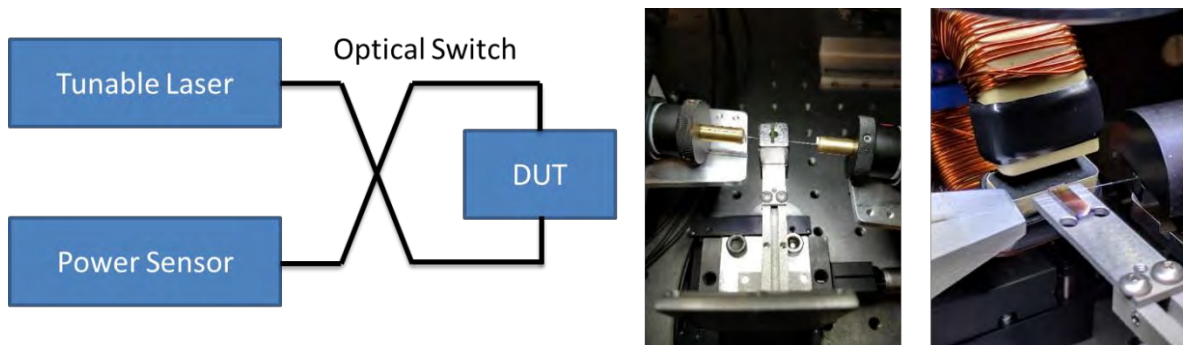


Figure 5.6: Schematic and images of the test setup for generating strong out-of-plane magnetic fields.

The devices were initially sandwiched between a toroidal electromagnet capable of generating $>0.1\text{T}$ of magnetic field. Later on, the setup was changed such that the sample sits directly on a neodymium magnet with a measured field strength of 0.5T at the surface. In both cases, the magnetic field is generated out-of-plane with respect to the chip. An optical switch is used to change the propagation direction of light, and the spectra is recorded in both forward and backward directions.

Ultimately, no discernable NRPS was found in the samples. This holds true over multiple device designs, fabrication runs, and deposition techniques. Different garnets were experimented such as Ce:YIG, Bi:YIG, Ce:TIG, and Bi:TIG with varying thicknesses, deposition parameters, and anneal temperatures. Neither microring or MZI devices showed any appreciable nonreciprocity for magnetic fields up to 50000Oe , which is well above the saturation point of the garnets. Two example spectra are shown below in Figure 5.7 for a ring resonator and MZI respectively. There is no change between the spectra in the forward and backward direction.

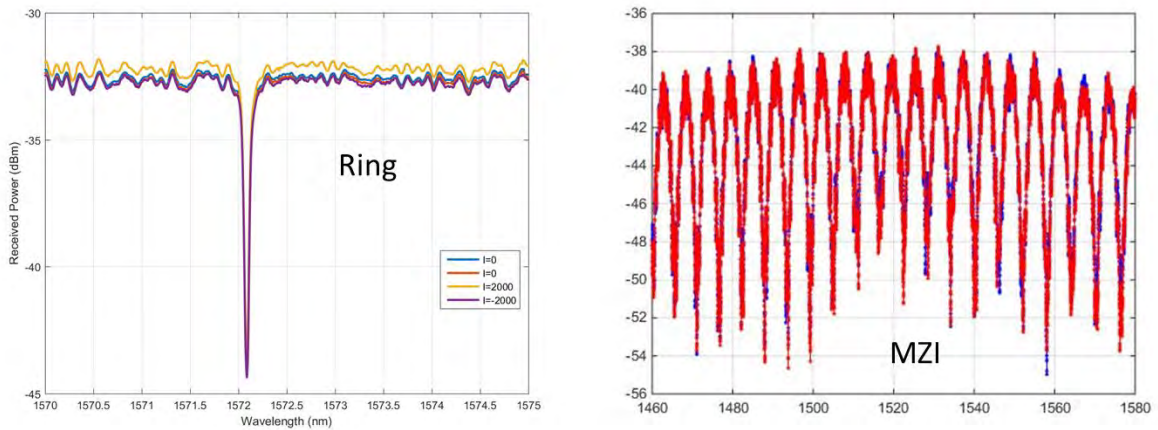


Figure 5.7: Comparison of the forward and backward spectra in the ring and MZI devices, showing no signs of nonreciprocity. Multiple sweeps showed the forward and backwards spectra to overlay exactly on top of each other.

Further analysis of devices showed that waveguides with smaller silicon cross-sections and larger overlap with the MO regions had higher loss, indicating significant penetration of the optical field into the MO material. The spectra were also clean, indicating only a single TE mode circulating in the ring or propagating through the interferometer. The resolution of the measurement is 0.1pm, which should be able to detect NRPS, even if it is much weaker than designed. Thus, the most likely conclusion is that the material itself is not magnetized. While measurements done on planar, uniform films deposited at the same time as the devices showed significant Faraday rotation, there is no actual NRPS in the devices that were measured at UCSB.

Other collaborators had more success using a similar approach. NRPS for TE polarization was observed in both silicon and silicon nitride based waveguides with Ce:YIG cladding on the side [18]. Up to 30dB of optical isolation for the TE polarization was measured. The question of material quality still remains however. The measured NRPS was only 0.36 radians per millimeter at room temperature, which is far less than the 6 radians per millimeter for TM polarization demonstrated in Chapter 3. There is significant room for improvement, but it does validate this approach, and could be promising in the future.

5.2 TE to TM polarization rotators

In the absence of a strong NRPS effect for TE mode, it is instead possible to achieve isolation for TE mode of light using a TE to TM polarization rotator. Such a rotator could be placed in between the laser and the TM mode isolator provided that the rotator has low loss, high polarization extinction ratio (PER), and low reflection. This effectively

changes to operating polarization of the isolator to TE mode, with the caveat that the PER is comparable to the isolation. Polarization rotators for silicon photonics have been widely studied and can be designed using a variety of methodologies. An excellent review of such technologies is presented in [19] and a detailed assessment of these techniques is beyond the scope of this work.

One type of polarization rotator known as the polarization splitter rotator (PSR) is attractive due to its fabrication simplicity and tolerance to fabrication errors [20]. The PSR can be separated into two components. The first section is a hybridization section, which can provide the conversion between TM and higher order TE modes through a process called mode hybridization. This effect can be readily observed in waveguides with high index contrast and asymmetrical cross-sections. For these waveguides, the amount of the dominant (i.e. E_x for TE modes) and nondominant (i.e. E_y for TE modes) field components can be comparable. The ratio between the polarizations can be written as the following equation [21].

$$\gamma_x = \frac{\int |E_x^2| dx dy}{\int |E_x^2| dx dy + \int |E_y^2| dx dy} \quad (5.1)$$

This modal hybridization is maximized when $\gamma_x = 50\%$, at which there is a crossover between the dominant polarization of the mode. To achieve significant modal hybridization, asymmetry is required in the waveguide geometry. It is possible to introduce asymmetry in the lateral direction by using L-shaped waveguides [22] or intentionally creating a slant in one of the sidewalls [23], but these typically involve additional processing steps. Instead, the easiest way to introduce asymmetry is in the vertical direction, by using a different material for the top and bottom cladding of the

waveguide. Since the bottom cladding for silicon waveguides is generally silicon dioxide, the top cladding should be a material such as air, silicon nitride, or Ce:YIG in this case, as the garnet is already bonded in order to make an isolator.

For such waveguides with vertical asymmetry, γ_x is sensitive to the width of the waveguide, which can be lithographically controlled. In Figure 5.8, a silicon waveguide with bonded Ce:YIG top cladding is shown, and the calculated effective indices of the waveguide eigenmodes are plotted. The waveguide cross-section is identical to the one used in the isolators and circulators, which alleviates some fabrication complexity. The plots are repeated for silicon heights of 220nm, 250nm, and 270nm at a wavelength of 1550nm.

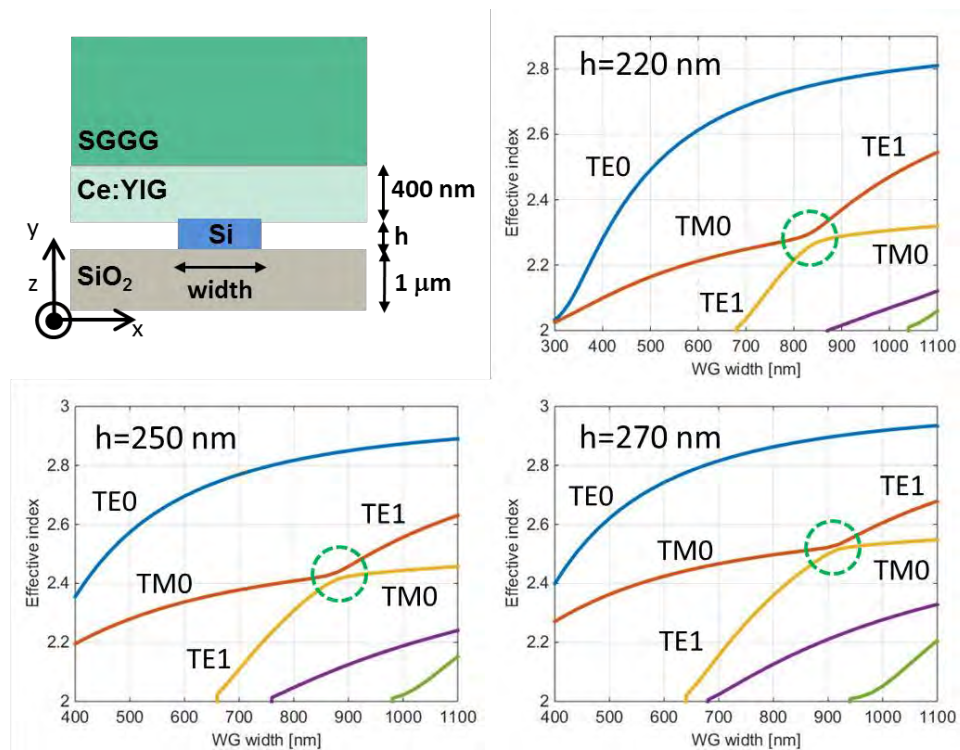


Figure 5.8: Schematic and simulations of the mode hybridization between TM0 and TE1 modes at various waveguide heights from 400nm to 1100nm and widths from 220nm to 270nm.

For each of these plots, there clearly exists a waveguide width at which the TE₀ and TE₁ modes become hybridized. The exact width at which this crossover occurs changes with the waveguide height, and the strength of the hybridization is also apparent from the “splitting” of the curves near this point. A larger split between the TE₀ and TE₁ curves, as is the case for $h = 220\text{nm}$, is indicative of stronger hybridization. When the waveguide structure is fully symmetric, the curves do not split, and instead cross each other. Hybridization between even higher order modes exist but are not shown here. The fundamental TE₀ mode is not hybridized at all, as it is far away from any mode crossings for the widths of interest. To fully take advantage of mode hybridization for polarization conversion, a taper can be utilized to adiabatically transition between the TE₁ and TM₀ modes. Such a taper should be centered around the widths circled in Figure 5.8. For the case of $h = 220\text{nm}$, the taper should be centered at a waveguide width of 840nm, at which point the mode crossing occurs. This is further verified by plotting the polarization ratio γ_x of the two selected eigenmodes as a function of the width, as shown in Figure 5.9, in which we see $\gamma_x = 50\%$ at $w = 840\text{nm}$. As with any adiabatic mode transition, the input mode with the lower (higher) effective index will transition into the mode with the lower (higher) effective index after the taper, completing the TM₀ to TE₁ transition.

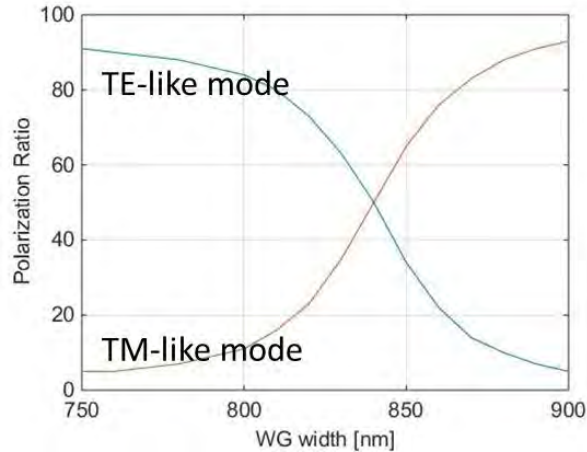


Figure 5.9: Polarization ratio of the TE and TM-like modes near the crossover point at 840nm.

As previously discussed in Chapter 4.3, the length criteria for adiabaticity can be challenging to directly calculate, and more practical to simulate. The tapering of the width should be slowest around the crossover point, so it is advantageous to use a three-section taper, in which the middle section is centered at $w = 840\text{nm}$ and tapered the slowest. This helps keep the overall length of the taper relatively short to avoid excessive losses. The final taper design is shown below in Figure 5.10 and the waveguide dimensions are tabulated in Table 5. The central part is a linear taper from 790nm to 890nm. The electric field intensity of the eigenmode is also pictured above the beginning, middle, and end of the taper. The transition between TE₁ mode to TM₀ is clear, and the hybrid TE/TM mode is also depicted at the width of 840nm.

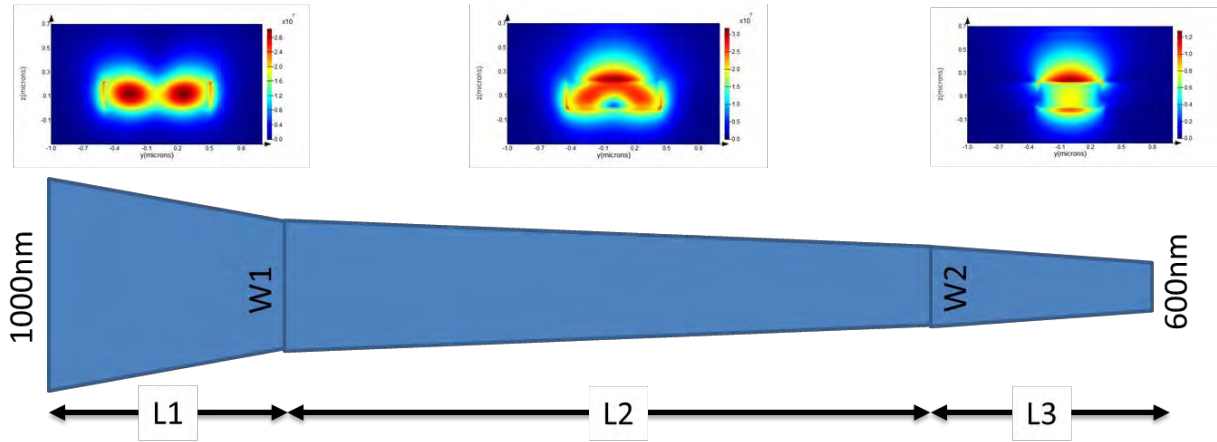


Figure 5.10: Schematic and field profiles along various points in the taper from TE1 to TM0 polarization.

Symbol	Description	Size
W1	Taper Start	890 nm
W2	Taper End	790 nm
L1	First segment length	20 μm
L2	Central taper length	80 μm
L3	Last segment length	20 μm

Table 5.1: Dimensions of the final mode hybridization taper design.

Based on EME simulations in Lumerical MODE, 50 microns is enough for complete power transfer ($\sim 99\%$) between the TM0 and TE1 modes, as shown in Figure 5.11. The final choice of the 80 microns long taper length may be overly cautious but used in anticipation of fabrication inaccuracies.

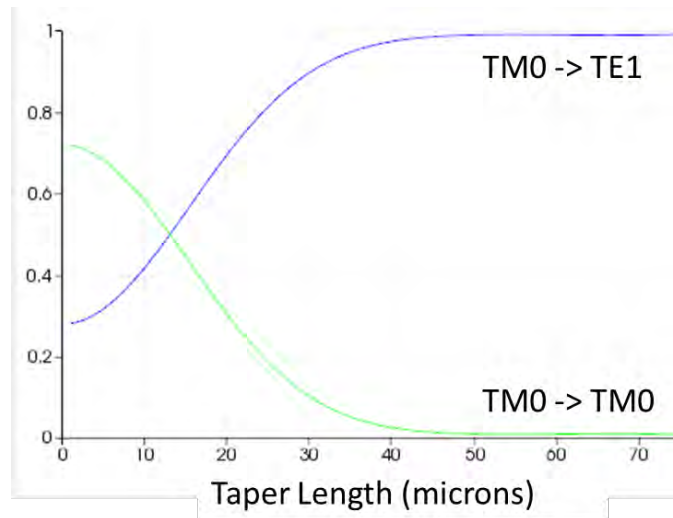


Figure 5.11: Simulation of power transfer between TM0 and TE1 modes as a function of central taper length.

The second component of the PSR is a mode converter that couples the TE0 and TE1 modes together. This is a common component in mode-multiplexed systems [24] and can be achieved using asymmetric directional couplers [20], multimode interferometers (MMIs) [25], or an adiabatically tapered coupler [26]. There are tradeoffs between size, insertion loss, and operating bandwidth when considering these structures. Ultimately, an adiabatic tapered coupler was selected, which has been shown to have better fabrication tolerance and broadband optical behavior [27].

The coupler consists of two waveguides with different widths that are gradually tapered together, but in opposite directions. The concept of the adiabatic TE0 to TE1 tapered coupler is like the adiabatic 50:50 tapered coupler in Section 4.3. Only one supermode of the two-waveguide system is excited at the input due to the mismatch in effective indices between the two waveguide modes. As the two waveguides are tapered together, there exists a point where the index between the TE0 mode of the narrow

waveguide is matched to the TE1 mode of the wide waveguide. Following this point in the taper, the supermode completely transfers its energy from the narrow to the wide waveguide. There is no beating of energy between the two waveguides like a directional coupler, since only a single supermode exists at any given point. The waveguides here have SiO₂ top cladding instead of Ce:YIG, as it is disadvantageous to have any TE/TM mode hybridization. The effective indices of TE₀ and TE₁ modes in a 220nm tall silicon waveguide on BOX is plotted for different widths in Figure 5.12. The shaded region from $n = 2.1$ to $n = 2.3$ is where the index matching is selected to occur. No other modes, TE or TM, are present near these index values for the widths considered. This is important to reduce any crosstalk between modes due to fabrication imperfections (roughness, width deviations, etc).

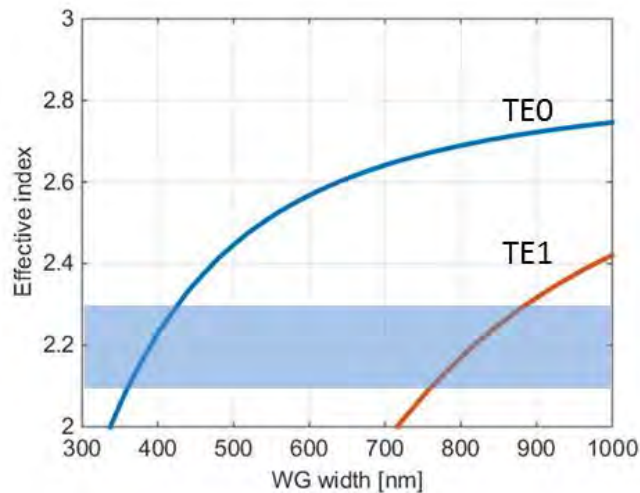


Figure 5.12: Simulation of the TE₀ and TE₁ modes for various waveguide widths for a silicon waveguide height of 220nm.

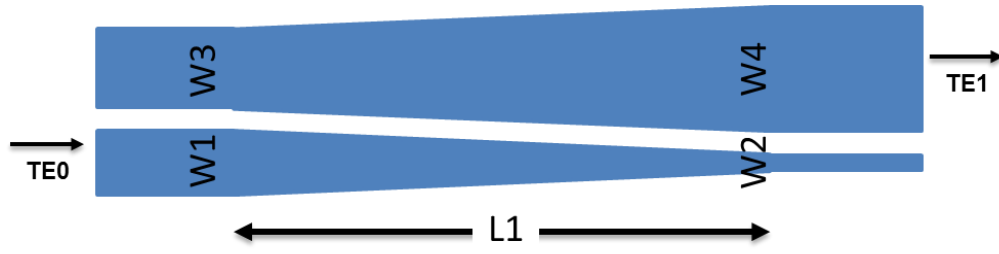


Figure 5.13: Schematic of the TE0 to TE1 tapered coupler.

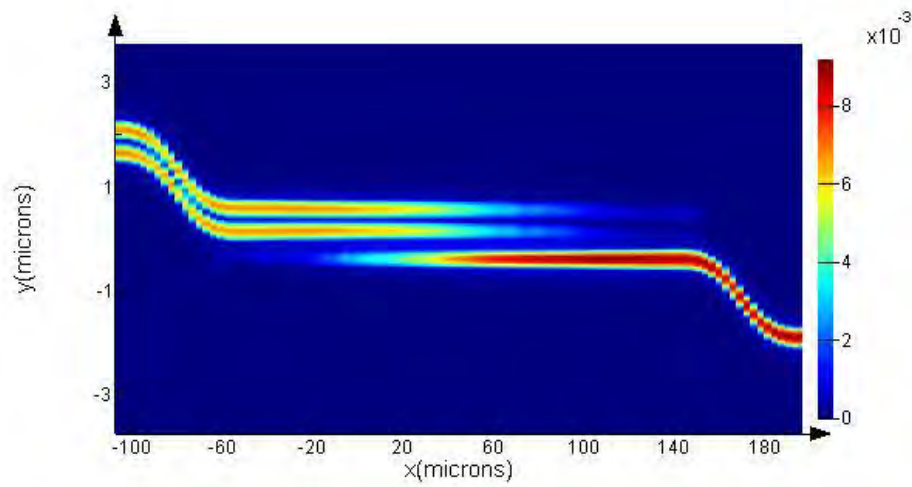


Figure 5.14: FDTD simulation of the TE0 to TE1 tapered coupler.

Symbol	Description	Size
W1	TE0 waveguide width start	440 nm
W2	TE0 waveguide width end	360 nm
W3	TE1 waveguide width start	800 nm
W4	TE1 waveguide width end	880 nm
L1	Tapered coupler length	100 μm
Gap	Gap between waveguides	300 nm

Table 5.2: Final design parameters for the TE0 to TE1 tapered coupler.

The final design of the PSR is shown in Figure 5.15. It consists of an adiabatically tapered coupler (100 μm long) for TE0 to TE1 mode conversion, followed by a linear taper (120 μm long) to convert from TE1 to TM0. S-bends and other tapers to transition

between the regions are not shown, but very important to simulate and verify. The S-bend into each adiabatic section is extremely important, as it should be gradual enough to only excite a single supermode of the system. EME and FDTD are both equally valuable tools for design and verification for such a complex structure.

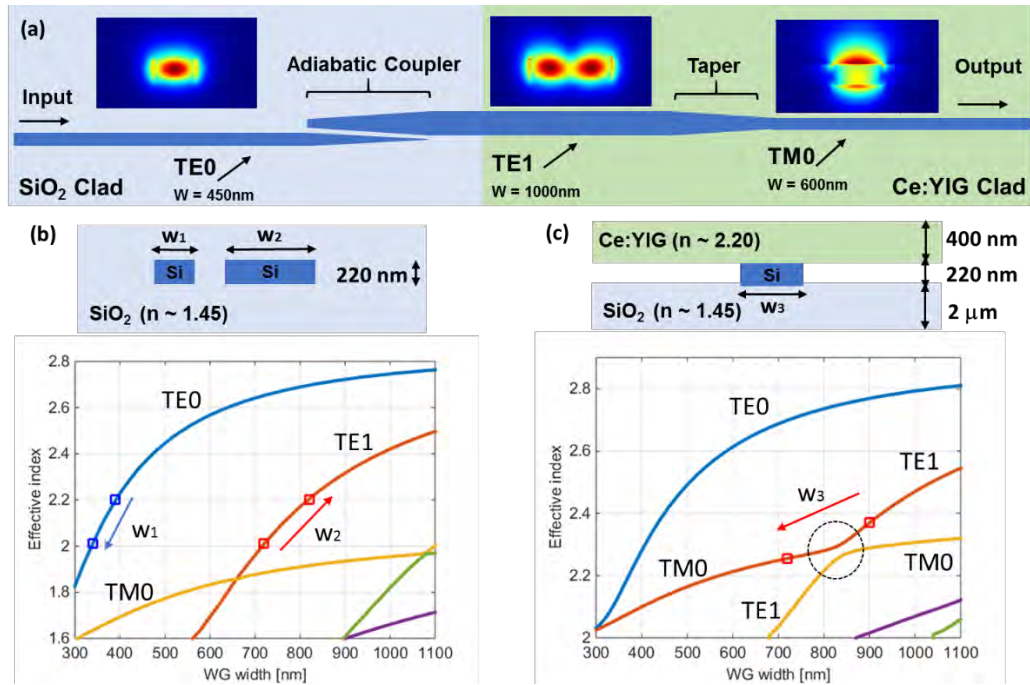


Figure 5.15: Final design of the polarization converter.

The advantage of this polarization rotator over previous TM mode isolator plus TE/TM rotator devices is improved fabrication tolerance [28] as it does not require electron-beam lithography, and fabrication simplicity [29] since it does not require any additional processing steps such as a polysilicon or silicon nitride overlay on the waveguide. The use of Ce:YIG to assist with polarization rotation is unconventional, but suitable given the constraints of the situation.

The polarization rotator is characterized by using a setup similar to the one in Chapter 3. Polarized light (TE or TM) is launched and collected using PM lensed fiber. A

polarization beam splitter is then placed at the output, and the PER can be measured by comparing the powers in the two polarizations. The test structures consisted of a polarization rotator connected with a roughly 2mm long straight waveguide segment. The results are plotted in Figure 5.16. Comparison is made with silicon only waveguides, as well as a Ce:YIG/Si waveguide with no polarization rotator. The extracted parameters are shown in Table 5.3.

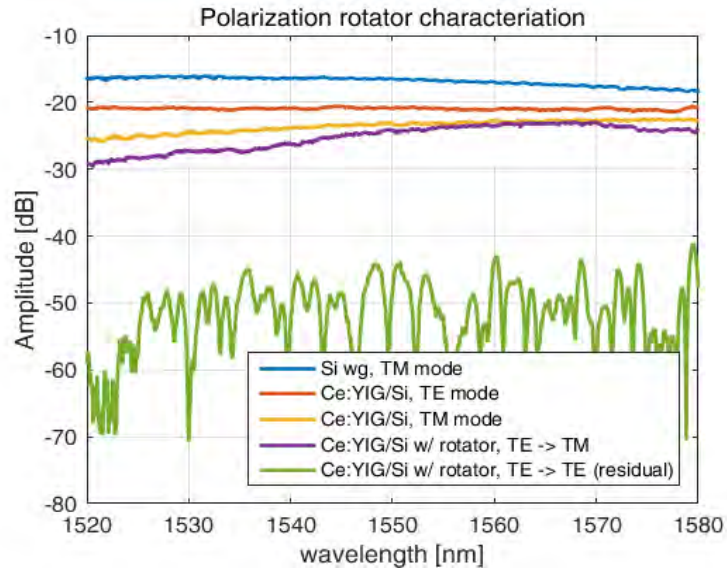


Figure 5.16: Measurements of a waveguide with and without the polarization rotator.

Symbol	Description	Size
W1	Taper Start	890 nm
W2	Taper End	790 nm
L1	First segment length	20 μm
L2	Central taper length	80 μm
L3	Last segment length	20 μm

Table 5.3:

5.3 Microring optical isolator for TE mode

Using the polarization rotator discussed in the previous section, it is possible to combine the device with the TM mode microring isolator to achieve optical isolation for TE polarized light. This is the first microring based isolator operating for TE mode. A schematic and microscope image of the isolator is shown in Figure 5, in which a 3-coil Archimedean spiral is used for the electromagnet. For this device, only a single TE to TM polarization rotator was included, and the output light polarization is TM. If the device is to be included in a PIC, it may be necessary to include a second TM to TE polarization rotator at the output of the isolator to return to the conventional TE mode.

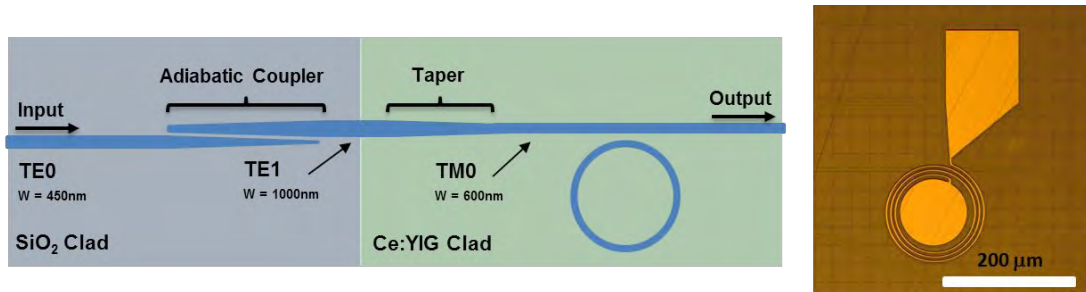


Figure 5.17: Schematic and image of the TE mode microring isolator.

The transmission spectrum is measured with a tunable laser sweep and shown in Fig. 5b. The isolation ratio is measured by injecting TE polarized light into the device while sweeping the current applied to the electromagnet. A split in the resonant wavelength between forward and backward propagation is observed for 40 mA of current, which results in a maximum of 25 dB optical isolation as shown in Figure 5.

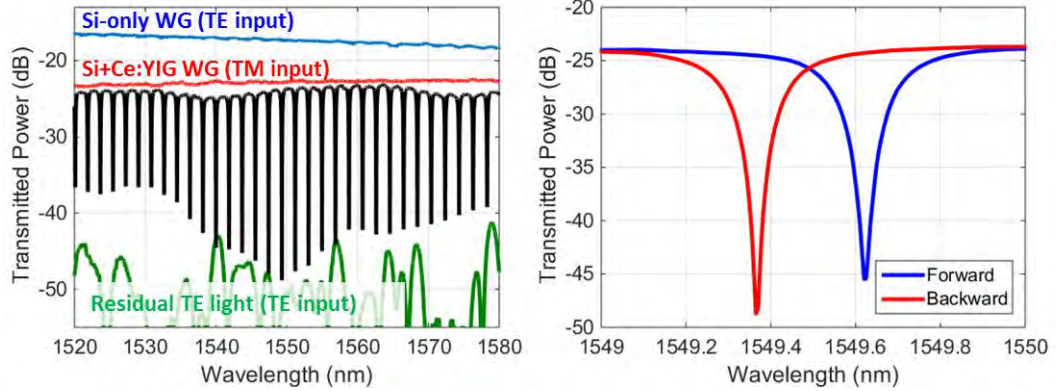


Figure 5.18: Experimental measurements of the forward and backward transmission through the TE mode microring isolator.

The performance of the polarization rotator is characterized by comparing the spectrum through the ring isolator plus rotator (TE input) with the spectrum through a reference Si/Ce:YIG waveguide (TM input) of the same geometry. The polarization rotator introduces 0.8 dB of insertion loss at 1550 nm, and <2 dB of loss across the whole wavelength range of 1520 nm to 1580 nm. The PER of the rotator is measured by adding a polarizer at the output of the isolator and measuring the residual TE light in the waveguide. The PER near 1550 nm is 25 dB, and ranges from 20 dB to 30 dB across the whole wavelength range. The broadband characteristics of the polarization rotator is attributed to the adiabatic design. The total insertion loss of the isolator is 6.5 dB compared to a Si only waveguide (TE input) at 1550 nm. The primary contributions to the loss is caused by the Ce:YIG upper cladding as well as the transition into the bonded Ce:YIG region. This can be further reduced by shortening the length of the Si/Ce:YIG bus waveguide, which is 2 mm long in this case. The isolation ratio is measured by injecting TE polarized light into the device while sweeping the current applied to the electromagnet. Flipping the orientation of the current is identical to changing the

propagation direction of light. A split in the resonant wavelength between forward and backward propagation is observed for 40 mA of current, which results in a maximum of 25 dB optical isolation as shown in Fig. 5c.

One of the improvements in this device compared with the microring isolators presented in Chapter 3 is the addition of the multi-coil electromagnet. This improves the thermal tuning efficiency in the device, as shown in Figure 5. The blue line depicts the MO nonreciprocal wavelength split, while the red line is the shift in resonance wavelength due to Joule heating. The MO effect saturates as the magnetization is saturated, and then slightly decreases at higher currents due to heating. Both mechanisms affect the isolation wavelength, which is plotted as a function of applied current (clockwise and counterclockwise injection) in Fig. 6c. The isolation wavelength can be tuned across a full free spectral range (FSR) of the ring, meaning the isolator is widely tunable.

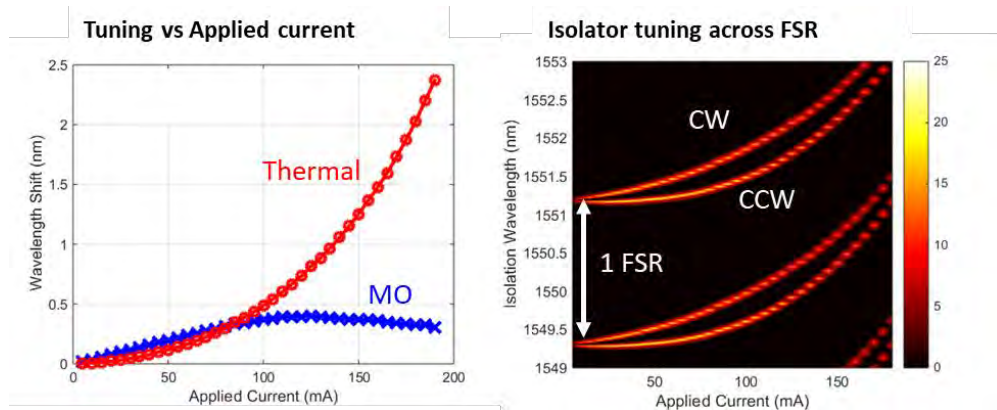


Figure 5.19: Thermal tuning of the TE mode microring isolator exceeding a FSR.

Over 20 dB of optical isolation can be achieved anywhere from 1540 nm to 1580 nm with proper tuning, as depicted for few select wavelengths in Fig. 6d. The limitations of

the range stem from the deviation of the ring from its critical coupling state, which provides the largest extinction ratio. The bandwidth of the polarization rotator could also limit the tuning range, but is not a concern for this device.

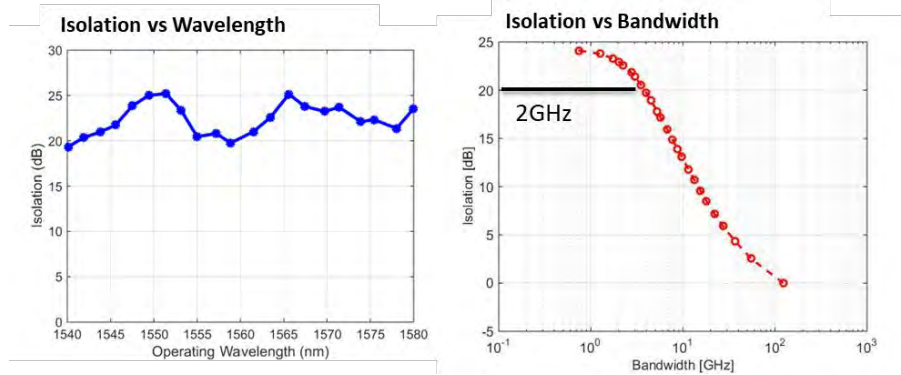


Figure 5.20: Measurements of isolation bandwidth and wavelength range.

5.4 MZI optical isolator and circulator for TE mode

As discussed in Chapter 4, MZI based isolators and circulators are useful when the large isolation bandwidth is needed. While TE mode MZI optical isolators have been demonstrated before, there has never been a demonstration of a circulator. A TE optical circulator is more challenging since the polarization converters must be on every port of the MZI. This allows any of the ports to serve as an input port in a PIC. The schematic is given in Figure 5.21, although the polarization rotators have not been drawn in for simplicity.

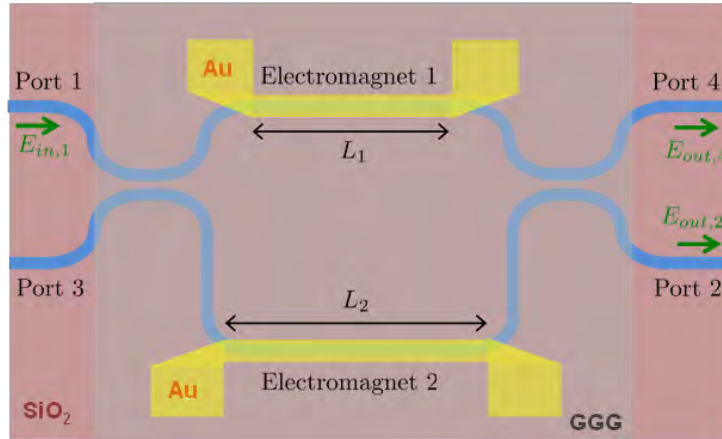


Figure 5.21: Schematic of the TE mode circulator (not showing polarization rotators)

The design of the TE mode MZI optical circulator is similar to the devices covered in Chapter 4. One significant change from previous devices is the use of broadband 50:50 splitters formed by a tapered adiabatic coupler, instead of the wavelength sensitive directional coupler. The design of this coupler is similar to other adiabatic 50:50 couplers used in silicon photonics [30], but has Ce:YIG bonded on top. Rather than interference based couplers such as directional couplers or MMIs, this coupler operates on the principle of mode evolution. The design of this coupler is given below in Figure 5.22. The coupler begins with two waveguides that are mismatched in width, such that they are beta-mismatched and do not couple. In the central region, the two widths are brought together, and light from the wider (narrower) input waveguide excites the even (odd) supermode of the coupled waveguides. Then, when the two widths are matched, the waveguides are separated. The whole process is adiabatic, and near 50:50 splitting ratio is observed over 100nm both in simulations as well as experiments. To ensure adiabaticity, the overall coupler length is long at 150 microns. The final parameters for the adiabatic 50:50 splitter are given in Table 5.4.

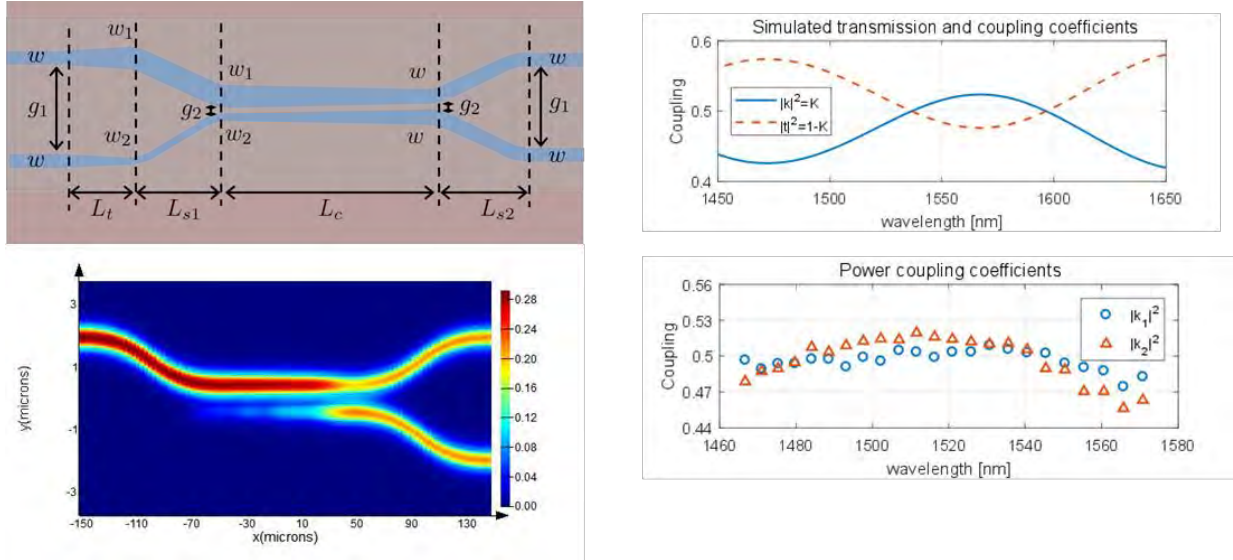


Figure 5.22: Schematic of the adiabatic 50:50 splitter as well as both simulated and experimental coupling values.

Symbol	Description	Size
w	Waveguide width	600 nm
w_1	Waveguide width	700 nm
w_2	Waveguide width	500 nm
g_1	Waveguide distance	6 μm
g_2	Coupler distance	250 nm
L_t	Taper length	100 μm
L_{s1}	s-bend	100 μm
L_{s2}	s-bend	20 μm
L_c	Coupler length	150 μm

Table 5.4: Relevant parameters of the adiabatic 50:50 splitter.

The optical behavior of the TE optical circulator is characterized in the C telecom band (1530 nm – 1565 nm). Considering the circulating direction Port 1 → Port 2 → Port 3 → Port 4 → Port 1, the optical spectra between two adjacent ports are shown on the top of Figure 5.23, while the corresponding spectra in the backwards direction are reported on the bottom. The operating wavelengths in the direction Port 1 → Port 2 → Port 3 → Port 4 → Port 1 are highlighted with the continuous vertical line, while the dashed vertical line refers to the Port 1 → Port 4 → Port 3 → Port 2 → Port 1 operating

wavelength. The isolation ratio computed between two adjacent ports reaches a maximum value of 30 dB near 1555nm, while a minimum isolation larger than 18 dB between two adjacent ports is guaranteed across the C-band. The insertion loss of this device is between 18 dB and 21 dB and it is measured by comparing it to a straight silicon reference waveguide of the same dimensions, however, without the bonded Ce:YIG.

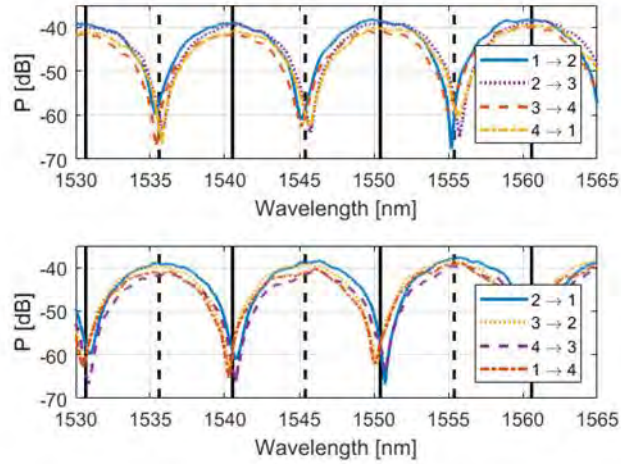


Figure 5.23: Experimental results for the transmission through a narrowband TE mode optical circulator.

To realize an optical circulator that operates across a broader bandwidth, the FSR is enlarged by reducing the path difference between the two arms, as was demonstrated in Chapter 4. In the case of a 1 μm path difference, the forward and backward optical spectra are shown in Figure 5.24. The spectrum is centered at 1560 nm and an optical isolation of more than 18 dB is provided between each port pair. The isolation is less than the narrowband device, as the phase condition is probably not optimal. Since multiple fringes are not visible, it is difficult to know what the best isolation condition is. Furthermore, variations in the polarization rotators can degrade the spectra, as it has different performance at different wavelengths and some residual TE is not fully

converted. In this case, the insertion loss is between 14 dB and 18dB when compared to a silicon reference waveguide at 1560 nm.

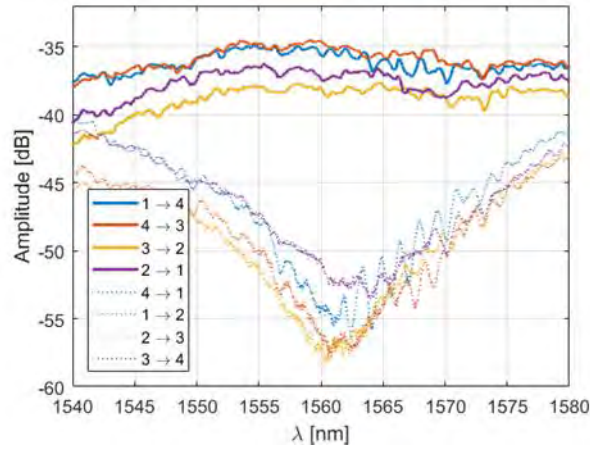


Figure 5.24: Experimental results for the transmission through a broadband TE mode optical circulator

Summary

The heterogeneous approach is not suitable to achieve NRPS for TE polarization, due to the nature of wafer bonding. Deposition of Ce:YIG on silicon using sputtering or pulsed laser deposition can achieve this, but is still in its infancy in terms of material development. Faced with a lack of strong optical isolation for TE modes, one option is to use polarization rotators. Such rotators can be designed to be broadband and adiabatic. Using the Ce:YIG as a part of the rotator simplifies the fabrication, and allows seamless integration with the isolator itself. Optical isolators operating for TE mode were demonstrated using both a microring and MZI approach, and the first optical circulator for TE mode on silicon was also realized. The optical losses for the circulator were large but can be straightforwardly reduced by improving design and fabrication on the rotators.

Single Microring Isolator (TE-mode), 3 coil	Value
Ring Radius	60 microns
Coupling Gap	270nm
Resonance Wavelength Split	0.38nm @ 120mA
Power Consumption	3mW @ 40mA
Isolation Ratio	25dB
20dB Isolation Bandwidth	2 GHz
Insertion Loss	6.5dB

Narrowband MZI-Circulator (TE-mode), 3 coil	Value
Common Arm Length	1000 microns
Arm Imbalance	70 microns
Designed FSR	10.2nm
Power Consumption	3.6mW @ 13mA
Isolation Ratio	30dB
20dB Isolation Bandwidth	0.6nm
Insertion Loss	18dB

Broadband MZI-Circulator (TE-mode), 3 coil	Value
Common Arm Length	1000 microns
Arm Imbalance	1.25 microns
Designed FSR	602.8nm
Power Consumption	3.6mW @ 13mA
Isolation Ratio	18dB
20dB Isolation Bandwidth	N/A
Insertion Loss	19dB

References

1. P. Pintus, D. Huang, P. A. Morton, Y. Shoji, T. Mizumoto, and J. E. Bowers, "Broadband TE Optical Isolators and Circulators in Silicon Photonics through Ce : YIG Bonding," **8724**, (2019).
2. J. P. Krumme and P. Hansen, "New magneto-optic memory concept based on compensation wall domains," *Appl. Phys. Lett.* **23**, 576–578 (1973).
3. A. F. Popkov, M. Fehndrich, M. Lohmeyer, and H. Dötsch, "Nonreciprocal TE-mode

- phase shift by domain walls in magneto-optic rib waveguides," *Appl. Phys. Lett.* **72**, 2508–2510 (1998).
4. M. Fehndrich, A. Josef, L. Wilkens, J. Kleine-Börger, N. Bahlmann, M. Lohmeyer, P. Hertel, and H. Dötsch, "Experimental investigation of the nonreciprocal phase shift of a transverse electric mode in a magneto-optic rib waveguide," *Appl. Phys. Lett.* **74**, 2918–2920 (1999).
 5. J. Fujita, S. Member, M. Levy, R. M. Osgood, L. Wilkens, and H. Dötsch, "Polarization-Independent Waveguide Optical Isolator Based on Nonreciprocal Phase Shift," **12**, 1510–1512 (2000).
 6. P. Pintus, F. Di Pasquale, and J. E. Bowers, "Integrated TE and TM optical circulators on ultra-low-loss silicon nitride platform," *Opt. Express* **21**, 5041 (2013).
 7. E. Ishida, K. Miura, Y. Shoji, H. Yokoi, T. Mizumoto, N. Nishiyama, and S. Arai, "Amorphous-Si waveguide on a garnet magneto-optical isolator with a TE mode nonreciprocal phase shift," *Opt. Express* **25**, 452–462 (2017).
 8. X. Y. Sun, Q. Du, T. Goto, M. C. Onbasli, D. H. Kim, N. M. Aimon, J. Hu, and C. A. Ross, "Single-Step Deposition of Cerium-Substituted Yttrium Iron Garnet for Monolithic On-Chip Optical Isolation," *ACS Photonics* **2**, 856–863 (2015).
 9. M. C. Onbasli, L. Beran, M. Zahradník, M. Kucera, R. Antoš, J. Mistrík, G. F. Dionne, M. Veis, and C. A. Ross, "Optical and magneto-optical behavior of Cerium Yttrium Iron Garnet thin films at wavelengths of 200–1770 nm," *Sci. Rep.* **6**, 1–10 (2016).
 10. Q. Du, T. Fakhrol, Y. Zhang, J. Hu, and C. A. Ross, "Monolithic magneto-optical oxide thin films for on-chip optical isolation," 413–418 (2018).
 11. L. Bi, J. Hu, P. Jiang, D. H. Kim, G. F. Dionne, L. C. Kimerling, and C. A. Ross, "On-chip optical isolation in monolithically integrated non-reciprocal optical resonators," *Nat. Photonics* **5**, 758–762 (2011).
 12. M. C. Onbasli, T. Goto, X. Sun, N. Huynh, and C. A. Ross, "Integration of bulk-quality thin film magneto-optical cerium-doped yttrium iron garnet on silicon nitride photonic substrates," **22**, 1564–1567 (2014).
 13. T. Goto, Y. Eto, K. Kobayashi, Y. Haga, M. Inoue, and C. A. Ross, "substrates for integrated optical circuits Vacuum annealed cerium-substituted yttrium iron garnet films on non-garnet substrates for integrated optical circuits," **939**, 3–6 (2013).
 14. A. D. Block, P. Dulal, B. J. H. Stadler, and N. C. A. Seaton, "Growth Parameters of Fully Crystallized YIG, Bi:YIG, and Ce:YIG Films With High Faraday Rotations," *IEEE Photonics J.* **6**, (2014).

15. P. Dulal, A. D. Block, T. E. Gage, H. A. Haldren, S. Y. Sung, D. C. Hutchings, and B. J. H. Stadler, "Optimized Magneto-optical Isolator Designs Inspired by Seedlayer-Free Terbium Iron Garnets with Opposite Chirality," *ACS Photonics* **3**, 1818–1825 (2016).
16. K. Srinivasan and B. J. H. Stadler, "Magneto-optical materials and designs for integrated TE- and TM-mode planar waveguide isolators: a review [Invited]," *Opt. Mater. Express* **8**, 3307 (2018).
17. C. Zhang, P. Dulal, B. J. H. Stadler, and D. C. Hutchings, "Monolithically-Integrated TE-mode 1D Silicon-on-Insulator Isolators using Seedlayer-Free Garnet," *Sci. Rep.* **7**, 1–8 (2017).
18. Y. Zhang, Q. Du, C. Wang, T. Fakhrol, and S. Liu, "Monolithic integration of broadband optical isolators for polarization-diverse silicon photonics," 1–20 (n.d.).
19. D. Dai, L. Liu, S. Gao, D.-X. Xu, and S. He, "Polarization management for silicon photonic integrated circuits," *Laser Photon. Rev.* **7**, 303–328 (2013).
20. D. Dai and J. E. Bowers, "Novel concept for ultracompact polarization splitter-rotator based on silicon nanowires," *Opt. Express* **19**, 10940 (2011).
21. D. Dai and M. Zhang, "Mode hybridization and conversion in silicon-on-insulator nanowires with angled sidewalls," *Opt. Express* **23**, 32452 (2015).
22. U. Si-nanowire-based, Z. Wang, and D. Dai, "Ultrasmall Si-nanowire-based polarization rotator," **25**, 747–753 (2008).
23. H. Deng, D. O. Yevick, C. Brooks, and P. E. Jessop, "Design rules for slanted-angle polarization rotators," *J. Light. Technol.* **23**, 432–445 (2005).
24. X. Wu, C. Huang, K. Xu, C. Shu, and H. K. Tsang, "Mode-Division Multiplexing for Silicon Photonic Network-on-Chip," *J. Light. Technol.* **35**, 3223–3228 (2017).
25. J. Leuthold, J. Leuthold, J. Eckner, J. Eckner, E. Gamper, E. Gamper, P. a Besse, P. a Besse, H. Melchior, and H. Melchior, "Multimode interference couplers for the conversion and combining of 0th & 1st-order modes.," *J. Light. Technol.* **16**, 1228–1239 (1998).
26. W. D. Sacher, T. Barwicz, B. J. F. Taylor, and J. K. S. Poon, "Polarization rotator-splitters in standard active silicon photonics platforms," *Opt. Express* **22**, 3777 (2014).
27. Y.-C. Chang, S. P. Roberts, B. Stern, and M. Lipson, "Resonance-Free Light Recycling," 6–10 (2017).

28. Y. Shoji, A. Fujie, and T. Mizumoto, "Silicon waveguide optical isolator operating for TE mode input light," *IEEE J. Sel. Top. Quantum Electron.* **22**, (2016).
29. S. Ghosh, S. Keyvaninia, Y. Shirato, T. Mizumoto, G. Roelkens, and R. Baets, "Optical isolator for TE polarized light realized by adhesive bonding of Ce:YIG on silicon-on-insulator waveguide circuits," *IEEE Photonics J.* **5**, (2013).
30. Y. Wang, L. Xu, H. Yun, M. Ma, A. Kumar, E. El-fiky, R. Li, N. Abadiacalvo, L. Chrostowski, N. A. F. Jaeger, and D. V. Plant, "Polarization-Independent Mode-Evolution-Based Coupler for the Silicon-on-Insulator Platform," *IEEE Photonics J.* **10**, 1–10 (n.d.).

Chapter 6

Laser and Isolator integration

This section will cover ongoing efforts to integrate the optical isolators described in previous chapters with an integrated laser. The motivation for this is clear, and will be briefly discussed. The heterogeneous silicon/III-V laser is a promising candidate to integrate with the isolators, as it shares the same silicon waveguides and bonding procedures. The path towards heterogeneous integration of isolators with lasers on silicon is outlined and preliminary fabrication and results are discussed.

6.1 Background and Motivation

On its own, an optical isolator is not particularly useful. The importance of the device is only clear when integrated with a laser. As discussed in the introduction, the best placement of the optical isolator is directly after the laser, before the rest of the PIC or the light is collected into a fiber. Only then will the results justify the means and added complexity of the isolator. However, there have been very few demonstrations of lasers integrated with isolators for many reasons (mainly material incompatibility and fabrication complexity).

One possible solution is to design and fabricate lasers on a garnet substrate. Garnet based solid-state lasers are widely used, the most famous of which is the neodymium-doped yttrium aluminum garnet (Nd:YAG) laser, which emits at 1064nm. GGG can also serve as a host for rare-earth dopants such as Nd [1] or Yb [2], and edge emitting lasers using etched planar waveguides on GGG have been demonstrated [3]. The downsides to this are obvious. The lasers must be optically pumped and further integration is limited. The majority of semiconductor laser and PIC technology is centered at 1.3 and 1.55 microns due to transparency windows for optical fiber, which is not optimal for garnet lasers. Finally, the semiconductor diode laser is too deeply entrenched in industry today for laser and isolator integration to take place on garnet substrates. Thus, the focus of researchers over the past few decades has been integration on III-V and more recently, silicon substrates.

As mentioned in Chapter 2.3, NRL isolators have been successfully integrated with lasers [4], it comes at the cost of high power consumption, large optical loss, and additional noise generated by the SOA. They also require strong magnetic fields, which is generally seen to be a disadvantage. A “passive” optical isolator such as the NRPS or Faraday isolator is preferred. To the best of our knowledge, a laser has never been integrated with a Faraday or NRPS based isolator of any kind.

6.2 Co-design of heterogeneous silicon laser and isolator

The integration of magneto-optic isolator with a laser on silicon requires some careful design and consideration. The first step is to choose the right photonic platform to demonstrate such a PIC. Given the choice to use silicon waveguides as a part of the

optical isolator, it is natural that a silicon waveguide-based laser such as the heterogeneous silicon/III-V laser is used. The design of the heterogeneous silicon/III-V laser was the culmination of work from many previous students, and the subject of many publications. When considering the addition of an isolator to the laser, the overarching design strategy was to change as little as possible in the two processes. A few modifications did need to be made, which will be highlighted in this section. A detailed explanation of the design of the heterogeneous silicon/III-V laser will not be given here, and can be found elsewhere [5].

One of the main design challenges is the mismatch of waveguide dimensions between the laser and the isolator. The cross-section of the heterogeneous silicon/III-V laser is shown in Figure 6.1. It has a silicon waveguide height of 500nm, which is chosen to match the refractive index of the silicon slab with the thick InP gain region.

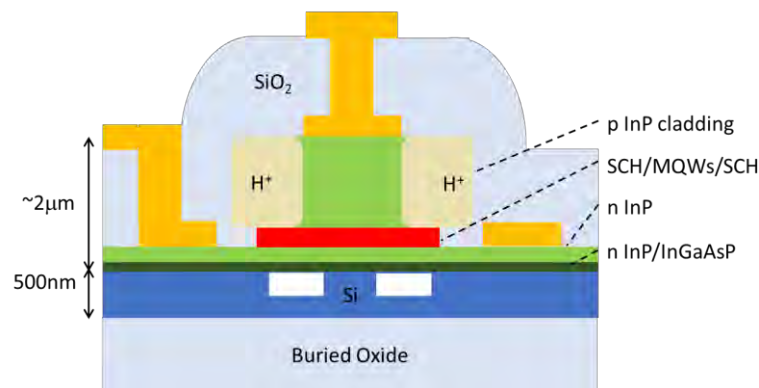


Figure 6.1: Schematic of the cross-section of a heterogeneous silicon/III-V amplifier waveguide.

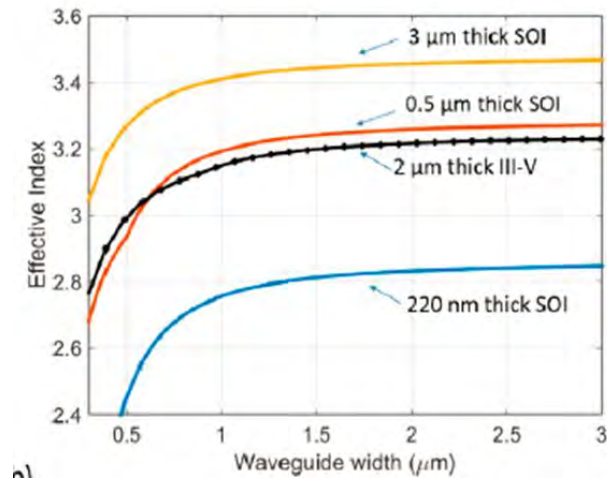


Figure 6.2: Effective index of various silicon thicknesses at different waveguide widths compared with the III-V epitaxial stack. Further details found in [6].

Silicon waveguides thinner than 400nm will suffer from low coupling to the InP [7]. However, the optimal silicon thickness for isolators is between 200 and 250nm, as explored in Chapter 3. It is possible to transition between the two silicon waveguides using a partial etch and taper structure [8], but this roughens the silicon surface, which complicates the bonding process. Furthermore, the taper could serve as a source of reflections. Since the main purpose of the isolator is to block reflections from reaching the laser, the isolator should not introduce significant reflection. The solution explored in this work is local oxidation of silicon (LOCOS) [9], which thins down a lithographically defined area of the wafer. It can be performed at the start of the process, prior to any waveguide etching.

From a fabrication standpoint, the challenges lie in managing the thermal budget of the process, as well as the simultaneous processing of vastly dissimilar materials (III-V, silicon, and garnet). While the lattice constant mismatch can be somewhat alleviated by wafer bonding, the thermal expansion coefficient mismatch between III-V and silicon

provides a limited thermal budget for the process. Rapid thermal anneal performed at 420C for 2 minutes have degraded laser performance [5], and temperatures should be ideally kept below 300C. The monolithic approaches for garnet deposition discussed in Chapter 5 may have a difficult time meeting this thermal budget. Studies have shown that 650C is required to crystallize YIG [10], and TIG films are annealed even hotter, at 900C [11]. Therefore, if a monolithic approach is pursued, the garnet would have to be deposited near the beginning of the process, prior to any III-V bonding to preserve the thermal budget for the rest of the process. This could affect subsequent steps and may require a complete retooling of the heterogeneous silicon/III-V process. Alternatively, bonding of garnet is attractive as it can be added as a back-end process after laser fabrication. Since the garnet is already fully crystallized prior to bonding, the thermal anneal is not required. In fact, the highest temperature process in isolator fabrication is post-bonding anneal 200C, which will not negatively impact the laser performance. The inclusion of the isolator processing at the end also reduces the amount of overlap with laser fabrication, which simplifies the process greatly.

The other point of concern is how to know that the isolator is functional once the laser is integrated with it. Unlike previous devices, a tunable laser sweep in the forwards and backwards direction is not available. Instead, monitor photodiodes are placed in strategic locations of the PIC, as shown in Figure 6.3. Two variations of the PIC are shown, with a tunable Vernier laser as well as a DFB. One photodiode (PD1) is tapped from the output of the laser, to provide a monitor for the lasing power. The remainder of the forwards propagating light travels through a polarization rotator to convert from TE to TM mode, and into the Ce:YIG region. The silicon transition from 500nm to 220nm

is also included right before the polarization rotator. The light goes through an isolator (circulator) that is either the microring or MZI configuration, and a portion of the light is fed back using a tunable reflector. This consists of a balanced MZI with a loop mirror at the end. A heater is used to control the phase of one of the arms, to enable a tunable reflection from 0 to $4k(1-k)$, where k is the power coupling constant of the 2×2 couplers in the MZI. Finally, PD3 can be used to measure the amount of light that is dropped across the ring or MZI circulator.

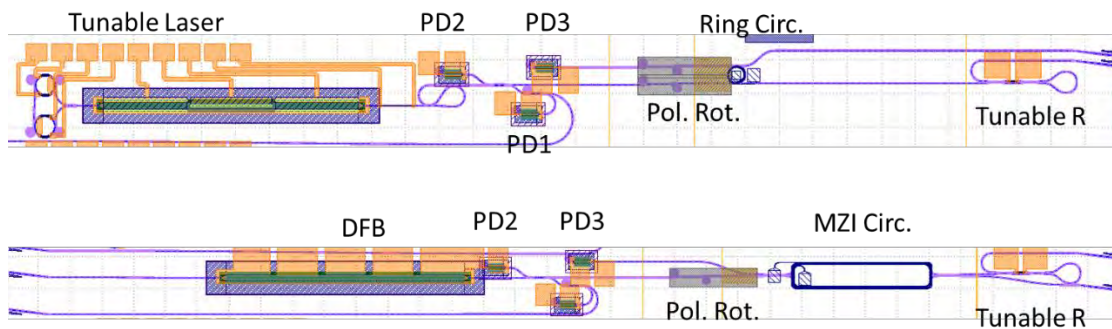


Figure 6.3: Schematic of the layout of integrated lasers with isolators and circulators.

Together, each of the PDs enable a monitor on where the light is travelling. The PIC can first be tested with the tunable reflector set to a minimum (also maximizing output power). Then, the reflection can be increased without turning on the isolator, and the laser characteristics can be recorded. Finally, the isolator can be turned on. Monitoring the power on the PD can signal when the laser is aligned with the isolation wavelength. An alternate way to characterize the isolator is to inject light from a tunable laser source from the right side, and monitoring the power measured on PD3 as the laser is swept.

This provides a spectral response of the isolator, from which the extinction ratio and resonance wavelength can be determined.

6.3 Fabrication and Preliminary Results

As previously mentioned, the overall strategy is to change as little as possible from the two separate processes, and “stitch” the processes together. The entire fabrication flow is depicted in Figure 6.4 and can be roughly divided into silicon processing, III-V processing, metallization, and isolator processing. This section will provide an overview of the fabrication, but will not go into the details of the heterogeneous silicon/III-V process, which can be found elsewhere [5]. Deviations from the “standard” laser process flow are highlighted and discussed.

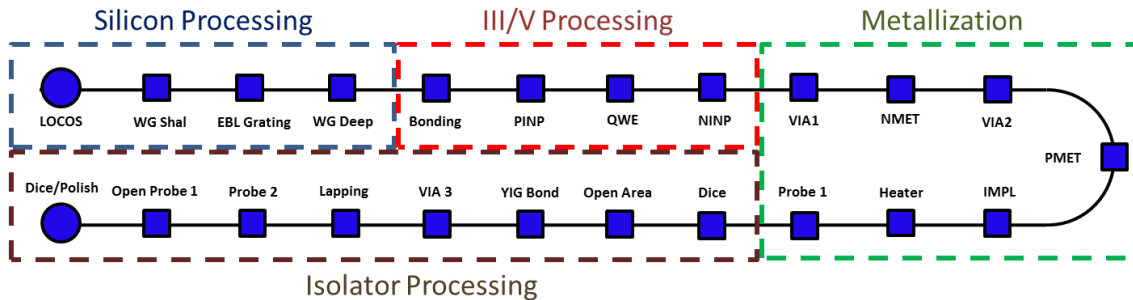


Figure 6.4: Complete processing flow for the laser with isolator

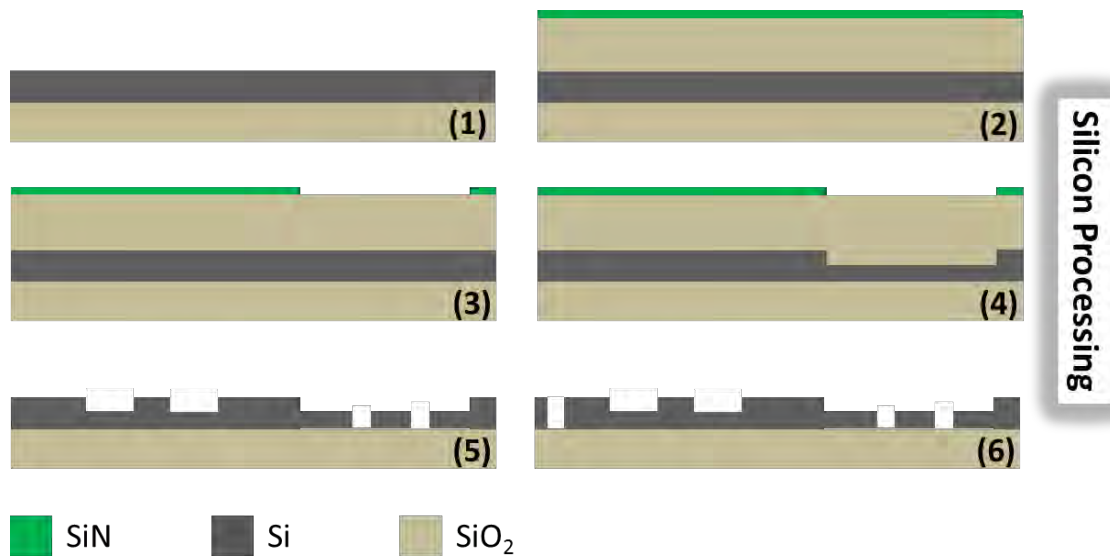


Figure 6.5: Process flow of the first few silicon processing steps

The first few steps involve silicon processing, which is outlined in Figure 6.5. The fabrication begins with the local oxidation of silicon (LOCOS) to thin the silicon device layer down from 500nm to roughly 230nm in the areas where the isolators will be fabricated. This is done by taking a blank 500nm SOI wafer, patterning and etching alignment marks, and then depositing 2000nm of SiO_2 and 200nm of SiN on top of the whole wafer. This is followed by dry etching away the SiN in the areas that will be thinned down by oxidation. The wet thermal oxidation is then performed at 1050C for 8 hours, followed by removing the remaining SiO_2 and SiN using a combination of dry etching and BHF. The two control parameters in this process is the SiO_2 thickness and the wet oxidation time. The oxide thickness is related to the length of the transition between the thinned and un-thinned areas. Thicker oxide provides a more gradual transition (longer taper) but slows down the oxidation. The actual thinned amount is determined by the oxidation time. Multiple tests showed that 2 microns of SiO_2 and 8

hours of wet oxidation repeatably thins down the silicon from 500nm to 230nm with a transition length around 6 to 8 microns. Ellipsometry shows that while the silicon nitride mostly prevents oxidation in the un-thinned areas, there is still some small amount of silicon (~10nm) that is consumed. As a result, the final silicon heights after oxidation are closer to 490nm and 220nm.

The images of the LOCOS taper are shown in Figure 6.6, in which a cross-sectional view as well as a top-down view are shown. This is from one of the test runs, so the silicon heights are a bit off the final values. AFM scans of the thinned and un-thinned silicon areas are given in Figure 6.7, showing essentially the same surface quality. This is consistent with previous experiments that showed that oxidation preserves the surface roughness.

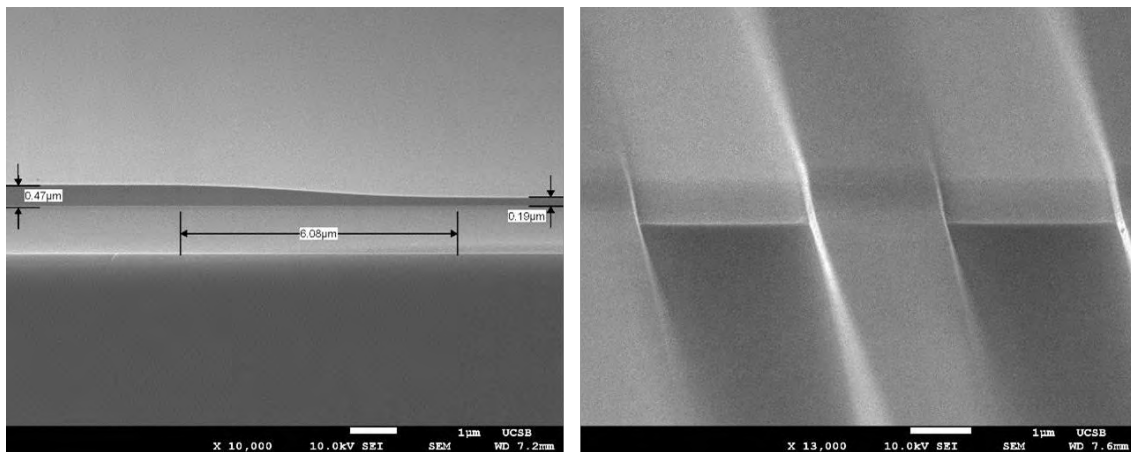


Figure 6.6: SEM images of the LOCOS transition

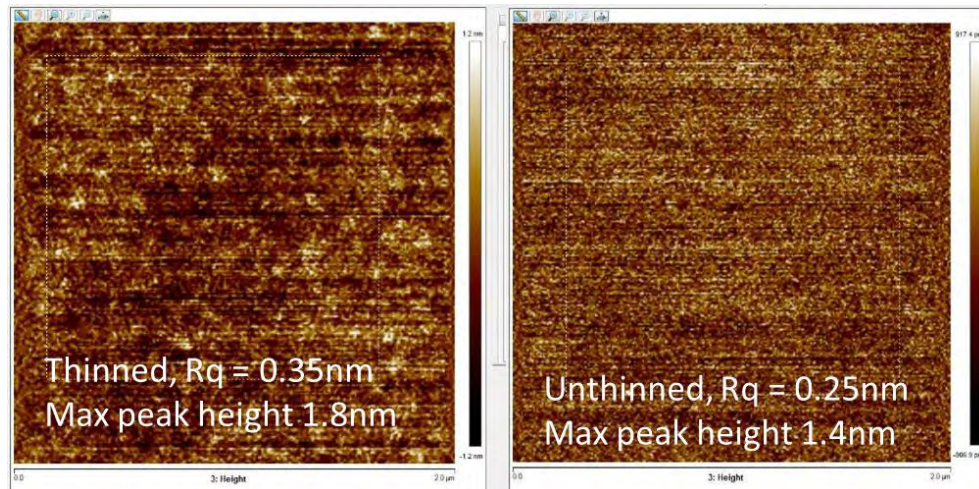


Figure 6.7: AFM comparison of the surface quality of the thinned and unthinned silicon areas

Following the LOCOS, a single waveguide etch is used to define the shallow, 231nm etch rib waveguides in the laser sections, as well as the fully etched waveguides in the isolator sections. This single etch alleviates any need to do precise local alignment and guarantees that the waveguide is continuous between the two regions. Following the waveguide etch, gratings can be defined where needed, and vertical outgassing channels are etched in the silicon.

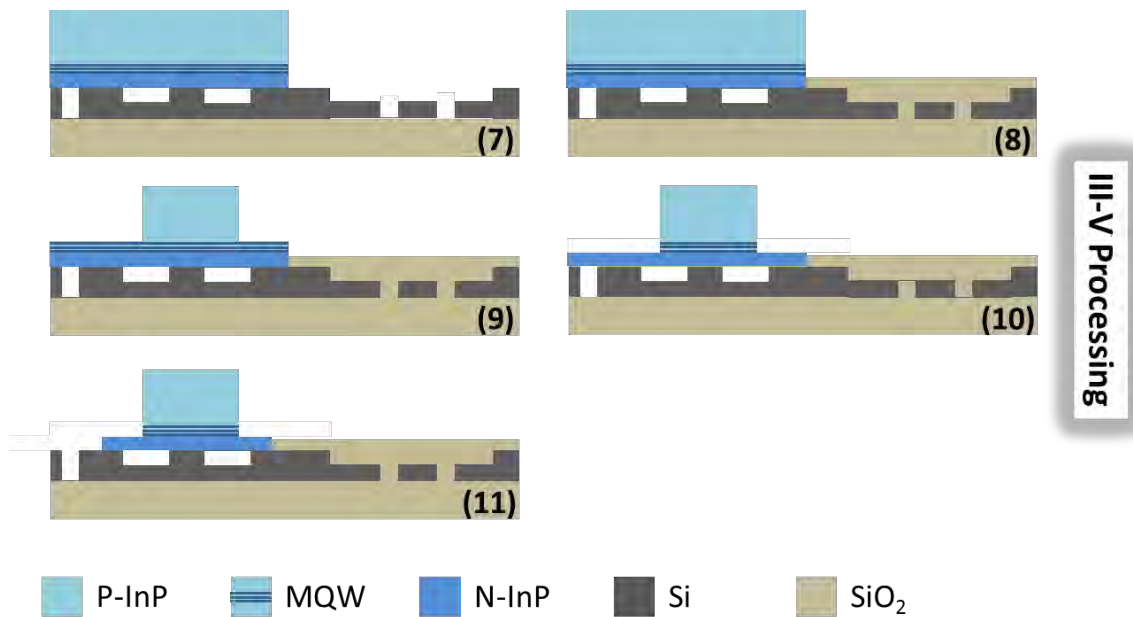


Figure 6.8: Process flow of the III-V bonding and subsequent processing.

The next steps involve bonding and processing III-V on the silicon, as shown in Figure 6.8. The III-V epi consists of InAlGaAs multiple quantum well material, with 3 quantum wells. The design of the epi is the same as previous work in the group [5]. The III-V is bonded to the silicon wafer, making direct contact with the un-thinned areas, followed by a 2 hour anneal at 300C. The rest of the wafer is immediately coated with sputtered SiO₂ to protect them from upcoming processing. The InP substrate is then removed using a combination of mechanical polishing and 3:1 HCl:H₂O acid. An InGaAs layer (50nm thick) serves as an etch stop for the wet etch.

The laser mesas are fabricated using a methane hydrogen argon (MHA) etch. A liftoff hardmask is used to define the P-mesas, which is used for several reasons. A hardmask is needed to prevent hydrogen to contaminate the highly doped P-contact layer. It is also used due to its high selectivity with InP and InGaAs, since over 1.5 microns is removed

during this etch. A liftoff technique is used as it is simpler than the alternative, which is to deposit SiO_2 everywhere, and proceed to etch the hardmask. Furthermore, due to the presence of bond fails that expose the silicon waveguide, the hardmask etch would attach the silicon waveguides in those areas. Thus, a liftoff hardmask is used in conjunction with DUV lithography, which allows for extremely sharp tapers to be formed. This is important to reduce the loss and reflection when transitioning from the gain section to the passive silicon waveguides. Following the hardmask liftoff, the P-mesa is etched using MHA. A typical etch lasts for 35-40 minutes and is tracked using a laser monitor. The aluminum containing SCH layers underneath the P-InP naturally provide an etch stop, as the MHA etch slows down considerably (roughly 100 times) in the SCH, allowing for significant overetch to be performed. Images of the etched P-InP taper is shown in Figure 6.9. Sharp ($<300\text{nm}$) features can be achieved, and the verticality of the etch is good given the 1.5 micron etch depth.

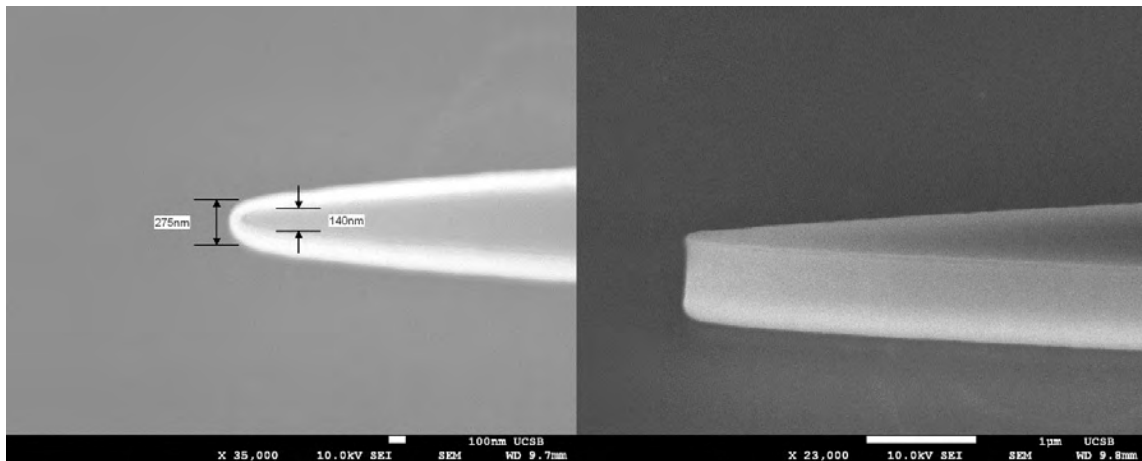


Figure 6.9: SEM images of the P-InP taper after etching with MHA.

The quantum wells are etched using a phosphoric acid mixture, with a photoresist mask. The hardmask should remain on during this, as well as the upcoming N-InP etch

in order to protect the top P-contacts from hydrogen. The N-InP is etched using MHA as well, but with a photoresist mask, as the N-layer is much thinner. MHA does not attack silicon, so this step can be overetched, much like the P-InP. A lower voltage on the RIE tool is used in order to prevent the photoresist from burning, after which it becomes nearly impossible to remove. A short BHF dip is performed after the III-V etching is all complete in order to remove the P-InP hardmask, as well as any MHA residue on the waveguides. The wafer can be “prewet” in DI water before the BHF to prevent the acid from penetrating underneath the bonded areas. Since the bond interface between silicon and III-V is oxide, it can be attacked by the BHF, which sometimes results in bubbles in the mesa, as seen in Figure 6.10. Images of the devices following all III-V etching are shown in Figure 6.11.

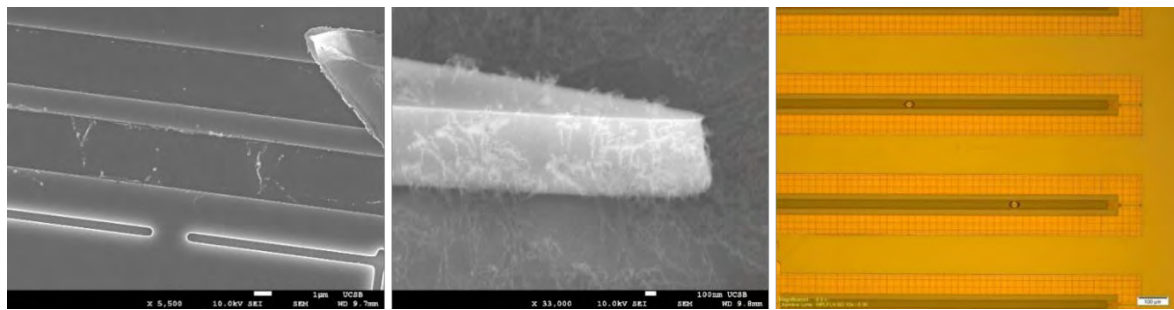


Figure 6.10: SEM images of residue after the MHA etch using a resist mask and bubbles that may form under the mesa after BHF cleaning

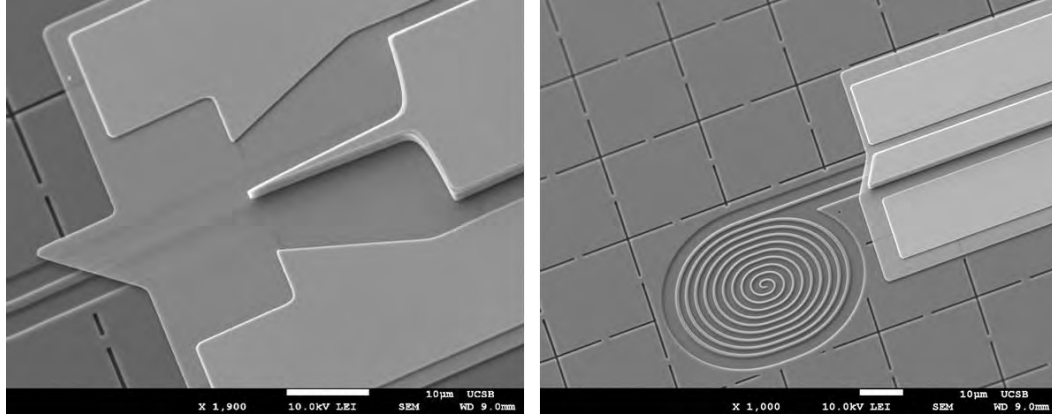


Figure 6.11: Completed laser mesa structures with transitions to the silicon waveguides.

Once the III-V processing has concluded, the backend, or metallization of the laser diodes begins. First, the entire wafer is covered with a sputtered SiO_2 cladding (450nm thick), which passivates the laser mesas. Then, vias are etched to expose the highly N-doped InP, and then the N-metal is put down. A second deposition of SiO_2 is deposited (450nm thick), before the P-contacts are opened with a second via etch. This is due to areas of the laser where the P and N metals overlap and must be separated with oxide to prevent a short. The dual via process was established to prevent N-metal peeling throughout the process, as was seen in previous fabrication runs. The combination of the two via oxides (900nm) is sufficient to separate the silicon waveguides from any metal routing or pads, which may induce optical loss. Care must be taken that the N and P-metals are actually separated by the second via oxide, as there is significant topology to the wafer at this point. Doing the p-metal last also has the benefit that the sidewalls of the tapers are completely covered with oxide at that point. Thus, the metal can be deposited all around the taper tip, as seen in Figure 6.13. This reduces lithographic alignment constraints and helps the taper become pumped, which reduces loss.

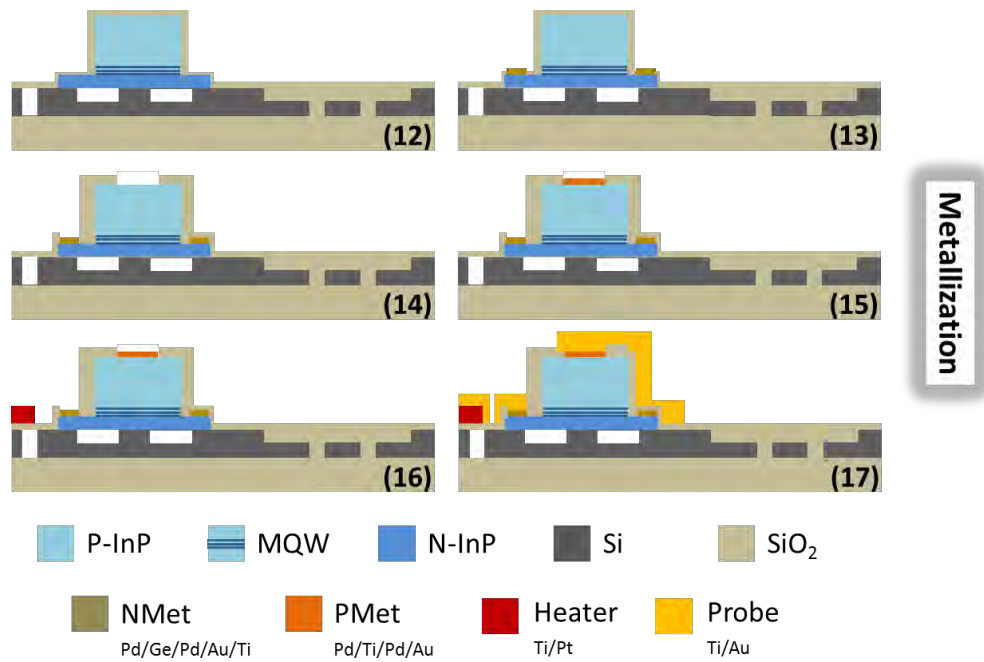


Figure 6.12: Process flow of the backend metallization of the lasers.

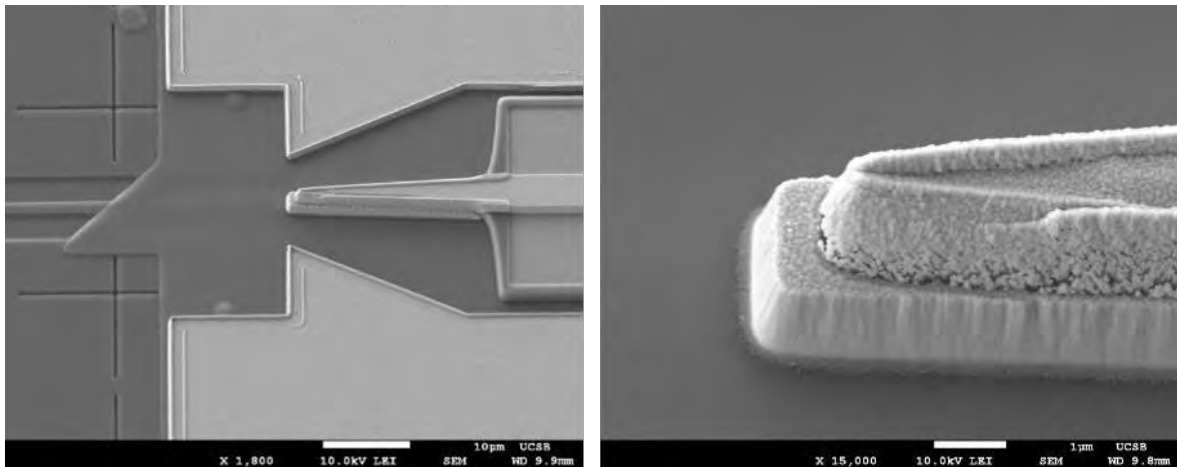


Figure 6.13: SEM images of the lasers after metallization to the n and p contacts is complete.

The P-metal serves as a mask for implantation. Hydrogen implantation is used to define the current channels. Finally, heaters (Ti/Pt) and probe metal (Ti/Au) is lifted off.

At this point, the laser is fully functional, and can be screened. Thanks to the placement of monitor photodiodes alongside each laser, the LIV of the laser can be characterized at this point, prior to any isolator fabrication. Up to now, the process has had very minimal changes, with the exception of the LOCOS. The following steps were added at the end of the laser process to fabricate the isolator.

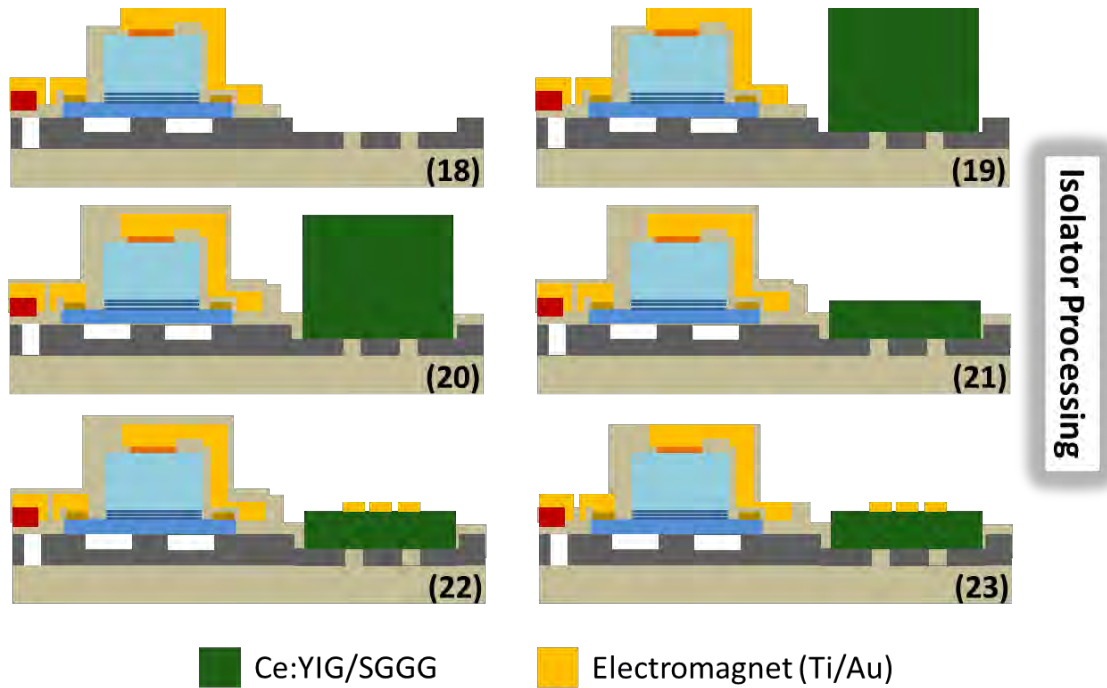


Figure 6.14: Process flow of the isolator integration after laser processing is complete.

First, the chip is downsized to individual chiplets. Up until now, the processing has all been on a 4" SOI wafer, to take advantage of the superior lithography provided by the DUV stepper at UCSB. However, the following steps do not need critical alignment, and therefore the i-Line stepper can be used, which handles piece parts. Following dicing the wafer into individual dies, the areas that were previously thinned by LOCOS are opened up. This is done by masking the die with photoresist, reflowing the resist, and using BHF

to strip away the oxide (estimated 1.2 microns thick) on the LOCOS areas. Slight overetch is needed to clear up the areas, which need to be clean in order for bonding. However, significant overetch is risky as the waveguides in these areas are fully etched, which means they are prone to being undercut and breaking.

While this process was successfully carried out over multiple test chips, the real chip containing lasers encountered some issues with some oxide residue in spots that were extremely stubborn to BHF. Since excessive BHF is risky, the call was made to proceed with the Ce:YIG bond. In hindsight, it may have been better to etch away these areas with dry etch, as voids are preferred over bumps when it comes to bonding. After the bond areas have been opened up, the Ce:YIG chips are bonded in place, followed by a SiO₂ sputter deposition, as was detailed in Chapter 3. This does cover up all the electrical pads on the lasers, which need to be opened up later. The substrate removal of Ce:YIG proceeds as previously discussed, with extreme care taken to level the chip such that lasers are not damaged by the polishing. Thinning down to 10 microns was successfully achieved with no damage to the surrounding areas. Finally, the electromagnets are deposited using evaporated gold and a liftoff process. The last step is to open up the contact pads for the lasers and photodiodes, which is done using a dry etch. The chip is diced and polished in preparation for testing.

Unfortunately, due to the problem of residue in the bonding areas, the overall bond yield was poor, and only a fraction of the YIG chip bonded successfully. Only a few resulting devices were testable, and the laser performance was poor due to some P-contact issues that created a non-Ohmic contact. For the laser that worked, other elements in the PIC were unfunctional, which prevented a complete characterization of

the laser with isolator. In particular, a defect in the waveguide near the output facet prevented any light from being coupled out. Investigation with an infrared camera showed light propagating through the bonded Ce:YIG section, but not leaving the chip. Future runs should address the contact issues with the laser. The isolator integration seemed to be viable, and the troubles encountered in this run are seen as an unlucky break.

Summary

A pathway towards heterogeneous integration of lasers with isolators on silicon is given. A limited thermal budget means that the preferred approach is to bond the Ce:YIG towards the back-end of the process. Fabrication details are given, in which the laser and isolator processing were separated as much as possible. Due to some unlucky breaks, the preliminary run did not result in any working devices, but ongoing efforts aim to make this integration a reality in the near future.

References

1. S. J. Field, D. C. Hanna, A. C. Large, D. P. Shepherd, A. C. Tropper, P. J. Chandler, P. D. Townsend, and L. Zhang, "Ion-implanted Nd:GGG channel waveguide laser," *Opt. Lett.* **17**, 52–54 (1992).
2. M. Shimokozono, N. Sugimoto, A. Tate, Y. Katoh, M. Tanno, S. Fukuda, and T. Ryuoh, "Room-temperature operation of an Yb-doped Gd₃Ga₅O₁₂ buried channel waveguide laser at 1.025 μm wavelength," *Appl. Phys. Lett.* **68**, 2177–2179 (1996).
3. R. Gerhardt, J. Kleine-Börger, L. Beilschmidt, M. Frommeyer, H. Dötsch, and B. Gather, "Efficient channel-waveguide laser in Nd:GGG at 1.062 μm wavelength," *Appl. Phys. Lett.* **75**, 1210–1212 (1999).
4. H. Shimizu and Y. Nakano, "Monolithic Integration of a Waveguide Optical Isolator

- With a Distributed Feedback Laser Diode in the 1.5-um Wavelength Range," *Technology* **19**, 1973–1975 (2007).
5. M. Davenport, "Heterogeneous Silicon III-V Mode-Locked Lasers," (2017).
 6. M. Tran, D. Huang, T. Komljenovic, J. Peters, A. Malik, and J. Bowers, "Ultra-Low-Loss Silicon Waveguides for Heterogeneously Integrated Silicon/III-V Photonics," *Appl. Sci.* **8**, 1139 (2018).
 7. P. Dong, T.-C. Hu, T.-Y. Liow, Y.-K. Chen, C. Xie, X. Luo, G.-Q. Lo, R. Kopf, and A. Tate, "Novel integration technique for silicon/III-V hybrid laser," *Opt. Express* **22**, 26854 (2014).
 8. S. Keyvaninia, G. Roelkens, D. Van Thourhout, C. Jany, M. Lamponi, A. Le Liepvre, F. Lelarge, D. Make, G.-H. Duan, D. Bordel, and J.-M. Fedeli, "Demonstration of a heterogeneously integrated III-V/SOI single wavelength tunable laser," *Opt. Express* **21**, 3784–3792 (2013).
 9. G. Beaudin, A. Belarouci, and V. Aimez, "Precise localized thinning and vertical taper fabrication for silicon photonics using a modified local oxidation of silicon (LOCOS) fabrication process," *Opt. Express* **23**, 4377 (2015).
 10. T. Goto, M. C. Onba, C. A. Ross, M. C. Onbaşlı, and C. A. Ross, "Magneto-optical properties of cerium substituted yttrium iron garnet films with reduced thermal budget for monolithic photonic integrated circuits Taichi," *Opt. Express* **20**, 163–166 (2012).
 11. P. Dulal, A. D. Block, T. E. Gage, H. A. Haldren, S. Y. Sung, D. C. Hutchings, and B. J. H. Stadler, "Optimized Magneto-optical Isolator Designs Inspired by Seedlayer-Free Terbium Iron Garnets with Opposite Chirality," *ACS Photonics* **3**, 1818–1825 (2016).

Chapter 7

Beyond optical isolators and circulators

Now that a pathway towards integration of the isolator with the laser has been established, it is useful to examine how the devices might function in real-life PICs. In this chapter, we analyze the role of the isolator or circulator in various PIC such as optical transmitters, microwave generators, WDM networks, optical sensors, and optical switches. Detailed examples of the latter two are given, showing the uses of integrated magneto-optic waveguides beyond just optical isolators and circulators.

7.1 Optical isolators and circulators in PIC

In the ideal case, an optical isolator would be included after every semiconductor laser. However, given the difficulties of integrating the optical isolator, it is important to take a deeper look into PICs, and examine which applications really call for an optical isolator.

We begin with possible the most commonly used PIC, which is the optical transmitter for data transmission. It consists of a laser followed by an optical modulator (electro-absorption or phase modulator). Any modulation will induce sidebands onto the optical

carrier, with the strength of the sidebands proportional to the RF modulation power. The combined effect of this along with the pseudo-random bit sequence (PRBS) applicable to data transmission is a “smearing” out of the optical carrier in spectra. Most reflections are broadband in nature (with the exception of gratings), so any reflections coming after the modulator will not necessarily be at the laser wavelength. Thus, narrowband optical isolators such as the microring isolator may not be applicable for data transmission. MZI based isolators may be the better fit.

For analog applications in which purely sinusoidal modulation is used, the microring isolator may have some use. Feedback sensitivity is generally characterized by studying the relative intensity noise (RIN) of the laser as the feedback into the laser is increased. Studies by Morton Photonics have shown that the laser (single-frequency) is more tolerant to reflections at wavelengths other than the optical carrier. Combined with the fact that the sidebands are always lower than the carrier, this may indicate that microring isolators have a fit in these microwave applications. In any case, it is advantageous to place the isolator directly after the laser, as was discussed in Chapter 6.

Another commonly used PIC that would benefit from an optical isolator is a single wavelength laser with booster semiconductor optical amplifier (SOA), as shown in Figure 7.1. This device is a distributed feedback (DFB) laser with an optical amplifier to increase the output power. Ideally, an isolator would be included in between the laser and the SOA. Otherwise, the SOA, which emits in both directions, could destabilize the laser. This may be seen in broadened linewidths of the laser, as well as mode instability. The latter is especially important when the laser itself has poor mode suppression ratio, as the additional gain from the SOA will cause undesired modes to lase.

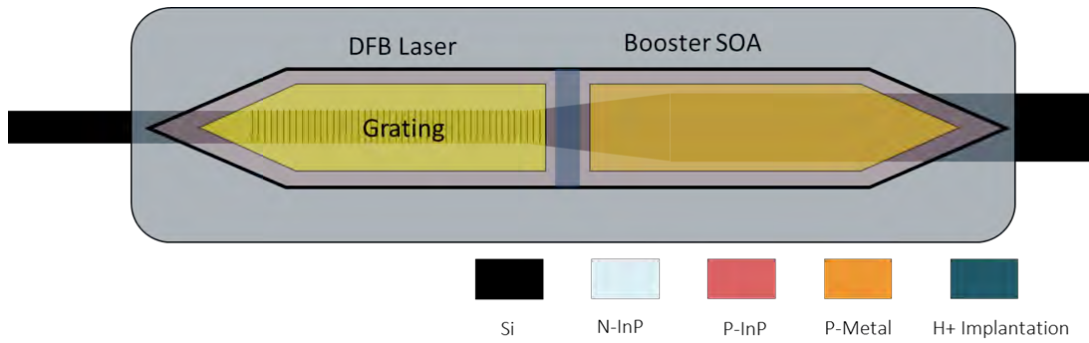


Figure 7.1: Schematic of a single-frequency DFB with a booster amplifier.

Circulators also have many uses in PIC, some of which will be discussed here. The primary use is to separate counterpropagating signals. This has tremendous use in many sensing systems, which sense reflected light. Without the use of an optical circulator or optical isolator, this reflection will be directed into the laser cavity. Optical circulators are commonly used with Bragg grating reflectors, to reroute the reflected light to a third port. This can be used in WDM networks as add-drop multiplexers [1].

Circulators also enable bidirectional operation of many PIC. This can open up opportunities similar to what is done in reflective erbium amplifiers, in which the same length of erbium doped fiber amplifies the light twice by placement of a mirror on one end and a circulator on the other [2]. Alternatively, amplification in a bidirectional optical link can be achieved [3]. Distributed sensing systems such as OFDR or OTDR analyze the amplitude and phase of the reflected light. Thus, an optical circulator or optical isolator plus coupler is needed if the full integration of everything except the device (fiber) under test is required. Another use of circulators in PIC is in Sagnac-type interferometric sensors, such as optical gyroscopes or optical current sensors. This is discussed in more detail in the following section.

7.2 Magnetic sensors

The most commonly used magnetic sensor is the Hall effect sensor, which measures the voltage difference across an electric conductor that has current flowing transverse to an applied magnetic field. However, there are some downsides, as the Hall effect sensor is sensitive to electromagnetic interference (EMI), and has rather limited dynamic range. Using optics to perform magnetic and current sensing has inherent advantages in the sense that the systems are EMI resistant, and have high suppression of spurious signals due to the high common-mode rejection of the system. Typical FOC are wrapped around the current carrying wire, such that it is only sensitive to magnetic fields propagating circularly around the wire. A commercial application of optical magnetic sensors is the fiber optic current sensor (FOCS) for current sensing in power lines. Commercial power line FOCS can sense currents up to 500kA with an accuracy down to 0.1%.

The operating principle of these FOC is Faraday rotation. As was discussed in Chapter 2, the polarization of light is rotated in a magnetic medium, which can be detected. Alternatively, the interference between two counterpropagating beams of light with circular polarization can be detected. This is otherwise known as the Sagnac configuration, and most commonly utilized in optical gyroscopes. Most FOC utilize the Sagnac approach with silica fiber, which has a Verdet constant of $0.54 \text{ rad}/(\text{Tm})$ near 1550nm [4]. Such a weak effect means that long spools of fiber are needed to achieve high sensitivity.

Compared with standard silica fiber, terbium-doped fiber has a Verdet constant that is $-32 \text{ rad}/(\text{Tm})$ at 1060nm, which is 27 times larger [5]. This can be utilized to construct

miniaturized FOC was constructed in the polarimetric approach [6], or the interferometric approach [7]. The schematic of the interferometric sensor is shown in Figure 7.2, in which 10cm of Tb-doped fiber was used as the sensing element. A solenoid is used to generate a magnetic field parallel to the length of the fiber. Sensitivities down to 0.1mA in the solenoid was achieved, corresponding to 12.5 microtesla of field. Further details about this current sensor can be found in [7].

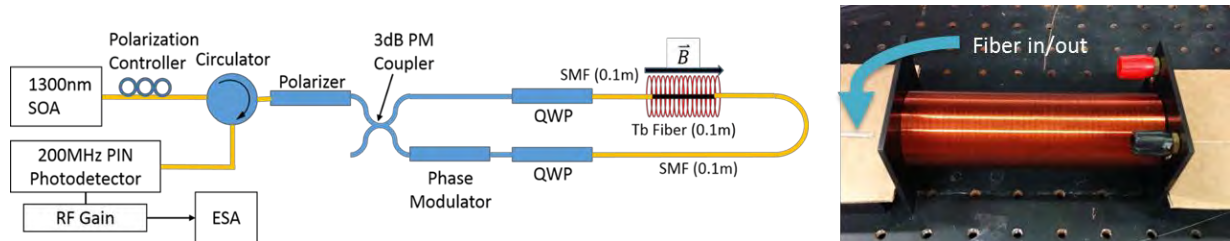


Figure 7.2: Schematic of the Tb-fiber based interferometric current sensor.

For this demonstration, the fiber was kept straight, but it would be wound around a current carrying wire in a real application. Despite the improvements in Verdet constant, the sensitivity could be improved by orders of magnitude if a material such as Ce:YIG could be used instead. Furthermore, integration of Ce:YIG clad waveguides with the heterogeneous silicon/III-V laser means that the entire magnetic/current sensor could be integrated together on a single chip, which dramatically reduces the SWaP + C. This is envisioned in [8], in which the sensitivity of the fully integrated magnetometer is predicted reach 20 femtotesla. The other advantage of integration is that the “front-end” of the sensor, comprising of all the lasers, modulators, and detectors, could be integrated on the same chip as well, as was demonstrated for an optical gyroscope [9].

However, once the MO sensing component is integrated, it can no longer be wound around a current carrying wire. Thus, it loses all the benefits of being resistant to stray

magnetic fields, such as the Earth's magnetic field. One way to address this is to use the sensors in sets of three, corresponding to the x, y, and z axis. This is similar to the deployment of optical gyroscopes, which can only sense rotation in one axis at a time. Alternatively, if a chip consisted of MO waveguides showing NRPS for TE mode as well as TM modes, it could provide magnetic field sensing in two axes at once, since the two polarizations are sensitive to magnetic fields in different directions.

In any case, it is apparent that the integrated MO sensor would be more like a magnetic field "point" sensor, rather than a current sensor. Nevertheless, this is a largely unexplored area, and could be of interest in the near future, as garnet materials such as Ce:YIG possess Verdet constants on the order of 10000 rad/Tm [10].

7.3 Magneto-optic switches

Another potential area in which magneto-optic devices may become useful is optical switching technologies. The rapid growth in data center networks has placed tremendous demand for technological improvements in all aspects, from the transceivers to the interfaces and switches. While optical switching is unlikely to completely replace electronic switching due to the difficulty in making reliable optical memory and buffers, they are very attractive in several switching architectures due to their immense bandwidth capacities. Bandwidth scaling for switch capacity is roughly a decade per five years based on historical data [11]. Switches are found in all layers of the datacenter networks with various functionalities such as broadcasting or routing. These switches have been demonstrated using various technologies, such as MEMs

based switches, SOA based switches, MZI networks, and MRR based switches. A comprehensive review of optical switching technologies in datacenters is found in [12].

While the underlying technology for optical switches is identical to that used for optical modulators, a switch is not just a slow modulator. Key differences between the two include the necessity of multiple ports for scalability a switch, as well as higher requirements for low insertion loss and low crosstalk in a switch [13]. Switching speed is important for some, but not all applications, since individual bits are rarely involved in the switching. Power consumption is also an important metric, as switching fabrics often involve hundreds, or even thousands of individual switch components. Currently, almost all optical switches have steady state power consumption. Power is dissipated to hold the switch in a state, regardless of the switching methodology (generally electro-optic or thermo-optic). MEMs and other voltage-controlled switches are better off in this sense, since they may only dissipate power in one switching state, and overall power consumption is low due to the capacitive nature of the switch. A downside to these is the large operating voltage, often in the tens or hundreds of volts [14]. Another voltage-controlled switch is using a MOS-capacitor, which has been demonstrated in lasers [15] and modulators [16]. Dark current is very low in these devices, but optical losses are considerable due to the high concentration of free carriers in the waveguide. Even so, none of these mechanisms are truly latching.

Using the magneto-optic effect for switching offers several attractive properties. First, ferromagnetism offers a latching, or self-holding behavior for switches that is uncommon for optical switches. Self-holding behavior has been observed using phase-change materials with incident laser pulses [17] or a floating gate transistor embedded

in the optics [18]. Recently, a magneto-optic switch with self-holding operation was demonstrated by utilizing a thin-film FeCoB stripes above a MZI structure [19]. The stripes are magnetized using a silver microstrip, much like the devices in this thesis. The FeCoB retains magnetization even after the current pulses through the electromagnet die away. A one microsecond current pulse was enough to magnetize the FeCoB.

While this is an interesting proof of concept, many improvements can be made. The device was fabricated by depositing amorphous silicon on a garnet substrate, so it is not compatible with other silicon photonic devices. This is especially important given the need for scaling arguments. Microrings may also be a better design, as they are significantly smaller in footprint. The devices presented in this work may be suitable for future switching applications. The microring optical circulator discussed in Chapter 3 was further investigated for its switching characteristics [20]. A switching time of 400ps was measured, as shown by the eye diagram in Figure 7.3. The figure also shows the combined switching of the magneto-optic and thermal effects. The thermal-optic shift is much slower (on the order of kHz) compared with the MO switching in the GHz. Thus, the thermo-optic shift is not visible in the eye diagram.

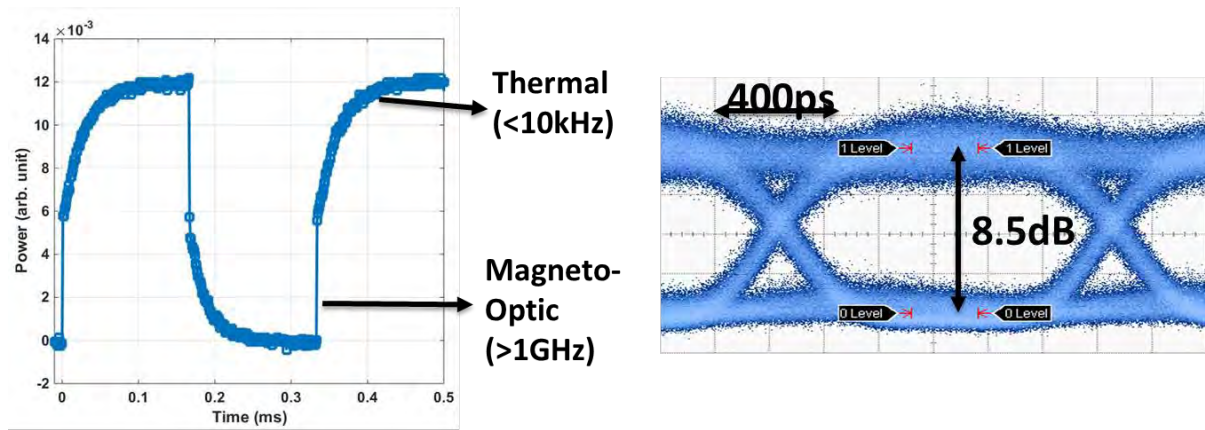


Figure 7.3: Experimental results of the switching time of the MO microring switch. The device used is identical to the microring isolator described in Chapter 3.

This is limited by the switching of the inductive electromagnet coil. Faster operation can be achieved by reducing skin depth effects and lowering the inductance of the microstrip, although additional limitations caused by magnetization reversal ($\sim 2\text{ps}$) [21] and photon lifetime ($\sim 12\text{ps}$) in the ring will eventually become relevant. No latching behavior was seen in this device, due to the weak remnant magnetization of Ce:YIG, so a thin-film magnet is needed in the future.

The magneto-optic devices are inherently nonreciprocal, so bidirectional transmission through the switch is possible. This could lead to a doubling of capacity in the switching network. Ultimately, the limiting factor is the optical loss. Losses through the MO devices should be reduced to an acceptable level ($<1\text{dB}$ per switching element) before practical switches can be constructed.

Summary

There are many practical uses of optical isolators and circulators in optical systems, some of which are presented in this chapter. As for their use in PIC, this is a largely

unexplored area given the lack of integrated isolators and circulators. In some cases, the only logical placement of the isolator is directly after the laser, which emphasizes laser and isolator co-integration, which was discussed in the previous chapter. There are also interesting magneto-optic devices outside of isolators. The magnetic sensor and magnetic switch are discussed, and the merits of using integrated magneto-optic waveguides for each are presented.

References

1. J. Hübner, D. Zauner, and M. Kristensen, "Strong sampled bragg gratings for WDM applications," *IEEE Photonics Technol. Lett.* **10**, 552–554 (1998).
2. J. M. P. Delavaux and J. A. Nagel, "Multi-Stage Erbium-Doped Fiber Amplifier Designs," *J. Light. Technol.* **13**, 703–720 (1995).
3. P. Pintus, N. Andriolli, F. Di Pasquale, and J. E. Bowers, "Bidirectional crosstalk and back-reflection free WDM active optical interconnects," *IEEE Photonics Technol. Lett.* **25**, 1973–1976 (2013).
4. J. L. Cruz, M. V. Andres, and M. A. Hernandez, "Faraday effect in standard optical fibers: dispersion of the effective Verdet constant," *Appl. Opt.* **35**, 922 (1996).
5. L. Sun, S. Jiang, and J. R. Marciante, "Compact all-fiber optical Faraday components using 65-wt%-terbium-doped fiber with a record Verdet constant of -32 rad/(Tm)," *Opt. Express* **18**, 12191 (2010).
6. L. Sun, S. Jiang, and J. R. Marciante, "All-fiber optical magnetic-field sensor based on Faraday rotation in highly terbium-doped fiber," *Opt. Express* **18**, 5407 (2010).
7. D. Huang, S. Srinivasan, and J. E. Bowers, "Compact Tb doped fiber optic current sensor with high sensitivity," *Opt. Express* **23**, 29993 (2015).
8. S. Srinivasan and J. E. Bowers, "Integrated high sensitivity hybrid silicon magnetometer," *IEEE Photonics Technol. Lett.* **26**, 1321–1324 (2014).
9. M. A. Tran, T. Komljenovic, J. C. Hulme, M. Kennedy, D. J. Blumenthal, and J. E. Bowers, "Integrated optical driver for interferometric optical gyroscopes," *Opt. Express* **4**, 3826–3840 (2017).
10. D. Huang, P. Pintus, S. Srinivasan, and J. E. Bowers, "Integrated compact optical

- current sensors with high sensitivity," 97440D (2016).
11. X. Zhou, H. Liu, and R. Urata, "Datacenter optics : requirements , technologies , and trends," *Chinese Opt. Lett.* **15**, 120008 (2017).
 12. Q. Cheng, S. Rumley, M. Bahadori, and K. Bergman, "Photonic switching in high performance datacenters [Invited]," *Opt. Express* **26**, 16022 (2018).
 13. R. Soref, "Tutorial: Integrated-photonic switching structures," *APL Photonics* **3**, (2018).
 14. T. J. Seok, N. Quack, S. Han, R. S. Muller, and M. C. Wu, "Large-scale broadband digital silicon photonic switches with vertical adiabatic couplers," *Optica* **3**, 64 (2016).
 15. D. Liang, X. Huang, G. Kurczveil, M. Fiorentino, and R. G. Beausoleil, "Integrated finely tunable microring laser on silicon," *Nat. Photonics* **10**, 719–722 (2016).
 16. J. H. Han, F. Boeuf, J. Fujikata, S. Takahashi, S. Takagi, and M. Takenaka, "Efficient low-loss InGaAsP/Si hybrid MOS optical modulator," *Nat. Photonics* **11**, 486–490 (2017).
 17. D. Tanaka, Y. Shoji, M. Kuwahara, X. Wang, K. Kintaka, H. Kawashima, T. Toyosaki, Y. Ikuma, and H. Tsuda, "Ultra-small, self-holding, optical gate switch using Ge₂Sb₂Te₅ with a multi-mode Si waveguide," *Opt. Express* **20**, 442–445 (2012).
 18. J.-F. Song, A. E.-J. Lim, X.-S. Luo, Q. Fang, C. Li, L. X. Jia, X.-G. Tu, Y. Huang, H.-F. Zhou, T.-Y. Liow, and G.-Q. Lo, "Silicon photonic integrated circuits with electrically programmable non-volatile memory functions," *Opt. Express* **24**, 21744 (2016).
 19. K. Okazeri, K. Muraoka, Y. Shoji, S. Nakagawa, N. Nishiyama, S. Arai, and T. Mizumoto, "Self-Holding Magneto-Optical Switch Integrated with Thin-Film Magnet," *IEEE Photonics Technol. Lett.* **30**, 371–374 (2018).
 20. D. Huang, P. Pintus, C. Zhang, P. Morton, Y. Shoji, T. Mizumoto, and J. E. Bowers, "Dynamically reconfigurable integrated optical circulators," *Optica* **4**, 23 (2017).
 21. I. Tudosa, C. Stamm, A. B. Kashuba, F. King, H. C. Siegmann, G. Ju, B. Lu, D. Weller, and J. Sto, "The ultimate speed of magnetic switching in granular recording media," *Nature* **124**, 831–833 (2003).

Chapter 8

Conclusions and Future Outlook

8.1 Conclusions

The search for a viable optical isolator and circulator for integrated optics has been a topic of interest for researchers for decades. The design for an integrated magneto-optic waveguide based isolator was proposed decades ago, and all the underlying physics and principles of the device are well studied. However, these devices never became mainstream due to their fabrication complexity and use of magneto-optic materials, which are generally incompatible with the commonly used silicon and III-V photonic platforms. Therefore, the isolator problem was ignored and efforts were made to bypass the issue completely through careful engineering of the laser and other photonic elements to be reflection-free.

This becomes more and more challenging as the complexity of PICs scale and the level of integration grows. With the growth of silicon photonics came progress in heterogeneous integration, in order to introduce new materials on silicon. Wafer bonding techniques and heterogeneous integration in general provided a new twist to the isolator problem, as it allowed for significantly more flexibility when it came to device design and the materials available to the researcher. The first wafer-bonded

isolator on silicon was demonstrated in 2008 [1], and the first microring based isolator was shown in 2011 [2], two years before this work started. The performance of the first devices were fairly poor, as expected. The microring isolator only showed 9dB of isolation, as it was severely undercoupled. The magnetic field was produced by a small neodymium cylinder magnet placed on top of the chip. Due to the size of the magnet, the ring radius was 900 microns, which led to the undercoupling of the device.

Chapter 3 described the improvements made to this pre-existing concept, starting from waveguide optimization to the inclusion of an electromagnet. The fabrication development leading to the on-chip electromagnet was crucial, as the ring could be shrunk down to as low as 20 microns in radius, and critical coupling was achieved. This led to a greatly improved isolation ratio of 32dB [3]. Further improvements such as increasing the efficiency of the electromagnet, cascading multiple rings [4], and demonstrating the first microring circulator [5] were also covered in Chapter 3. A need for greater isolation bandwidth led to the results discussed in Chapter 4, where the integrated electromagnet was carried over to the more common MZI isolator with great success. The electromagnet solution elegantly enables push-pull operation of the device, and the ability to tune the strength of the magnetic field enabled flexibility in operating the device. The operating wavelength can be freely tuned, and the optimal phase conditions can always be achieved with proper tuning [6].

Despite these improvements and record results, the isolators and circulators were still incompatible with typical semiconductor lasers due to their requirement that the light be TM polarized. Chapter 5 covered the successful efforts to integrate a polarization rotator with the isolator that would allow the devices to be integrated with a TE-

polarization emitting laser. Both a microring isolator for TE polarization and a MZI circulator for TE polarization were demonstrated, both of which were the first of their kind [7]. Chapter 6 covers the ongoing efforts to bring everything together, and integrated isolators with lasers. A number of challenges such as matching waveguide geometries and where to insert the isolator processing into the laser fabrication flow were discussed [8]. The full path towards heterogeneous integration of lasers with isolators on silicon was established, and a preliminary fabrication run was undertaken. While this run did not yield working devices, the problems were identified, and the researcher is hopeful that currently ongoing runs will see more success.

8.2 Future Outlook

A personal opinion of the researcher is that many of the efforts of the scientific community to invent a CMOS-compatible optical isolator are misguided. The real focus should be to develop a laser-compatible optical isolator. The reason is quite simple. The isolator needs to be placed immediately after the laser to be effective. Since silicon lacks a native laser, many solutions currently use an off-chip laser to provide light for the silicon PIC, through fiber coupling or direct coupling between the chips. In such a scenario, an on-chip isolator on the silicon PIC does not provide much value. Facets and grating couplers are a major source of reflection, which cannot be avoided unless the isolator immediately follows the laser. If the laser and silicon PIC are on different chips, an alternative solution to the on-chip isolator is to AR-coat the laser chip and place a

free-space or in-line isolator in between the two. Thus, in order for on-chip isolators to have real impact, one of two things should happen.

One way would be to increase the performance of the integrated isolator to the point where it rivals the performance of current devices. This is fairly challenging given that state of the art dual-stage TGG isolators have >60 dB of isolation with <1 dB of insertion loss. One could make the argument that an integrated isolator would offer significant cost savings, but such arguments are hard to make without data, and will not be discussed here. Alternatively, the motivation is integrating the isolator with the laser on the same chip, which can never be achieved otherwise. While the title of this dissertation is “Heterogeneously integrated optical isolators and circulators for silicon photonics”, the true value of it is the pathway outlined towards how to integrate the isolators with lasers. While significant progress has been made throughout this work, there remains many points to address.

1. One of the main issues is the large insertion loss of the devices in this work. Further investigation into where this loss originates is needed. Various papers quote the loss of Ce:YIG anywhere from 10 to 60dB/cm, depending on the growth conditions and subsequent anneal conditions. From our measurements, we estimate the loss in the silicon/Ce:YIG waveguide to be in the 20-25dB/cm range. Of course, this is a combination of scattering losses in silicon, scattering losses at the bond interface, as well as Ce:YIG loss. Our conservative estimates then place the loss in Ce:YIG to be on the order of 30-40dB/cm. If this can be reduced down to the lower 10dB/cm value, the device performance could improve significantly.
2. Significant improvements can be made in the fabrication of these devices. Mechanical polishing of the SGGG substrate was reliable at the chip level, but could be much more difficult at the wafer level. Ideally, an alternate technique would be developed. If an etch

stop layer could be implemented in the garnet stack, as is the case for III-V laser epi, then the substrate removal process could be extended to a wafer scale. Alternately, the smart-cut technology mentioned in Chapter 3 should be investigated, as it is also a method to transfer the thin garnet film. Other methods such as transfer printing could also be applicable.

3. A significant portion of the researcher's time was spent investigating the deposition of Ce:YIG and other garnets. Some of these efforts were outlined in Chapter 5, but ultimately success was very limited. However, reliable deposition of garnet would open up many opportunities. The garnet should only be deposited where needed, which can be achieved using liftoff techniques, or etching. Experiments were taken to verify the liftoff of epitaxially deposited garnet, and they were successful, although the films showed little Faraday rotation. If a monolithic approach could be adopted, this would also decrease the insertion loss, especially in the case of the microring isolator, since the Ce:YIG does not need to interact with the bus waveguide at all. Bandwidth concerns of the microring isolator can be partially alleviated by inclusion of another ring filter as a part of the design, which would filter out reflections outside the isolation bandwidth.
4. Few studies have been done regarding the power handling of integrated isolators. This is important, as the isolation ratio should stay constant regardless of the input laser power.
5. The successful integration of isolators with lasers opens up a plethora of opportunities. This starts with the simple laser and isolator PIC discussed in Chapter 6 and extends to designs such as a unidirectional laser. If the isolator is placed in the cavity of a ring laser, it would suppress lasing in one direction. Other applications involving the circulator include Bragg grating add-drop filters, which are commonplace in fiber-optics, but have never made an appearance in integrated optics. Finally, placing a wideband isolator in between a laser and SOA would lead to higher stability of the laser.

Thus, the work here should serve as a starting point towards realistic laser and isolator integration. Products today are packaged with bulk isolators, significantly increasing price and size. Therefore, the focus should be on achieving a laser-compatible optical isolator, as it doesn't make much sense to sell an integrated isolator as a discrete

component. A laser plus isolator combination is the end goal. Further improvements are needed in both device performance as well as process development. This continues to be an exciting, active field of research, and should see significant progress in the near future.

References

1. Y. Shoji, T. Mizumoto, H. Yokoi, I. W. Hsieh, and R. M. Osgood, "Magneto-optical isolator with silicon waveguides fabricated by direct bonding," *Appl. Phys. Lett.* **92**, (2008).
2. M.-C. Tien, T. Mizumoto, P. Pintus, H. Kromer, and J. E. Bowers, "Silicon ring isolators with bonded nonreciprocal magneto-optic garnets," *Opt. Express* **19**, 11740 (2011).
3. D. Huang, P. Pintus, C. Zhang, Y. Shoji, T. Mizumoto, and J. E. Bowers, "Electrically driven and thermally tunable integrated optical isolators for silicon photonics," *IEEE J. Sel. Top. Quantum Electron.* **22**, (2016).
4. P. Pintus, D. Huang, C. Zhang, Y. Shoji, T. Mizumoto, and J. E. Bowers, "Microring-Based Optical Isolator and Circulator with Integrated Electromagnet for Silicon Photonics," *J. Light. Technol.* **35**, 1429–1437 (2017).
5. D. Huang, P. Pintus, C. Zhang, P. Morton, Y. Shoji, T. Mizumoto, and J. E. Bowers, "Dynamically reconfigurable integrated optical circulators," *Optica* **4**, 23 (2017).
6. D. Huang, P. Pintus, Y. Shoji, P. Morton, T. Mizumoto, and J. E. Bowers, "Integrated broadband optical isolators for silicon photonics with over 100nm tuning range," *Opt. Lett.* **42**, 4901–4904 (2017).
7. P. Pintus, D. Huang, P. A. Morton, Y. Shoji, T. Mizumoto, and J. E. Bowers, "Broadband TE Optical Isolators and Circulators in Silicon Photonics through Ce:YIG Bonding," *J. Light. Technol.* **8724**, 1–1 (2019).
8. D. Huang, P. Pintus, and J. E. Bowers, "Towards heterogeneous integration of optical isolators and circulators with lasers on silicon [Invited]," *Opt. Mater. Express* **8**, 2471–2483 (2018).